

Measurement of the CKM angle γ using $B_s^0 \rightarrow D_s K \pi\pi$ decays

P. d'Argent¹, E. Gersabeck², M. Kecke¹, M. Schiller³

¹*Physikalisches Institut, Ruprecht-Karls-Universität Heidelberg, Heidelberg, Germany*

²*School of Physics and Astronomy, University of Manchester, Manchester, United Kingdom*

³*School of Physics and Astronomy, University of Glasgow, Glasgow, United Kingdom*

Abstract

We present the first measurement of the weak phase $\gamma - 2\beta_s$ obtained from a time-dependent (amplitude) analysis of $B_s^0 \rightarrow D_s K \pi\pi$ decays using proton-proton collision data corresponding to an integrated luminosity of 7 fb^{-1} recorded by the LHCb detector.

Change-log

- Version 1.0: First note draft circulated to the WG
- Version 2.0: Implemented first round of comments from Mark, Alessandro, Agnieszka
 - Changed D^0 bkg vetoes (Sec. 4.2.2)
 - Revisited some systematics
 - * Use uncertainty from fake rate instead of fixing misID yield to 0 or twice the value (Sec. 12.2)
 - * Use GLASS model instead of RBW as alternative to LASS model for $K\pi$ S-wave (Sec. 12.9)
 - * Instead of assuming pure phase space, recalculate running width of three-body resonances taking only the dominant $K\pi\pi$ decay mode into account (Sec. 12.9)
 - * Calculate RMS of lineshape variations instead of summing them up in quadrature (Sec. 12.9)
 - * Bug fix in evaluation of fixed lineshape parameters (mass, width, form-factor) systematic (Sec. 12.9)
 - Added tables with alternative amplitude models (Sec. 12.10)
 - Added comparison plots of 16 vs 17 data (Sec. M)
- Version 3.0:
 - Changed D^0 bkg vetoes back to the ones from v1.0 to account for additional Kaon misID (Fig. 4.3)
 - Updated analysis with new MC samples (Sec. 4.3)
 - Studied time resolution separately for 16 and 17 data (Sec. 6.2)
 - Changed phasespace acceptance method from BDT to MC integration (Sec. 7.3)
 - Updated analysis with latest OS Tagger tuning (Sec. 8.1)
- Version 3.1: Minor changes, approved by Mark and Alessandro
- Version 3.2: Updated fit validation of phasespace-integrated and full fit using the same data set (Sec. 2.4)
- Version 4.0: Implemented first round of comments from Marta and Rafael
 - Added a small section summarizing the main analysis steps (Sec. 3)
 - Small improvements to the formalism (Sec. 2) and additional information on used lineshapes (Sec. A)
 - Additional information on fit stability and interference fractions (Sec. K)
 - Added additional systematic studies for the phase-space acceptance (Sec. 12.8)
 - Added rough estimate of sensitivity to physical observables from phase-space integrated fit (Sec. 10.2)

- Added comparison of phase-space integrated and full time-dependent amplitude fit (Sec. 13)
- Version 4.1: Implemented second round of comments from Marta and Rafael
 - Added systematics for fit fractions (Table 11.3)
 - Added additional information to tagging calibration (Sec. 8.1) and detection asymmetry sections (Sec. 9.2)
- Version 5.0: Unblinded results
- Version 5.1: Updated systematics

Contents

1	Introduction	1
2	Formalism	2
2.1	Decay rates and CP -observables	2
2.2	Amplitude model	4
2.2.1	Form Factors and Resonance Lineshapes	4
2.2.2	Spin Densities	5
2.3	Fit implementation	7
2.4	Validation	8
3	Analysis strategy	11
4	Data samples and event selection	11
4.1	Stripping and Trigger selection	11
4.2	Offline selection	11
4.2.1	Phase space region	12
4.2.2	Physics background vetoes	13
4.2.3	Training of multivariate classifier	16
4.2.4	Final selection	17
4.3	Simulation	22
5	Yields determination	23
5.1	Signal model	23
5.2	Background models	24
5.3	Results	26
6	Decay-time Resolution	27
6.1	Calibration for Run-I data	28
6.2	Calibration for Run-II data	29
7	Acceptance	32
7.1	MC corrections	32
7.1.1	Truth matching of simulated candidates	32
7.1.2	Correction of data-simulation differences	32
7.2	Decay-time acceptance	33
7.3	Phase space acceptance	37
8	Flavour Tagging	39
8.1	OS tagger combination	40
8.2	Tagging performance	42
9	Production and Detection Asymmetries	43
9.1	B_s Production Asymmetry	43
9.2	$K^-\pi^+$ Detection Asymmetry	44

10 Decay-time fit	47
10.1 Fit to $B_s^0 \rightarrow D_s\pi\pi\pi$ data	47
10.2 Fit to $B_s^0 \rightarrow D_sK\pi\pi$ data	47
11 Time-dependent amplitude fit	51
11.1 Signal Model Construction	51
11.2 Results	55
12 Systematic uncertainties	58
12.1 Fit bias	58
12.2 Background subtraction	58
12.3 Decay-time acceptance	59
12.4 Decay-time resolution and tagging	59
12.5 Production, detection asymmetries and mixing frequency	60
12.6 Multiple candidates	60
12.7 Length and momentum scales	60
12.8 Phase space acceptance	61
12.9 Resonance description	61
12.10 Alternative amplitude models	62
13 Summary	68
A Parametrization of Amplitude Lineshapes	69
B Stripping and Trigger cuts	72
C Details of multivariate classifier	74
D Detailed mass fits	79
E Decay-time Resolution fits	84
F Comparison of time-acceptance in subsamples	88
G Comparison of phase-space acceptance in subsamples	88
H OS tagger calibration parameters	91
I Spin Amplitudes	92
J Considered Decay Chains	93
K Additional information for the time-dependent amplitude fit	94
L Data-simulation comparisson	97
M Data distributions	98
References	104

1 Introduction

This note presents the first measurement of the CKM angle $\gamma \equiv \arg[-(V_{ud}V_{ub}^*)/(V_{cd}V_{cb}^*)]$ using $B_s^0 \rightarrow D_s K\pi\pi$ decays, where the $K\pi\pi$ subsystem is dominated by excited kaon states such as the $K_1(1270)$ and $K_1(1400)$ resonances [1–3]. In these decays, sensitivity to the weak phase results from the interference between $b \rightarrow c$ and $b \rightarrow u$ transitions achieved through $B_s^0 - \bar{B}_s^0$ mixing [4,5]. The amplitudes for both processes are of the same order in the Wolfenstein parameters λ , $\mathcal{O}(\lambda^3)$, so that interference effects are expected to be large. The corresponding Feynman diagrams are shown in Fig. 1.1. Due to the interference between mixing and decay amplitudes, the physical CP violating observables in these decays are functions of a combination of γ and the mixing phase β_s , namely $\gamma - 2\beta_s$. To account for the non-constant strong phase across the phase space, one can either perform a time-dependent amplitude fit or select a suitable phase-space region and introduce a coherence factor as additional hadronic parameter to the decay-time fit, in which case the procedure is very similar to the analysis of $B_s^0 \rightarrow D_s K$ decays [6,7]. Both approaches are explored in this note. The topologically very similar yet flavour specific decay $B_s \rightarrow D_s \pi\pi\pi$ is used as calibration channel, not only to calibrate the tagging algorithms and determine the decay-time acceptance but also to constrain the $B_s^0 - \bar{B}_s^0$ mixing frequency. The branching ration of these decay modes was measured by LHCb to be $\frac{\mathcal{B}(B_s^0 \rightarrow D_s K\pi\pi)}{\mathcal{B}(B_s^0 \rightarrow D_s \pi\pi\pi)} = 0.052 \pm 0.005(\text{stat}) \pm 0.003(\text{syst})$ [1,2].

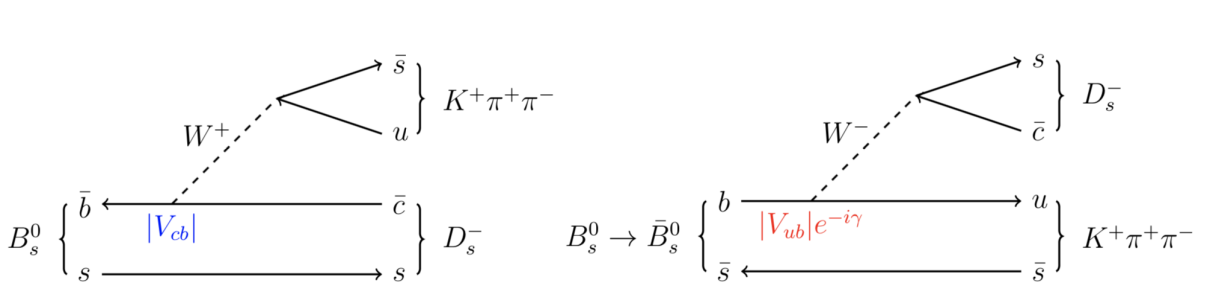


Figure 1.1: Feynman diagram for $B_s^0/\bar{B}_s^0 \rightarrow D_s^- K^+ \pi^+ \pi^-$ decays.

2 Formalism

2.1 Decay rates and CP -observables

The differential decay rate of B_s^0 or \bar{B}_s^0 decays to the final state $D_s^- K^+ \pi\pi$ or $D_s^+ K^- \pi\pi$ is given by:

$$\begin{aligned} \frac{d\Gamma(\mathbf{x}, t, q_t, q_f)}{e^{-\Gamma_s t} dt d\Phi_4} &\propto (|\mathcal{A}_f^c(\mathbf{x})|^2 + |\mathcal{A}_f^u(\mathbf{x})|^2) \cosh\left(\frac{\Delta\Gamma_s t}{2}\right) \\ &\quad + q_t q_f (|\mathcal{A}_f^c(\mathbf{x})|^2 - |\mathcal{A}_f^u(\mathbf{x})|^2) \cos(\Delta m_s t) \\ &\quad - 2\text{Re}(\mathcal{A}_f^c(\mathbf{x})^* \mathcal{A}_f^u(\mathbf{x}) e^{-iq_f(\gamma-2\beta_s)}) \sinh\left(\frac{\Delta\Gamma_s t}{2}\right) \\ &\quad - 2q_t q_f \text{Im}(\mathcal{A}_f^c(\mathbf{x})^* \mathcal{A}_f^u(\mathbf{x}) e^{-iq_f(\gamma-2\beta_s)}) \sin(\Delta m_s t) \end{aligned} \quad (2.1)$$

where $q_t = +1$ (-1) refers to an initially produced B_s^0 (\bar{B}_s^0) flavour eigenstate, $q_t = 0$ to an undetermined initial flavour, $q_f = +1$ or -1 denotes $f = D_s^- K^+ \pi\pi$ or $\bar{f} = D_s^+ K^- \pi\pi$ final states and Γ_s , $\Delta\Gamma_s$ and Δm_s are the width average, the width difference and the mass difference of the two B_s mass eigenstates. We choose a convention in which $\Delta\Gamma_s < 0$ and $\Delta m_s > 0$. We further assume $|q/p| = 1$ for the complex coefficients p and q which relate the B_s meson mass eigenstates to the flavour eigenstates (no CP violation in the mixing). The CKM angle γ can be extracted from the CP violating phase associated to the interference between mixing and decay, $\gamma - 2\beta_s$, since the $B_s^0 - \bar{B}_s^0$ mixing phase, β_s , is well constrained from $B_s \rightarrow J/\psi \phi$ and related modes.

The static total decay amplitudes $\mathcal{A}_f^c(\mathbf{x})$ and $\mathcal{A}_f^u(\mathbf{x})$ are given by the coherent sum over all intermediate state amplitudes $A_i(\mathbf{x})$, each weighted by a complex coefficient describing the relative magnitude and phase which is to be determined from data,

$$\mathcal{A}(B_s^0 \rightarrow D_s^- K^+ \pi\pi) \equiv \mathcal{A}_f^c(\mathbf{x}) = \sum_i a_i^c A_i(\mathbf{x}) \quad (2.2)$$

$$\mathcal{A}(\bar{B}_s^0 \rightarrow D_s^- K^+ \pi\pi) \equiv \mathcal{A}_f^u(\mathbf{x}) = \sum_i a_i^u A_i(\mathbf{x}) \quad (2.3)$$

where the superscript c (u) indicates a $b \rightarrow c$ ($b \rightarrow u$) quark-level transition and \mathbf{x} represents a unique set of kinematic conditions within the five-dimensional phase space of the decay. Convenient choices for the kinematic observables include the invariant mass combinations of the final state particles or acoplanarity and helicity angles. In practice, we do not need to choose a particular five-dimensional basis, but use the full four-vectors of the decay in our analysis. The dimensionality is handled by the phase space element which can be written in terms of any set of five independent kinematic observables, $\mathbf{x} = (x_1, \dots, x_5)$, as

$$d\Phi_4 = \phi_4(\mathbf{x}) d^5x, \quad (2.4)$$

where $\phi_4(\mathbf{x}) = \left| \frac{\partial\Phi_4}{\partial(x_1, \dots, x_5)} \right|$ is the phase space density. In contrast to three-body decays, the four-body phase space density function is not flat in the usual kinematic variables. An analytic expression for ϕ_4 can be found in Ref. [8], but is not needed in practice, see Sec. 7.3.

49 Assuming there is no direct CP violation in the B_s decay implies for the CP conjugate
50 transition amplitudes:

$$\mathcal{A}(\bar{B}_s^0 \rightarrow \bar{f}) = \mathcal{A}_f^c(\mathbf{x}) = \mathcal{A}_f^c(\bar{\mathbf{x}}) \quad (2.5)$$

$$\mathcal{A}(B_s^0 \rightarrow \bar{f}) = \mathcal{A}_{\bar{f}}^u(\mathbf{x}) = \mathcal{A}_{\bar{f}}^u(\bar{\mathbf{x}}) \quad (2.6)$$

51 where the CP -conjugate phase space point $\bar{\mathbf{x}}$ is defined such that it is mapped onto
52 \mathbf{x} by the interchange of final state charges, and the reversal of three-momenta. The
53 phenomenological description of the intermediate state amplitudes is discussed in Sec. 2.2.

54

55 Rather than developing an amplitude model describing the whole phase space, it is also
56 possible to determine the CKM angle γ , in a model-independent way, from the decay-time
57 distribution only. The differential decay rate integrated over the phase space yields:

$$\int \frac{d\Gamma(x, t, q_t, q_f)}{e^{-\Gamma_s t} dt d\Phi_4} \propto \cosh\left(\frac{\Delta\Gamma_s t}{2}\right) + q_t q_f C \cos(\Delta m_s t) \\ + D_f \sinh\left(\frac{\Delta\Gamma_s t}{2}\right) - q_t S_f \sin(\Delta m_s t) \quad (2.7)$$

58 where the same convention for the CP coefficients as for the $B_s \rightarrow D_s K$ analysis is used:

$$C = \frac{1 - r^2}{1 + r^2} \quad (2.8)$$

$$D_f = -\frac{2r\kappa \cos(\delta - q_f(\gamma - 2\beta_s))}{1 + r^2} \quad (2.9)$$

$$S_f = q_f \frac{2r\kappa \sin(\delta - q_f(\gamma - 2\beta_s))}{1 + r^2} \quad (2.10)$$

59 The coherence factor κ , the strong phase difference δ and the ratio of the suppressed
60 ($b \rightarrow u$) over favored ($b \rightarrow c$) decay mode, averaged over the phase space, are defined as:

$$\kappa e^{i\delta} \equiv \frac{\int \mathcal{A}_f^c(x)^* \mathcal{A}_f^u(x) d\Phi_4}{\sqrt{\int |\mathcal{A}_f^c(x)|^2 d\Phi_4} \sqrt{\int |\mathcal{A}_f^u(x)|^2 d\Phi_4}} \quad (2.11)$$

$$r \equiv \frac{\sqrt{\int |\mathcal{A}_f^u(x)|^2 d\Phi_4}}{\sqrt{\int |\mathcal{A}_f^c(x)|^2 d\Phi_4}}. \quad (2.12)$$

61 The five CP coefficients $C, D \equiv D_f, \bar{D} \equiv D_{\bar{f}}, S \equiv S_f, \bar{S} \equiv S_{\bar{f}}$ can be extracted from
62 a fit to the decay-time distribution which allows to infer the four physical observables
63 $r, \delta, \gamma, \kappa$ as discussed in more detail in Sect. 2.4. This approach will be called phase-space
64 integrated fit in the following. In contrast, the approach using Eq. 2.1 will be referred
65 to as full time-dependent amplitude fit. In case of the phase-space integrated fit, the
66 coherence factor dilutes the sensitivity to the weak phase γ due to the integration over
67 the interfering amplitudes across the phase space. The value of κ is bounded between
68 zero and unity. The latter corresponds to the limit of only one contributing intermediate
69 state in which case the same sensitivity as in $B_s \rightarrow D_s K$ decays is reached, while $\kappa = 0$
70 would result in no sensitivity to γ at all.

71 **2.2 Amplitude model**

72 To construct the intermediate state amplitudes $A_i(\mathbf{x})$, the isobar approach is used, which
 73 assumes that the decay process can be factorized into subsequent two-body decay am-
 74 plitudes [9–11]. This gives rise to two different decay topologies; quasi two-body decays
 75 $B_s \rightarrow (R_1 \rightarrow h_1 h_2) (R_2 \rightarrow h_3 h_4)$ or cascade decays $B_s \rightarrow h_1 [R_1 \rightarrow h_2 (R_2 \rightarrow h_3 h_4)]$. In
 76 either case, the intermediate state amplitude is parameterized as a product of orbital
 77 angular momentum, L , dependent form factors B_L , included for each vertex of the decay
 78 tree, Breit-Wigner propagators T_R , included for each resonance R , and an overall angular
 79 distribution represented by a spin factor S ,

$$A_i(\mathbf{x}) = B_{L_{B_s}}(\mathbf{x}) [B_{L_{R_1}}(\mathbf{x}) T_{R_1}(\mathbf{x})] [B_{L_{R_2}}(\mathbf{x}) T_{R_2}(\mathbf{x})] S_i(\mathbf{x}). \quad (2.13)$$

80 The following description of the individual components is adapted from Ref. [12] and
 81 only included for completeness.

82 **2.2.1 Form Factors and Resonance Lineshapes**

83 To account for the finite size of the decaying resonances, the Blatt-Weisskopf penetration
 84 factors, derived in Ref. [13] by assuming a square well interaction potential with radius
 85 r_{BW} , are used as form factors, B_L . They depend on the breakup momentum q , which is
 86 defined as the magnitude of the three-momentum of one of the daughters in the rest frame
 87 of the decaying resonance and the orbital angular momentum L , between the resonance
 88 daughters. Their explicit expressions are

$$\begin{aligned} B_0(q) &= 1, \\ B_1(q) &= 1/\sqrt{1 + (q r_{\text{BW}})^2}, \\ B_2(q) &= 1/\sqrt{9 + 3 (q r_{\text{BW}})^2 + (q r_{\text{BW}})^4}. \end{aligned} \quad (2.14)$$

89 Resonance lineshapes are described as function of the energy-squared, s , by Breit-Wigner
 90 propagators

$$T(s) = \frac{1}{m_0^2 - s - i m_0 \Gamma(s)}, \quad (2.15)$$

91 where the total width, $\Gamma(s)$, is normalized to give the nominal width, Γ_0 , when evaluated
 92 at the nominal mass m_0 .

93 For a decay into two stable particles $R \rightarrow AB$, the energy dependence of the decay
 94 width can be described by

$$\Gamma_{R \rightarrow AB}^{(2)}(s) = \Gamma_0 \frac{m_0}{\sqrt{s}} \left(\frac{q}{q_0} \right)^{2L+1} \frac{B_L(q)^2}{B_L(q_0)^2}, \quad (2.16)$$

95 where q_0 is the value of the breakup momentum at the resonance pole [14].

96 The energy-dependent width for a three-body decay $R \rightarrow ABC$, on the other hand, is
 97 considerably more complicated and has no analytic expression in general. However, it can
 98 be obtained numerically by integrating the transition amplitude-squared over the phase
 99 space,

$$\Gamma_{R \rightarrow ABC}^{(3)}(s) = \frac{1}{2\sqrt{s}} \int |A_{R \rightarrow ABC}|^2 d\Phi_3, \quad (2.17)$$

and therefore requires knowledge of the resonant substructure. The three-body amplitude $A_{R \rightarrow ABC}$ can be parameterized similarly to the four-body amplitude in Eq. (2.13). In particular, it includes form factors and propagators of intermediate two-body resonances.

Both Eq. (2.16) and Eq. (2.17) give only the partial width for the decay into a specific channel. To obtain the total width, a sum over all possible decay channels has to be performed,

$$\Gamma(s) = \sum_i g_i \Gamma_i(s), \quad (2.18)$$

where the coupling strength to channel i , is given by g_i .

Equation (2.16) is used by default for resonances decaying into a two-body final state. For the $K\pi$ and $\pi\pi$ S-wave resonances as well as for the $\rho(770)$ meson more sophisticated parameterizations are employed. Their explicit expressions are given in Appendix A. The nominal masses and widths of the resonances are taken from the PDG [15] with the exceptions described in Appendix K. The running width distributions for various 3-body resonances, calculated from Eq. 2.17, are shown in Appendix A.

Some particles may not originate from a resonance but are in a state of relative orbital angular momentum. We denote such non-resonant states by surrounding the particle system with brackets and indicate the partial wave state with an subscript; for example $(\pi\pi)_S$ refers to a non-resonant di-pion S -wave. The lineshape for non-resonant states is set to unity.

2.2.2 Spin Densities

The spin amplitudes are phenomenological descriptions of decay processes that are required to be Lorentz invariant, compatible with angular momentum conservation and, where appropriate, parity conservation. They are constructed in the covariant Zemach (Rarita-Schwinger) tensor formalism [16–18]. At this point, we briefly introduce the fundamental objects of the covariant tensor formalism which connect the particle’s four-momenta to the spin dynamics of the reaction and give a general recipe to calculate the spin factors for arbitrary decay trees. Further details can be found in Refs. [19, 20].

A spin- S particle with four-momentum p , and spin projection λ , is represented by the polarization tensor $\epsilon_{(S)}(p, \lambda)$, which is symmetric, traceless and orthogonal to p . These so-called Rarita-Schwinger conditions reduce the a priori 4^S elements of the rank- S tensor to $2S + 1$ independent elements in accordance with the number of degrees of freedom of a spin- S state [17, 21].

The spin projection operator $P_{(S)}^{\mu_1 \dots \mu_S \nu_1 \dots \nu_S}(p_R)$, for a resonance R , with spin $S = \{0, 1, 2\}$, and four-momentum p_R , is given by [20]:

$$\begin{aligned} P_{(0)}^{\mu\nu}(p_R) &= 1 \\ P_{(1)}^{\mu\nu}(p_R) &= -g^{\mu\nu} + \frac{p_R^\mu p_R^\nu}{p_R^2} \\ P_{(2)}^{\mu\nu\alpha\beta}(p_R) &= \frac{1}{2} \left[P_{(1)}^{\mu\alpha}(p_R) P_{(1)}^{\nu\beta}(p_R) + P_{(1)}^{\mu\beta}(p_R) P_{(1)}^{\nu\alpha}(p_R) \right] - \frac{1}{3} P_{(1)}^{\mu\nu}(p_R) P_{(1)}^{\alpha\beta}(p_R), \end{aligned} \quad (2.19)$$

where $g^{\mu\nu}$ is the Minkowski metric. Contracted with an arbitrary tensor, the projection operator selects the part of the tensor which satisfies the Rarita-Schwinger conditions.

For a decay process $R \rightarrow AB$, with relative orbital angular momentum L , between particle A and B , the angular momentum tensor is obtained by projecting the rank- L tensor $q_R^{\nu_1} q_R^{\nu_2} \dots q_R^{\nu_L}$, constructed from the relative momenta $q_R = p_A - p_B$, onto the spin- L subspace,

$$L_{(L)\mu_1\dots\mu_L}(p_R, q_R) = (-1)^L P_{(L)\mu_1\dots\mu_L\nu_1\dots\nu_L}(p_R) q_R^{\nu_1} \dots q_R^{\nu_L}. \quad (2.20)$$

Their $|\vec{q}_R|^L$ dependence accounts for the influence of the centrifugal barrier on the transition amplitudes. For the sake of brevity, the following notation is introduced,

$$\begin{aligned} \varepsilon_{(S)}(R) &\equiv \varepsilon_{(S)}(p_R, \lambda_R), \\ P_{(S)}(R) &\equiv P_{(S)}(p_R), \\ L_{(L)}(R) &\equiv L_{(L)}(p_R, q_R). \end{aligned} \quad (2.21)$$

Following the isobar approach, a four-body decay amplitude is described as a product of two-body decay amplitudes. Each sequential two-body decay $R \rightarrow A B$, with relative orbital angular momentum L_{AB} , and total intrinsic spin S_{AB} , contributes a term to the overall spin factor given by

$$\begin{aligned} S_{R \rightarrow AB}(\mathbf{x}|L_{AB}, S_{AB}; \lambda_R, \lambda_A, \lambda_B) &= \varepsilon_{(S_R)}(R) X(S_R, L_{AB}, S_{AB}) L_{(L_{AB})}(R) \\ &\times \Phi(\mathbf{x}|S_{AB}; \lambda_A, \lambda_B), \end{aligned} \quad (2.22)$$

where

$$\Phi(\mathbf{x}|S_{AB}; \lambda_A, \lambda_B) = P_{(S_{AB})}(R) X(S_{AB}, S_A, S_B) \varepsilon_{(S_A)}^*(A) \varepsilon_{(S_B)}^*(B). \quad (2.23)$$

Here, a polarization vector is assigned to the decaying particle and the complex conjugate vectors for each decay product. The spin and orbital angular momentum couplings are described by the tensors $P_{(S_{AB})}(R)$ and $L_{(L_{AB})}(R)$, respectively. Firstly, the two spins S_A and S_B , are coupled to a total spin- S_{AB} state, $\Phi(\mathbf{x}|S_{AB})$, by projecting the corresponding polarization vectors onto the spin- S_{AB} subspace transverse to the momentum of the decaying particle. Afterwards, the spin and orbital angular momentum tensors are properly contracted with the polarization vector of the decaying particle to give a Lorentz scalar. This requires in some cases to include the tensor $\varepsilon_{\alpha\beta\gamma\delta} p_R^\delta$ via

$$X(j_a, j_b, j_c) = \begin{cases} 1 & \text{if } j_a + j_b + j_c \text{ even} \\ \varepsilon_{\alpha\beta\gamma\delta} p_R^\delta & \text{if } j_a + j_b + j_c \text{ odd} \end{cases}, \quad (2.24)$$

where $\varepsilon_{\alpha\beta\gamma\delta}$ is the Levi-Civita symbol and j refers to the arguments of X defined in Eqs. 2.22 and 2.23. Its antisymmetric nature ensures the correct parity transformation behavior of the amplitude. The spin factor for a whole decay chain, for example $R \rightarrow (R_1 \rightarrow AB)(R_2 \rightarrow CD)$, is obtained by combining the two-body terms and performing a sum over all unobservable, intermediary spin projections

$$\sum_{\lambda_{R_1}, \lambda_{R_2}} S_{R \rightarrow R_1 R_2}(\mathbf{x}|L_{R_1 R_2}; \lambda_{R_1}, \lambda_{R_2}) S_{R_1 \rightarrow AB}(\mathbf{x}|L_{AB}; \lambda_{R_1}) S_{R_2 \rightarrow CD}(\mathbf{x}|L_{CD}; \lambda_{R_2}), \quad (2.25)$$

where $\lambda_R = \lambda_A = \lambda_B = \lambda_C = \lambda_D = 0$, $S_{AB} = S_{CD} = 0$ and $S_{R_1 R_2} = L_{R_1 R_2}$, as only pseudoscalar initial/final states are involved.

The spin factors for all decay topologies considered in this analysis are explicitly given in Appendix I.

¹⁶⁴ 2.3 Fit implementation

¹⁶⁵ The hadronic amplitudes are renormalized prior to the amplitude fit such that

$$\int |A_i(\mathbf{x})|^2 d\Phi_4 = 1. \quad (2.26)$$

¹⁶⁶ This allows us to set more intuitive starting values as the amplitude coefficients are all on
¹⁶⁷ a comparable scale. Moreover, the total amplitudes $\mathcal{A}_f^{c(u)}(\mathbf{x})$ are renormalized on-the-fly
¹⁶⁸ (*i.e.* at each minimization step) such that

$$\begin{aligned} & \int |\mathcal{A}_f^{c(u)}(\mathbf{x})|^2 d\Phi_4 = 1 \\ & \arg \left(\int \mathcal{A}_f^c(\mathbf{x})^* \mathcal{A}_f^u(\mathbf{x}) d\Phi_4 \right) = 0. \end{aligned} \quad (2.27)$$

¹⁶⁹ As a result, the average amplitude ratio and strong phase difference between the $b \rightarrow u$ and
¹⁷⁰ $b \rightarrow c$ transitions can be introduced as direct fit parameters instead of derived quantities
¹⁷¹ that have to be calculated from Equation 2.11 after the fit. For the differential decay rate
¹⁷² follows:

$$\begin{aligned} \frac{d\Gamma(\mathbf{x}, t, q, f)}{e^{-\Gamma_s t} dt d\Phi_4} \propto & (|\mathcal{A}_f^c(\mathbf{x})|^2 + r^2 |\mathcal{A}_f^u(\mathbf{x})|^2) \cosh \left(\frac{\Delta\Gamma_s t}{2} \right) \\ & + q_t q_f (|\mathcal{A}_f^c(\mathbf{x})|^2 - r^2 |\mathcal{A}_f^u(\mathbf{x})|^2) \cos (\Delta m_s t) \\ & - 2 r \text{Re} (\mathcal{A}_f^c(\mathbf{x})^* \mathcal{A}_f^u(\mathbf{x}) e^{i\delta - iq_f(\gamma - 2\beta_s)}) \sinh \left(\frac{\Delta\Gamma_s t}{2} \right) \\ & - 2 q_t q_f r \text{Im} (\mathcal{A}_f^c(\mathbf{x})^* \mathcal{A}_f^u(\mathbf{x}) e^{i\delta - iq_f(\gamma - 2\beta_s)}) \sin (\Delta m_s t) \end{aligned} \quad (2.28)$$

¹⁷³ This renormalization procedure was found to be crucial for the fit stability since it reduces
¹⁷⁴ the correlation between the a_i^c and a_i^u amplitude coefficients significantly. Due to the
¹⁷⁵ overall normalization, one of the complex amplitude coefficients a_i^c can be fixed to unity
¹⁷⁶ and since r and δ are included as fit parameters one of the complex amplitude coefficient
¹⁷⁷ a_i^u can be additionally fixed to unity.

¹⁷⁸ We force strong decays in the cascade topology to have the same pattern in $b \rightarrow c$
¹⁷⁹ and $b \rightarrow u$ transitions by the sharing of couplings between related quasi-two-body final
¹⁸⁰ states. For example, given the two a_i^c parameters required for $B_s \rightarrow D_s^- K_1(1270)^+$
¹⁸¹ with $K_1(1270)^+ \rightarrow \rho(770)^0 \pi^+$ and $K_1(1270)^+ \rightarrow K^*(892) \pi^+$, the amplitude $\bar{B}_s \rightarrow$
¹⁸² $D_s^- K_1(1270)^+$ with $K_1(1270)^+ \rightarrow \rho(770)^0 \pi^+$ and $K_1(1270)^+ \rightarrow K^*(892) \pi^+$ only requires
¹⁸³ one additional global complex parameter to represent the different production processes
¹⁸⁴ of $B_s \rightarrow D_s^- K_1(1270)^+$ and $\bar{B}_s \rightarrow D_s^- K_1(1270)^+$, while the relative magnitude and phase
¹⁸⁵ of $K_1(1270)^+ \rightarrow \rho(770)^0 \pi^+$ and $K_1(1270)^+ \rightarrow K^*(892) \pi^+$ are the same regardless of
¹⁸⁶ the production mechanism. For this purpose, multiple decay amplitudes of a three-body
¹⁸⁷ resonance are defined relative to a given reference channel.

188 2.4 Validation

189 The amplitude fit is performed by using the amplitude analysis tool **MINT2**. It was
 190 previously applied to analyze $D^0 \rightarrow 4\pi$ and $D^0 \rightarrow KK\pi\pi$ decays [12] which have an
 191 identical general spin structure (*i.e.* scalar to four scalar decay) to $B_s \rightarrow D_s K\pi\pi$ decays.
 192 In the course of the $D^0 \rightarrow hhhh$ analysis, the implementation of the amplitudes were
 193 extensively cross-checked against other available tools such as **qft++** [22], **AmpGen** [23]
 194 and where possible **EVTGEN** [24]. Since no additional line shapes or spin factors are
 195 needed for this analysis, we consider the amplitude calculation as fully validated.

196 This does, however, not apply to the full time-dependent amplitude pdf which is
 197 newly implemented for this analysis. To cross-check it, we use **EVTGEN** to generate
 198 toy events with time-dependent CP violation according to the **SSD_Cp** event model [24].
 199 Since this event model does not allow for multiple interfering resonances, we generate
 200 only the decay chain $B_s \rightarrow D_s(K_1(1400) \rightarrow K^*(892)\pi)$. Table 2.1 lists the generated
 201 input parameters. The toy data set is fitted with our **MINT2** implementation of the full
 202 time-dependent amplitude pdf and the phasespace-integrated pdf. Flat decay-time and
 203 phase-space acceptances are used. The true ID of the B_s meson is used to tag the initial
 204 flavor (*i.e.* perfect tagging). For technical reasons (the extreme case of perfect resolution
 205 is currently not implemented in our fitter) we smeared the generated decay-times with a
 206 Gaussian of width 45 fs. We use a Gaussian of the same width to convolute the pdf for
 207 fitting. More details of the fit procedures are given in Secs. 10 and 11. The fit projections
 208 are shown in Figs. 2.1 and 2.2.

209 The CP coefficients $C, D, \bar{D}, S, \bar{S}$ are the fit parameters in case of the phasespace-
 210 integrated pdf, which are converted after to the fit to the physical observables r, κ, δ and γ
 211 using the **GammaCombo** package [25]. The obtained 1-CL contours are shown in Fig. 2.3.
 212 The full pdf determines r, δ and γ directly. As shown in Tab. 2.2 and 2.3, the fit results
 213 are in excellent agreement with the generated input values. The phasespace-integrated fit
 214 is, in addition, performed with the **B2DX** fitter used for the $B_s \rightarrow D_s K$ analysis yielding
 215 identical results. Note though that some parts of the **B2DX** fitter have been taken over to
 216 our **MINT2** fitter, such that the implementations are not fully independent.

Table 2.1: Input values used to generate **EVTGEN** toy events according to the **SSD_Cp** event model.

τ	1.5 ps
$\Delta\Gamma$	-0.1 ps^{-1}
Δm_s	17.757 ps^{-1}
r	0.37
κ	1
δ	10.0°
γ	71.1°
β_s	0.0°

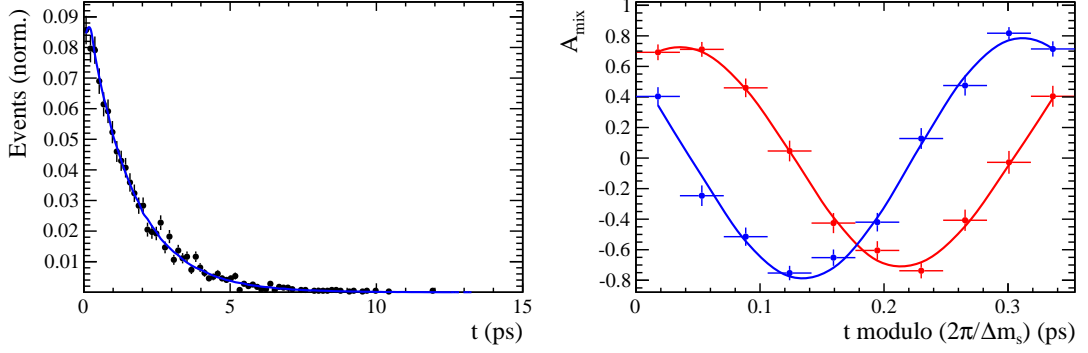


Figure 2.1: Left: Time distribution of $B_s \rightarrow D_s K \pi \pi$ events generated with EVTGEN (points with error bars) and MINT2 fit projections (solid line). Right: Time-dependent asymmetry between mixed and unmixed events folded into one oscillation period for $D_s^- K^+ \pi \pi$ (red) and $D_s^+ K^- \pi \pi$ (blue) final states. The data points show events generated with EVTGEN, while the solid lines show the MINT2 fit projections.

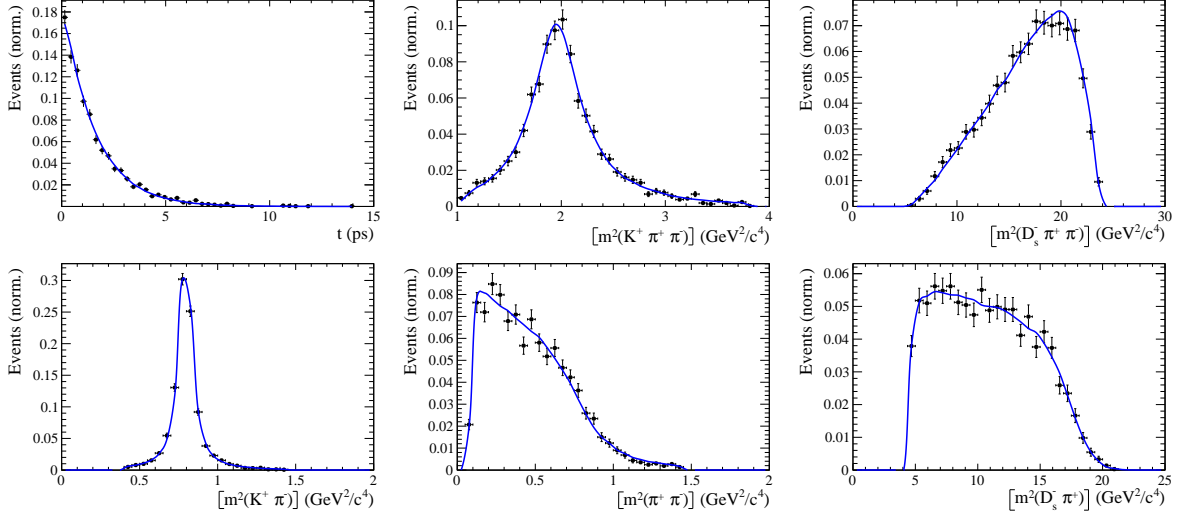


Figure 2.2: Time and invariant mass distributions of $B_s \rightarrow D_s K \pi \pi$ events generated with EVTGEN (points with error bars) and MINT2 fit projections (blue solid line).

Table 2.2: Result of the phasespace-integrated fit to EVTGEN toy events.

	Generated	Fit result	Pull(σ)
C	0.759	0.767 ± 0.023	0.3
D	-0.314	-0.194 ± 0.205	0.6
\bar{D}	-0.101	-0.189 ± 0.210	-0.4
S	-0.570	-0.556 ± 0.033	0.4
\bar{S}	-0.643	-0.683 ± 0.031	-1.3

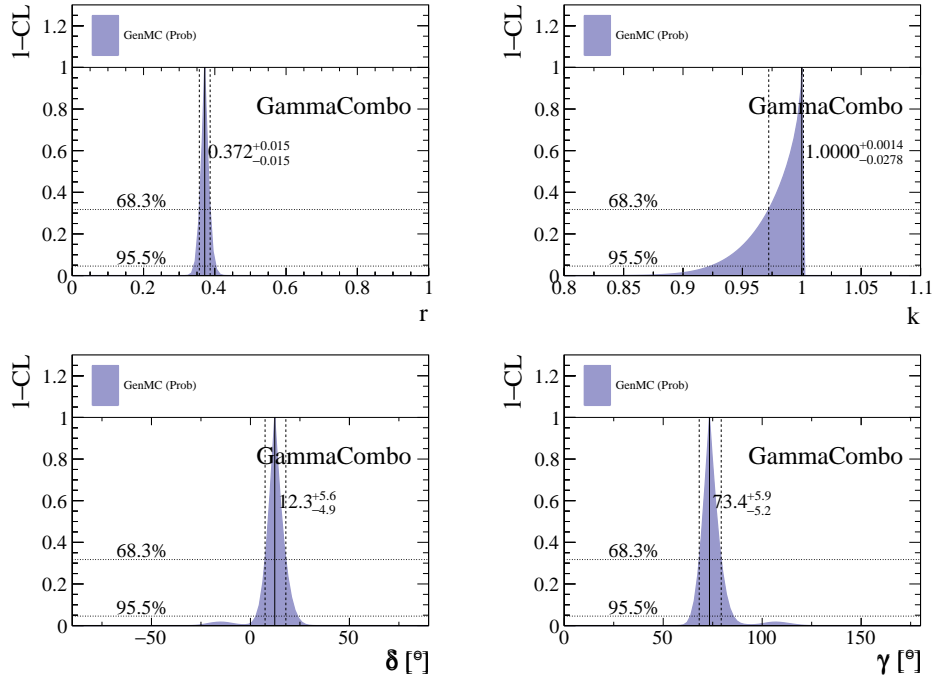


Figure 2.3: The 1-CL contours for the physical observable r, κ, δ and γ obtained with the phasespace-integrated fit to the EVTGEN toy sample.

Table 2.3: Results for the physical observables obtained from fits to EVTGEN toy events.

	Generated	Full PDF	Phasespace-integrated
r	0.370	0.372 ± 0.015	0.372 ± 0.015
κ	1.0	1.0	1.000 ± 0.035
δ	10.0°	12.2 ± 5.1	12.3 ± 5.1
γ	71.1°	73.2 ± 5.5	73.4 ± 5.5

217 3 Analysis strategy

218 The selection of the signal, $B_s \rightarrow D_s K\pi\pi$, and calibration channel, $B_s \rightarrow D_s \pi\pi\pi$, are
219 outlined in Sect. 4, followed by the determination of the signal and background yields. The
220 calibration channel is used to study the decay-time acceptance, see Sect. 7, and to calibrate
221 the flavor tagging algorithms in Sect. 8. Moreover, the B_s mixing frequency is measured
222 in Sect. 10.1. Afterwards, the CKM angle γ is extracted from $B_s \rightarrow D_s K\pi\pi$ data using
223 two different approaches: the results of the phase-space integrated fit are presented in
224 Sect. 10.2, while Sect. 11 discusses the significantly more complicated full time-dependent
225 amplitude fit. The systematic uncertainties of both methods are determined in Sect. 12,
226 before we compare the results and conclude in Sect. 13.

227 4 Data samples and event selection

228 4.1 Stripping and Trigger selection

229 The dataset used for this analysis corresponds to 1 fb^{-1} of proton-proton collision data col-
230 lected in 2011 with a centre of mass energy $\sqrt{s} = 7 \text{ TeV}$, 2 fb^{-1} collected in 2012 with $\sqrt{s} =$
231 7 TeV and 4 fb^{-1} collected in 2015/2016/2017 with $\sqrt{s} = 13 \text{ TeV}$. Candidate $B_s^0 \rightarrow D_s K\pi\pi$
232 ($B_s^0 \rightarrow D_s \pi\pi\pi$) decays are reconstructed using the `B02DKPiPiD2HHHPIDBeauty2CharmLine`
233 (`B02DPiPiPiD2HHHPIDBeauty2CharmLine`) line of the `BHadronCompleteEvent` stream of
234 `Stripping21r1` (2011), `Stripping21` (2012), `Stripping24r1` (2015) and `Stripping28r1p1` (2016)
235 and `Stripping29r2` (2017). Both stripping lines employ the same selection cuts, listed in
236 Appendix B, except for the PID requirement on the bachelor kaon/pion.

237 Events that pass the stripping selection are further required to fulfill the following
238 trigger requirements: at the hardware stage, the B_s^0 candidates are required to be TOS
239 on the `L0Hadron` trigger or TIS on `L0Global`; at Hlt1, B_s^0 candidates are required to be
240 TOS on the `Hlt1TrackAllL0` (`Hlt1TrackMVA` or `Hlt1TwoTrackMVA`) trigger line for Run-I
241 (Run-II) data; at Hlt2, candidates have to be TOS on either one of the 2, 3 or 4-body
242 topological trigger lines or the inclusive ϕ trigger. More details on the used HLT lines are
243 given in Appendix B.

244 Due to a residual kinematic dependence on whether the event is triggered by `L0Hadron`
245 or not and on the data taking condition, the analysis is performed in four disjoint categories:
246 `[Run-I,L0-TOS]`, `[Run-I,L0-TIS]`, `[Run-II,L0-TOS]` and `[Run-II,L0-TIS]`, where for simplic-
247 ity we denote `L0Hadron-TOS` as `L0-TOS` and (`L0Global-TIS` and not `L0Hadron-TOS`) as
248 `L0-TIS`.

249 4.2 Offline selection

250 The offline selection, in particular the requirements on the D_s hadron, are guided by
251 the previous analyses of $B_s \rightarrow D_s K/\pi$, $B_d \rightarrow D^0 \pi$ as well as the branching fraction
252 measurement of $B_s^0 \rightarrow D_s K\pi\pi$ decays. Tables 4.1 and 4.2 summarize all selection
253 requirements which are described in the following. Throughout the note, we abbreviate
254 $B_s^0 \rightarrow D_s X_s (\rightarrow K\pi\pi)$ and $B_s^0 \rightarrow D_s X_d (\rightarrow \pi\pi\pi)$.

255 Given the high number of pp interactions per bunch crossing, a large fraction of
256 events have more than one reconstructed PV. We choose the 'best' PV to be the one
257 to which the B_s candidate has the smallest χ^2_{IP} . In instances where the association

of the B_s candidate to the best PV is wrong, the decay time of this candidate will be incorrect. These wrongly associated candidates are rejected by requiring that the B_s χ^2_{IP} with respect to any other PV is sufficiently higher than with respect to the best PV ($\Delta\chi^2_{IP} = \chi^2_{IP,\text{SECONDBEST}} - \chi^2_{IP,\text{BEST}} > 20$). Events with only a single PV are not affected.

In order to clean up the sample and to align the Run-I to the slightly tighter Run-II stripping selection, we apply the following loose cuts to the b-hadron:

- DIRA > 0.99994
- min IP $\chi^2 < 16$ to the best PV,
- FD $\chi^2 > 100$ to the best PV,
- Vertex $\chi^2/\text{nDoF} < 8$.

The cut on the B_s decay-time is tightened with respect to the stripping selection ($t > 0.2$ ps) because, while offline we use the decay-time determined for a DTF in which the PV position, the D_s and the B_s mass are constrained, in the stripping the simple decay-time returned by a kinematic fit is used. The difference between these two decay-times extends up to 0.1 ps, thus cutting at 0.4 ps avoids any boundary effects and simplifies the time-acceptance studies. We further remove outliers with poorly estimated decay times ($\delta t < 0.15$ ps).

We reconstruct the $B_s^0 \rightarrow D_s h \pi\pi$ decay through three different final states of the D_s meson: $D_s \rightarrow KK\pi$, $D_s \rightarrow \pi\pi\pi$ and $D_s \rightarrow K\pi\pi$. Of those, $D_s \rightarrow KK\pi$ is the most prominent one, while $\mathcal{BR}(D_s \rightarrow \pi\pi\pi) \approx 0.2 \cdot \mathcal{BR}(D_s \rightarrow KK\pi)$ and $\mathcal{BR}(D_s \rightarrow K\pi\pi) \approx 0.12 \cdot \mathcal{BR}(D_s \rightarrow KK\pi)$ holds for the others. For the $KK\pi$ final state we make use of the well known resonance structure; the decay proceeds either via the narrow ϕ resonance, the broader K^{*0} resonance or (predominantly) non-resonant. Within the ϕ resonance region the sample is already sufficiently clean after the stripping so that we do not impose additional criteria on the D_s daughters. For the K^{*0} and non-resonant regions consecutively tighter requirements on the particle identification and the D_s flight-distance are applied. We apply global requirements (*i.e.* independent of the D_s Dalitz-plot position) for the other final states. All cuts are summarized in Table 4.1.

4.2.1 Phase space region

Due to the comparably low masses of the final state particles with respect to the B_s mass, there is, in contrast to for example b-hadron to charmonia or charm decays, a huge phase-space available for the $B_s^0 \rightarrow D_s K\pi\pi$ decay. For the invariant mass of the $K\pi\pi$ subsystem it extends up to 3.4 GeV. It has however been observed that the decay proceeds predominantly through the low lying axial vector states $K_1(1270)$ and $K_1(1400)$, while the combinatorial background is concentrated at high $K\pi\pi$ invariant masses ($m(K\pi\pi) > 2000$ MeV). Moreover, the strange hadron spectrum above 2 GeV is poorly understood experimentally such that a reliable extraction of the strong phase motion in that region is not possible. We consequently choose to limit the considered phase space region to $m(K\pi\pi) < 1950$ MeV, which is right below the charm-strange threshold ($B_s^0 \rightarrow D_s^+ D_s^-$).

297 **4.2.2 Physics background vetoes**

298 We veto various physical backgrounds, which have either the same final state as our
 299 signal decay, or can contribute via a single misidentification of $K \leftrightarrow \pi$, $K \leftrightarrow p$ or $\pi \leftrightarrow p$.
 300 Depending on the D_s final state different vetoes are applied in order to account for peaking
 301 backgrounds originating from charm meson or charmed baryon decays.

302 1. $D_s^- \rightarrow K^+ K^- \pi^-$

303 (a) $D^- \rightarrow K^+ \pi^- \pi^-$:

304 Possible with $\pi^- \rightarrow K^-$ misidentification, vetoed by requiring $m(K^+ K_\pi^- \pi^-) \neq$
 305 $m(D^-) \pm 40$ MeV or the K^- has to fulfill more stringent PID criteria depending
 306 on the resonant region (see Table 4.1).

307 (b) $\Lambda_c^- \rightarrow K^+ \bar{p} \pi^-$:

308 Possible with $\bar{p} \rightarrow K^-$ misidentification, vetoed by requiring $m(K^+ K_p^- \pi^-) \neq$
 309 $m(\Lambda_c^-) \pm 40$ MeV or the K^- has to fulfill more stringent PID criteria depending
 310 on the resonant region (see Table 4.1).

311 (c) $D^0 \rightarrow KK$:

312 D^0 combined with a random π can fake a $D_s \rightarrow KK\pi$ decay, vetoed by
 313 requiring $m(KK) < 1840$ MeV.

314 2. $D_s^- \rightarrow \pi^+ \pi^- \pi^-$

315 (a) $D^0 \rightarrow \pi\pi$:

316 D^0 combined with a random π can fake a $D_s \rightarrow \pi\pi\pi$ decay, vetoed by requiring
 317 both possible combinations to have $m(\pi\pi) < 1700$ MeV.

318 3. $D_s^- \rightarrow K^- \pi^+ \pi^-$

319 (a) $D^- \rightarrow \pi^- \pi^+ \pi^-$:

320 Possible with $\pi^- \rightarrow K^-$ misidentification, vetoed by requiring $m(K_\pi^- \pi^+ \pi^-) \neq$
 321 $m(D^-) \pm 40$ MeV or $\text{PIDK}(K^+) > 15$.

322 (b) $\Lambda_c^- \rightarrow \bar{p} \pi^+ \pi^-$:

323 Possible with $\bar{p} \rightarrow K^-$ misidentification, vetoed by requiring $m(K_p^- \pi^+ \pi^-) \neq$
 324 $m(\Lambda_c^-) \pm 40$ MeV or $\text{PIDK}(K^-) - \text{PIDp}(K^-) > 5$.

325 (c) $D^0 \rightarrow K\pi$:

326 D^0 combined with a random π can fake a $D_s \rightarrow K\pi\pi$ decay, vetoed by requiring
 327 both possible combinations to have $m(K\pi) < 1750$ MeV.

328 The effects of these veto cuts are illustrated in Figs. 4.1,4.2 and 4.3. To reduce cross-feed
 329 from our calibration channel into the signal channel and vice-versa we require tight PID
 330 cuts on the ambiguous bachelor track; for the signal channel we apply $\text{PIDK}(K^+) > 10$
 331 and for the calibration channel $\text{PIDK}(\pi^+) < 0$. In addition, we veto $B_s^0 \rightarrow D_s^- D_s^+$ decays
 332 which is illustrated in Fig. 4.4.

- 333 1. $X_s^+ \rightarrow K^+\pi^+\pi^-$:
- 334 (a) $B_s^0 \rightarrow D_s\pi\pi\pi$:
 335 Possible with $\pi^+ \rightarrow K^+$ misidentification, suppressed with $\text{PIDK}(K^+) > 10$.
- 336 (b) $B_s^0 \rightarrow D_s^-(D_s^+ \rightarrow K^+\pi^+\pi^-)$:
 337 Outside of considered phase-space region, see Sec. 4.2.1.
- 338 (c) $B_s^0 \rightarrow D_s^-(D_s^+ \rightarrow K^+K^-\pi^+)$:
 339 To suppress $B_s^0 \rightarrow D_s^-K^+K^-\pi^+$ background, possible with $K^- \rightarrow \pi^-$ misiden-
 340 tification, we require $\text{PIDK}(\pi^-) < 0$. In case the invariant mass of the $K^+\pi^+\pi^-$
 341 system recomputed applying the kaon mass hypothesis to the pion is close to
 342 the D_s mass ($m(K^+\pi^+\pi_K^-) = m(D_s) \pm 20$ MeV), we further tighten the cut to
 343 $\text{PIDK}(\pi^-) < -5$.
- 344 2. $X_d^+ \rightarrow \pi^+\pi^+\pi^-$:
- 345 (a) $B_s^0 \rightarrow D_sK\pi\pi$:
 346 Possible with single missID of $K^+ \rightarrow \pi^+$, suppressed with $\text{PIDK}(\pi^+) < 0$.
- 347 (b) $B_s^0 \rightarrow D_s^-(D_s^+ \rightarrow \pi^+\pi^+\pi^-)$:
 348 Outside of considered phase-space region, see Sec. 4.2.1.
- 349 (c) $B_s^0 \rightarrow D_s^-(D_s^+ \rightarrow K^+\pi^-\pi^+)$:
 350 Possible with single missID of $K^+ \rightarrow \pi^+$, vetoed by requiring $m(\pi^+\pi_K^+\pi^-) \neq$
 351 $m(D_s) \pm 20$ MeV or $\text{PIDK}(\pi^+) < -5$ for both π^+ .

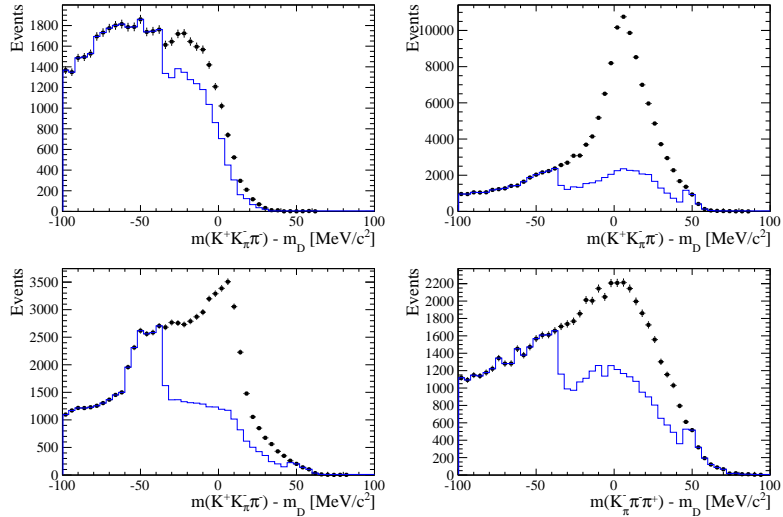


Figure 4.1: Background contributions from D^- decays where the π^- is misidentified as K^- . The D_s invariant mass is recomputed applying the pion mass hypothesis to the kaon and shown for the $D_s \rightarrow \phi\pi$, $D_s \rightarrow K^*(892)K$, $D_s \rightarrow KK\pi$ (non-resonant) and $D_s \rightarrow K\pi\pi$ final state categories from top-left to bottom-right. The distributions are shown without (black) and with (blue) the D^- -veto applied.

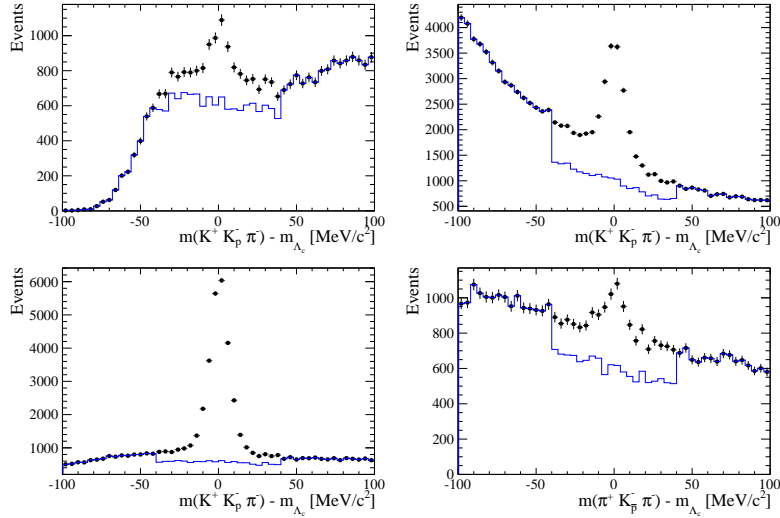


Figure 4.2: Background contributions from Λ_c decays where the \bar{p} is misidentified as K^- . The D_s invariant mass is recomputed applying the proton mass hypothesis to the kaon and shown for the $D_s \rightarrow \phi\pi$, $D_s \rightarrow K^*(892)K$, $D_s \rightarrow KK\pi$ (non-resonant) and $D_s \rightarrow K\pi\pi$ final state categories from top-left to bottom-right. The distributions are shown without (black) and with (blue) the Λ_c -veto applied.

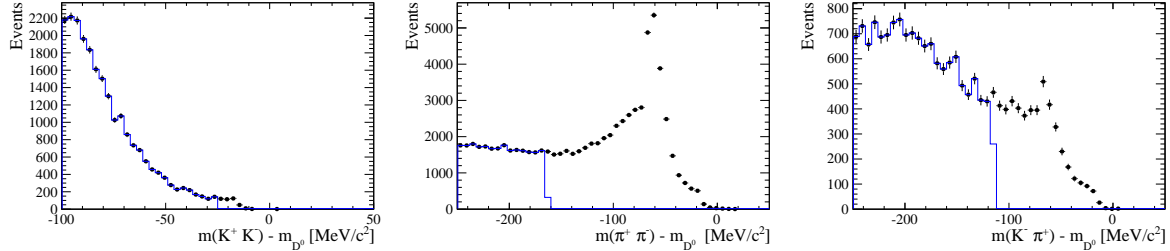


Figure 4.3: Background contributions to $D_s \rightarrow KK\pi$ (left), $D_s \rightarrow \pi\pi\pi$ (middle) and $D_s \rightarrow K\pi\pi$ (right) from $D^0 \rightarrow hh$ decays combined with a random pion. The peak at $m(\pi\pi) - m(D^0) \approx -60$ MeV ($m(K\pi) - m(D^0) \approx -60$ MeV) are due to $D^0 \rightarrow K\pi$ ($D^0 \rightarrow KK$) where a kaon is misidentified as pion.

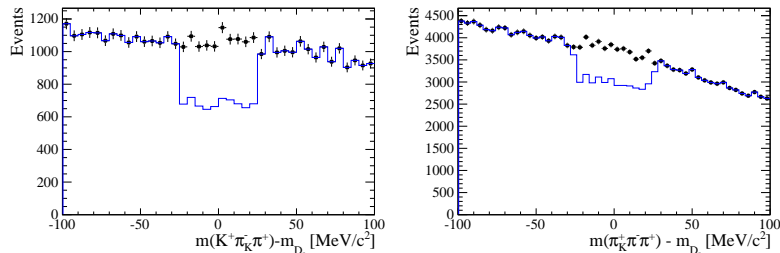


Figure 4.4: Background contributions to $B_s \rightarrow D_s K\pi\pi$ (left) and $B_s \rightarrow D_s \pi\pi\pi$ (right) from $B_s \rightarrow D_s D_s$ decays where the kaon is misidentified as pion. The $X_{s,d}$ invariant mass is recomputed applying the kaon mass hypothesis to the pion and shown without (black) and with (blue) the D_s -veto applied.

352 **4.2.3 Training of multivariate classifier**

353 The Toolkit for Multivariate Analysis (TMVA [26]) is used to train a multivariate classifier
 354 (BDT with gradient boosting, BDTG) discriminating signal and combinatorial background.
 355 We use $B_s \rightarrow D_s \pi\pi$ data that passes all previously mentioned selection steps, including
 356 the trigger and stripping selection, offline cuts and physical background vetoes, as signal
 357 proxy. The background is statistically subtracted by applying `sWeights` based on the
 358 fit to the reconstructed B_s mass shown in Fig. 4.5(left). This is a simplified version
 359 (performed in a reduced mass range) of the final mass fits described in Sec. 5. The
 360 sideband $B_s \rightarrow D_s K\pi\pi$ data ($m(B_s) > 5500$ MeV) is used as background proxy.

361 Training the classifier on a sub-sample which is supposed to be used in the final analysis
 362 might cause a bias, as the classifier selects, in case of overtraining, the training events
 363 more efficiently. As overtraining can not be completely avoided, we split the signal and
 364 the background training samples into two disjoint subsamples according to whether the
 365 event number is even or odd. We then train the classifier on the even sample and apply it
 366 to the odd one, and vice-versa (cross-training).

367 The following discriminating variables are used for the BDTG training¹:

- 368 • logarithm of the B_s impact-parameter χ^2 , $B_s \log(\chi_{IP}^2)$
- 369 • logarithm of the cosine of the B_s direction angle, $\log(\text{DIRA})$
- 370 • fit quality of the DTF with PV constrain, χ_{DTF}^2/ndf
- 371 • logarithm of the minimal B_s^0 decay vertex quality difference for adding one extra
 372 track, $\log(\Delta\chi_{add-track}^2)$
- 373 • the difference between the transverse momentum of the B_s - candidate and the
 374 transverse momentum of all the particles reconstructed with a cone of radius
 375 $r = \sqrt{(\Delta\Phi)^2 + (\Delta\eta)^2} < 1$ rad around the B_s - candidate normalized to the sum of
 376 both, $B_s A_{pT}^{\text{cone}}$
- 377 • largest ghost probability of all tracks, $\max(\text{ghostProb})$
- 378 • logarithm of the the smallest $X = X_d, X_s$ daughter impact-parameter χ^2 , $X \log(\min(\chi_{IP}^2))$
- 379 • largest distance of closest approach of the $X = X_d, X_s$ daughters, $\max(\text{DOCA})$
- 380 • cosine of the largest opening angle between the D_s and another bachelor track h_i in
 381 the plane transverse to the beam, $\cos(\max \theta_{D_s h_i})$
- 382 • logarithm of the the smallest D_s daughter impact-parameter χ^2 , $D_s \log(\min(\chi_{IP}^2))$
- 383 • logarithm of the D_s flight-distance significance, $D_s \log(\chi_{FD}^2)$
- 384 • logarithm of the D_s radial flight-distance, $D_s \log(RFD)$

¹ The following options are chosen: NTrees=500, MinNodeSize=2.5%, BoostType=Grad:Shrinkage=0.10, UseBaggedBoost:BaggedSampleFraction=0.5, nCuts=40, MaxDepth=3, NegWeightTreatment=Pray.

386 Loose cuts on the variables χ^2_{DTG}/ndf , $\Delta\chi^2_{add-track}$ and $\cos(\max\theta_{D_s h_i})$ are applied prior
 387 to the training which are expected to be 100% signal efficient. Figure 4.6 shows the
 388 distributions of the input variables for signal and background. As shown in Appendix C,
 389 these distributions differ between data-taking period and trigger category. In particular
 390 variables depending on the B_s kinematics and the event multiplicity are affected (*e.g.*
 391 $\theta_{D_s h_i}$ or A_{pT}^{cone}). The BDTG is consequently trained separately for these categories. The
 392 resulting classifier response is shown in Fig. 4.7 for each category (even and odd test
 393 samples combined) and in Appendix C for each training.

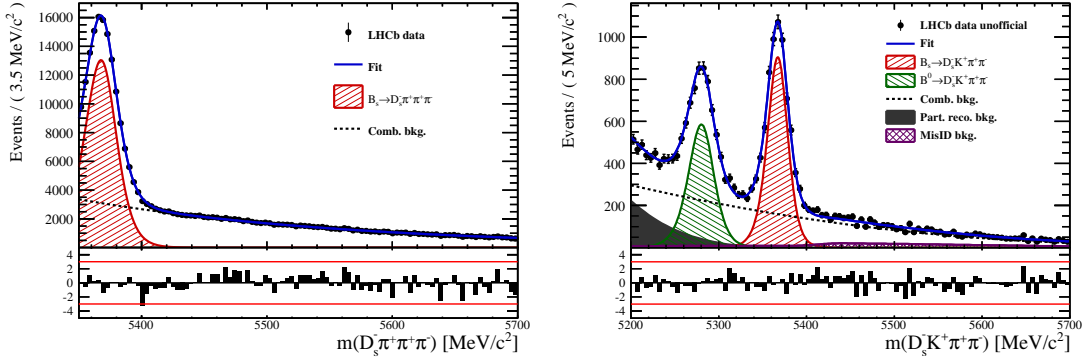


Figure 4.5: Left: Reconstructed B_s mass for $B_s \rightarrow D_s \pi\pi\pi\pi$ events that pass the preselection (all categories combined). The fitted PDF is shown in blue, the signal component in red and the background component in black.

Right: Reconstructed B_s mass for $B_s \rightarrow D_s K\pi\pi$ events that pass the $BDTG > 0$ requirement (all categories combined).

394 4.2.4 Final selection

395 The cut on the BDTG output is optimized using the signal significance as figure of merit:

$$FOM(BDTG) = \frac{N_s(BDTG)}{\sqrt{N_s(BDTG) + N_b(BDTG)}} \quad (4.1)$$

396 where $N_s(BDTG)$ is the $B_s \rightarrow D_s K\pi\pi$ signal yield for a given BDTG cut and $N_b(BDTG)$
 397 is the combinatorial background yield in the signal region ($m(D_s K\pi\pi) = m_{B_s} \pm 40$ MeV).
 398 To compute the yields as function of the BDTG cut, we use the BDTG efficiencies, $\epsilon_{s,b}$,
 399 evaluated on the corresponding test samples. To fix the overall scale, it is required to
 400 know the yields at (at least) one point of the scanned range. We arbitrarily choose this
 401 fix point to be $BDTG > 0$ and perform a fit to the reconstructed B_s mass as described
 402 in Sec. 5 to obtain the yields $N_{s,b}(0)$, see Fig. 4.5(right). These yields are then efficiency
 403 corrected to calculate the yields for a given BDTG cut:

$$N_{s,b}(BDTG) = N_{s,b}(0) \cdot \frac{\epsilon_{s,b}(BDTG)}{\epsilon_{s,b}(0)}. \quad (4.2)$$

404 Figure 4.8 shows the resulting BDTG scans for each training category.

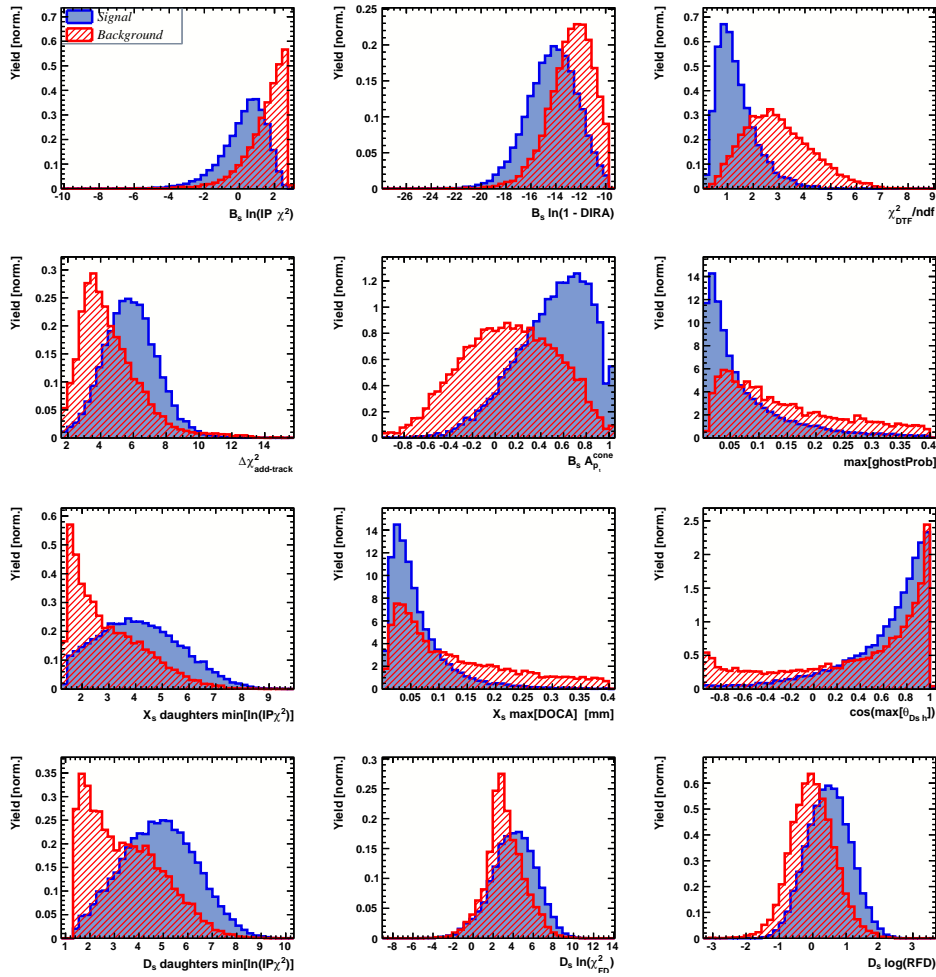


Figure 4.6: Discriminating variables used to train the BDTG for all data categories combined.

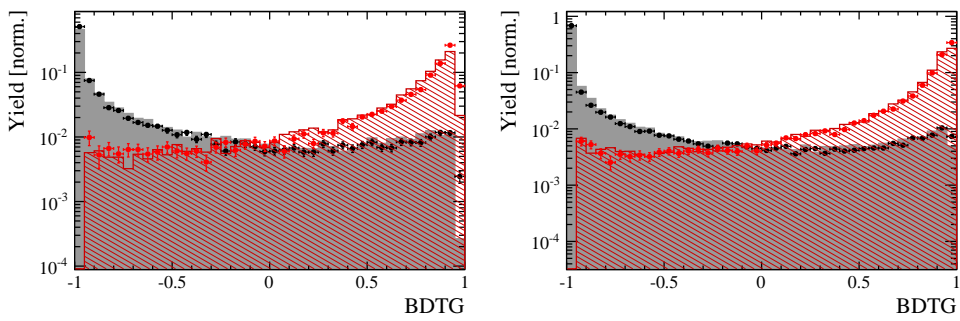


Figure 4.7: Signal (red) and background (black) distributions for the BDTG response for Run-I (left) and Run-II (right) data. Filled histograms (data points) show the BDTG response for the L0-TOS (L0-TIS) category. Even and odd test samples are combined.

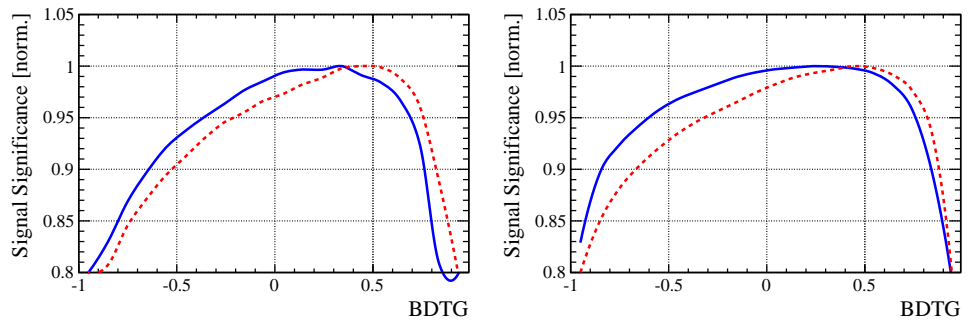


Figure 4.8: Signal significance as function of the applied cut on the BDTG response for Run-I (left) and Run-II (right) data. The scans for the L0-TOS (L0-TIS) category are shown in blue (red). The signal significance is normalized to be 1 at the optimal BDTG cut value.

Table 4.1: Offline selection requirements for $D_s \rightarrow 3h$ candidates.

	Description	Requirement
$D_s \rightarrow hh\bar{h}$	$m(hh\bar{h})$	$= m_{D_s} \pm 25$ MeV
$D_s^- \rightarrow KK\pi^-$	D^0 veto	$m(KK) < 1840$ MeV
$D_s^- \rightarrow \phi\pi^-$	$m(KK)$ PIDK(K^+) PIDK(K^-) PIDK(π^-) χ_{FD}^2 FD in z D^- veto Λ_c veto	$= m_\phi \pm 12$ MeV > -10 > -10 < 20 > 0 > -1 $m(K^+K_\pi^-\pi^-) \neq m(D^-) \pm 40$ MeV PIDK(K^-) > 5 $m(K^+K_p^-\pi^-) \neq m(\Lambda_c) \pm 40$ MeV PIDK(K^-) – PIDp(K^-) > 2
$D_s^- \rightarrow K^*(892)K^-$	$m(KK)$ $m(K^+\pi^-)$ PIDK(K^+) PIDK(K^-) PIDK(π^-) χ_{FD}^2 FD in z D^- veto Λ_c veto	$\neq m_\phi \pm 12$ MeV $= m_{K^*(892)} \pm 75$ MeV > -10 > 0 < 10 > 0 > 0 $m(K^+K_\pi^-\pi^-) \neq m(D^-) \pm 40$ MeV PIDK(K^-) > 15 $m(K^+K_p^-\pi^-) \neq m(\Lambda_c) \pm 40$ MeV PIDK(K^-) – PIDp(K^-) > 5
$D_s^- \rightarrow (KK\pi^-)_{NR}$	$m(KK)$ $m(K^+\pi^-)$ PIDK(K^+) PIDK(K^-) PIDK(π^-) χ_{FD}^2 FD in z D^- veto Λ_c veto	$\neq m_\phi \pm 12$ MeV $\neq m_{K^*(892)} \pm 75$ MeV > 5 > 5 < 10 > 4 > 0 $m(K^+K_\pi^-\pi^-) \neq m(D^-) \pm 40$ MeV PIDK(K^-) > 15 $m(K^+K_p^-\pi^-) \neq m(\Lambda_c) \pm 40$ MeV PIDK(K^-) – PIDp(K^-) > 5
$D_s^- \rightarrow \pi\pi\pi$	PIDK(π) PIDp(π) D^0 veto χ_{FD}^2 FD in z	< 10 < 20 $m(\pi^+\pi^-) < 1700$ MeV > 9 > 0
$D_s^- \rightarrow K^-\pi^+\pi^-$	PIDK(K) PIDK(π) PIDp(π) D^0 veto χ_{FD}^2 FD in z D^- veto Λ_c veto	> 8 < 5 < 20 $m(K^-\pi^+) < 1750$ MeV > 9 > 0 $m(K_\pi^-\pi^+\pi^-) \neq m(D^-) \pm 40$ MeV PIDK(K^-) > 15 $m(K_p^-\pi^+\pi^-) \neq m(\Lambda_c) \pm 40$ MeV PIDK(K^-) – PIDp(K^-) > 5

Table 4.2: Offline selection requirements for $B_s \rightarrow D_s K\pi\pi(D_s\pi\pi\pi)$ candidates.

	Description	Requirement
$B_s \rightarrow D_s h\pi\pi$	$m(D_s h\pi\pi)$	$> 5200 \text{ MeV}$
	χ^2_{vtx}/ndof	< 8
	DIRA	> 0.99994
	χ^2_{FD}	> 100
	χ^2_{IP}	< 16
	χ^2_{DTF}/ndof	< 15
	$\Delta\chi^2_{add-track}$	> 2
	$\cos(\max \theta_{D_s h_i})$	> -0.9
	t	$> 0.4 \text{ ps}$
	δt	$< 0.15 \text{ ps}$
	Phasespace region	$m(h\pi\pi) < 1.95 \text{ GeV}$ $m(h\pi) < 1.2 \text{ GeV}$ $m(\pi\pi) < 1.2 \text{ GeV}$
Wrong PV veto		$\text{nPV} = 1 \parallel \min(\Delta\chi^2_{IP}) > 20$
BDTG		$> 0.35 \text{ [Run-I,L0-TOS]}$ $> 0.45 \text{ [Run-I,L0-TIS]}$ $> 0.25 \text{ [Run-II,L0-TOS]}$ $> 0.45 \text{ [Run-II,L0-TIS]}$
$X_s^+ \rightarrow K^+\pi^+\pi^-$	PIDK(K)	> 10
	PIDK(π^+)	< 10
	PIDK(π^-)	< 0
	D_s veto	$m(K^+\pi^+\pi_K^-) \neq m(D_s) \pm 20 \text{ MeV} \parallel \text{PIDK}(\pi^-) < -5$
$X_d^+ \rightarrow \pi^+\pi^+\pi^-$	PIDK(π^+)	< 0
	PIDK(π^-)	< 10
	D_s veto	$m(\pi^+\pi_K^+\pi^-) \neq m(D_s) \pm 20 \text{ MeV} \parallel \text{PIDK}(\pi^+) < -5$
All tracks	hasRich	$= 1$

405 4.3 Simulation

406 Several Monte Carlo (MC) samples are used in the analysis for acceptance and background
 407 studies. A full list of them is given in Tab. 4.3. In each case, the decay model includes
 408 a mixture of non-interfering resonances contributing to the bachelor system and a non-
 409 resonant (phase-space) component. For $B_s \rightarrow D_s X_s$ these are: 25% $X_s \rightarrow \pi(K_1(1270) \rightarrow$
 410 $K\rho(770))$, 70% $X_s \rightarrow \pi(K_1(1400) \rightarrow K^*(892)\pi)$ and 5% $X_s \rightarrow K\pi\pi$ (non-resonant). And
 411 similar for $B_s \rightarrow D_s X_d$: 85% $X_d \rightarrow \pi(a_1(1260) \rightarrow \rho(770)\pi)$, 10% $X_d \rightarrow \pi(a_1(1260) \rightarrow \sigma\pi)$
 412 and 5% $X_d \rightarrow K\pi\pi$ (non-resonant). All MC samples are generated using Pythia8,
 413 reconstructed using Reco14c, Reco15 and Reco16 for Run-I, 15 and 16 data and selected
 414 using the same criteria as in data.

Table 4.3: List of simulated samples used in the analysis.

Decay	Event Type	Sim	Statistics				Filter
			11	12	15	16	
$B_s \rightarrow (D_s \rightarrow KK\pi)K\pi\pi$	13266007	08i	1.2 M	1.2 M	-	-	Generator Level
$B_s \rightarrow (D_s \rightarrow KK\pi)K\pi\pi$	13266008	09c	70 k	80 k	50 k	100 k	Generator Level, Stripping
$B_s \rightarrow (D_s \rightarrow K\pi\pi)K\pi\pi$	13266058	09c	70 k	80 k	50 k	100 k	Generator Level, Stripping
$B_s \rightarrow (D_s \rightarrow \pi\pi\pi)K\pi\pi$	13266038	09c	70 k	80 k	50 k	100 k	Generator Level, Stripping
$B_s \rightarrow (D_s \rightarrow KK\pi)\pi\pi\pi$	13266006	08i	1.2 M	1.2 M	-	-	Generator Level
$B_s \rightarrow (D_s \rightarrow KK\pi)\pi\pi\pi$	13266068	09c	70 k	80 k	50 k	100 k	Generator Level, Stripping
$B_s \rightarrow (D_s \rightarrow K\pi\pi)\pi\pi\pi$	13266088	09c	70 k	80 k	50 k	100 k	Generator Level, Stripping
$B_s \rightarrow (D_s \rightarrow \pi\pi\pi)\pi\pi\pi$	13266078	09c	70 k	80 k	50 k	100 k	Generator Level, Stripping
$B_s \rightarrow D_s^*\pi\pi\pi, D_s \rightarrow KK\pi$	13266201	08i	1.2 M	1.2 M	-	-	Generator Level

415 5 Yields determination

416 An extended unbinned maximum likelihood fit to the reconstructed B_s mass of the selected
 417 events is performed in order to determine the signal and background yields. The invariant
 418 mass $m(D_s h\pi\pi)$ is determined from a DTF constraining the mass of the D_s to the PDG
 419 value and the position of the PV. The probability density functions (PDFs) used to
 420 describe the signal and background components are described in the following.

421 Due to different mass resolutions, we perform the invariant mass fits simultaneously
 422 for each data-taking period and each trigger category. We further introduce four D_s final
 423 state categories: $D_s \rightarrow \phi\pi$, $D_s \rightarrow K^*(892)\pi$, $D_s \rightarrow \pi\pi\pi$ and $D_s \rightarrow Kh\pi$ to account for
 424 different signal purities. The $D_s \rightarrow Kh\pi$ category combines the two D_s decay channels
 425 with the lowest statistics: $D_s \rightarrow KK\pi$ (non-resonant) and $D_s \rightarrow K\pi\pi$. This amounts to
 426 16 categories in total.

427 5.1 Signal model

428 The signal B_s -mass distribution of both $B_s^0 \rightarrow D_s K\pi\pi$ and $B_s^0 \rightarrow D_s \pi\pi\pi$ is modeled
 429 using a Johnson's SU function [27], which results from a variable transformation of a
 430 normal distribution to allow for asymmetric tails:

$$\mathcal{J}(x|\mu, \sigma, \nu, \tau) = \frac{e^{-\frac{1}{2}r^2}}{2\pi \cdot c \cdot \sigma \cdot \tau \cdot \sqrt{z^2 + 1}} \quad (5.1)$$

$$r = -\nu + \frac{\operatorname{asinh}(z)}{\tau} \quad (5.2)$$

$$z = \frac{x - (\mu - c \cdot \sigma \cdot e^\tau \sinh(\nu \cdot \tau))}{c \cdot \tau} \quad (5.3)$$

$$c = \frac{e^{\tau^2} - 1}{2\sqrt{e^{\tau^2} \cdot \cosh(2\nu \cdot \tau) + 1}}. \quad (5.4)$$

431 It is conveniently expressed in terms of the central moments up to order four: The mean
 432 of the distribution μ , the standard deviation σ , the skewness ν and the kurtosis τ . The
 433 tail parameters ν and τ are fixed to the values obtained by a fit to the invariant mass
 434 distribution of simulated events shown in Fig 5.1. To account for differences between
 435 simulation and real data, linear scaling factors for the mean μ and width σ are determined
 436 in the fit to $B_s^0 \rightarrow D_s \pi\pi\pi$ data and later fixed in the fit to $B_s^0 \rightarrow D_s K\pi\pi$ decays. The scale
 437 factors are determined separately for each data-taking period and each trigger category.

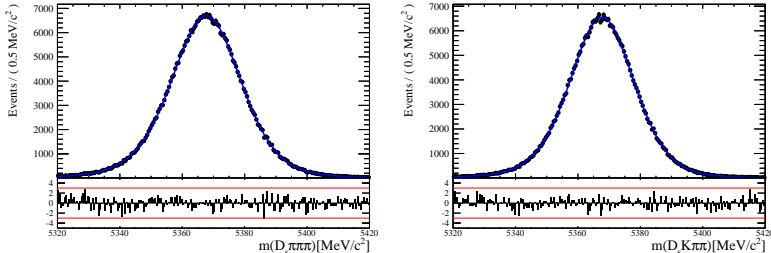


Figure 5.1: Invariant mass distributions of simulated (left) $B_s^0 \rightarrow D_s \pi\pi\pi$ and (right) $B_s^0 \rightarrow D_s K\pi\pi$ events. A fit with a Johnson's SU PDF is overlaid.

438 **5.2 Background models**

439 After the full selection the following residual background components have to be accounted
440 for:

441

442 **Combinatorial background**

443 The combinatorial background is described by a second order polynomial, whose
444 parameters are determined, for each D_s final state separately, in the fit to data. For
445 systematic studies an exponential PDF is used.

446

447 **Peaking B_d background**

448 Decays of B_d mesons into the $D_s h\pi\pi$ final state are described by the B_s signal PDF
449 where the mean is shifted by the known mass difference $m_{B_s} - m_{B_d}$ [15].

450

451 **Partially reconstructed background**

452 Partially reconstructed $B_s^0 \rightarrow D_s^* \pi\pi\pi$ decays, with $D_s^* \rightarrow D_s \gamma$ or $D_s^* \rightarrow D_s \pi^0$, are expected
453 to be peaking lower than signal in the $m(D_s \pi\pi\pi)$ spectrum with large tails due to the
454 momentum carried away by the not reconstructed π^0 or γ . An empirical description for
455 the shape of this contribution is derived from a $B_s^0 \rightarrow D_s^* \pi\pi\pi$ MC sample subject to
456 the nominal $B_s^0 \rightarrow D_s \pi\pi\pi$ selection. Figure 5.2 (top) shows the respective reconstructed
457 $m(D_s \pi\pi\pi)$ distribution. A sum of three bifurcated Gaussian functions (*i.e.* Gaussian
458 functions with different widths on the left and the right side of the maximum value) is used
459 to describe it. In the fit to data, all parameters are fixed to the ones obtained from MC
460 except for the parameter which describes the width of the right tail of the distribution to
461 account for data-simulation differences in mass resolution. The equivalent $B_s^0 \rightarrow D_s^* K\pi\pi$
462 component contributing to the $B_s^0 \rightarrow D_s K\pi\pi$ data sample is described by the same PDF
463 with the right tail fixed to the $B_s^0 \rightarrow D_s \pi\pi\pi$ result.

464 Contributions from $B^0 \rightarrow D_s^* K\pi\pi$ decays are modeled with the $B_s^0 \rightarrow D_s^* K\pi\pi$ PDF
465 shifted by $m_{B_s^0} - m_{B^0}$.

466

467 **Misidentified background**

468 A small fraction of $B_s \rightarrow D_s^- \pi^+ \pi^+ \pi^-$ and $B_s^0 \rightarrow D_s^* \pi^+ \pi^+ \pi^-$ decays, where one of the
469 pions is misidentified as a kaon, contaminate the $B_s^0 \rightarrow D_s K^+ \pi^+ \pi^-$ sample. To determine
470 the corresponding background shapes, we use simulated events passing the nominal
471 selection except for the PID cuts on the bachelor π^+ tracks. The **PIDCalib** package
472 is used to determine the p_T, η -dependent $\pi^+ \rightarrow K^+$ misidentification probability for
473 each pion. We change the particle hypothesis from pion to kaon for the pion with the
474 higher misidentification probability and recompute the invariant B_s^0 mass, $m(D_s^- \pi_K^+ \pi^+ \pi^-)$.
475 Similarly, the invariant masses $m(\pi_K^+ \pi^+ \pi^-)$ and $m(\pi_K^+ \pi^-)$ are recomputed and required
476 to be within the considered phasespace region. The background distributions are shown
477 in Fig. 5.2 (middle, bottom) and modeled by the sum of three Crystal Ball functions.

478 The expected yield of misidentified $B_s^0 \rightarrow D_s\pi\pi\pi$ ($B_s^0 \rightarrow D_s^*\pi^+\pi^+\pi^-$) candidates in
 479 the $B_s^0 \rightarrow D_sK\pi\pi$ sample is computed by multiplying the fake rate (within the considered
 480 B_s mass range) of $0.63 \pm 0.01\%$ ($0.55 \pm 0.02\%$) for Run-I and $0.33 \pm 0.01\%$ ($0.24 \pm 0.01\%$)
 481 for Run-II by the $B_s^0 \rightarrow D_s\pi\pi\pi$ ($B_s^0 \rightarrow D_s^*\pi^+\pi^+\pi^-$) yield as determined in the mass
 482 fit to the $B_s^0 \rightarrow D_s\pi\pi\pi$ data sample. The yields are corrected for the $\text{PID}(\pi^+) < 0$
 483 requirement which has an efficiency of $77.1 \pm 0.1\%$ for Run-I and $81.0 \pm 0.1\%$ for Run-II
 484 data. The $B_s^0 \rightarrow D_s^*\pi^+\pi^+\pi^-$ yield is additionally corrected for the efficiency of the cut
 485 $m(D_sK\pi\pi) > 5200 \text{ MeV}$ evaluated on MC. In the fit to data, the misidentified background
 486 yields are fixed to the predicted ones.

487 We consider the $B_s^0 \rightarrow D_sK\pi\pi$ and $B_s^0 \rightarrow D_s^*K\pi\pi$ components contributing to the
 488 $B_s^0 \rightarrow D_s\pi\pi\pi$ data sample to be negligible due to the low branching fractions and the
 489 tight PID cuts on the bachelor pions.

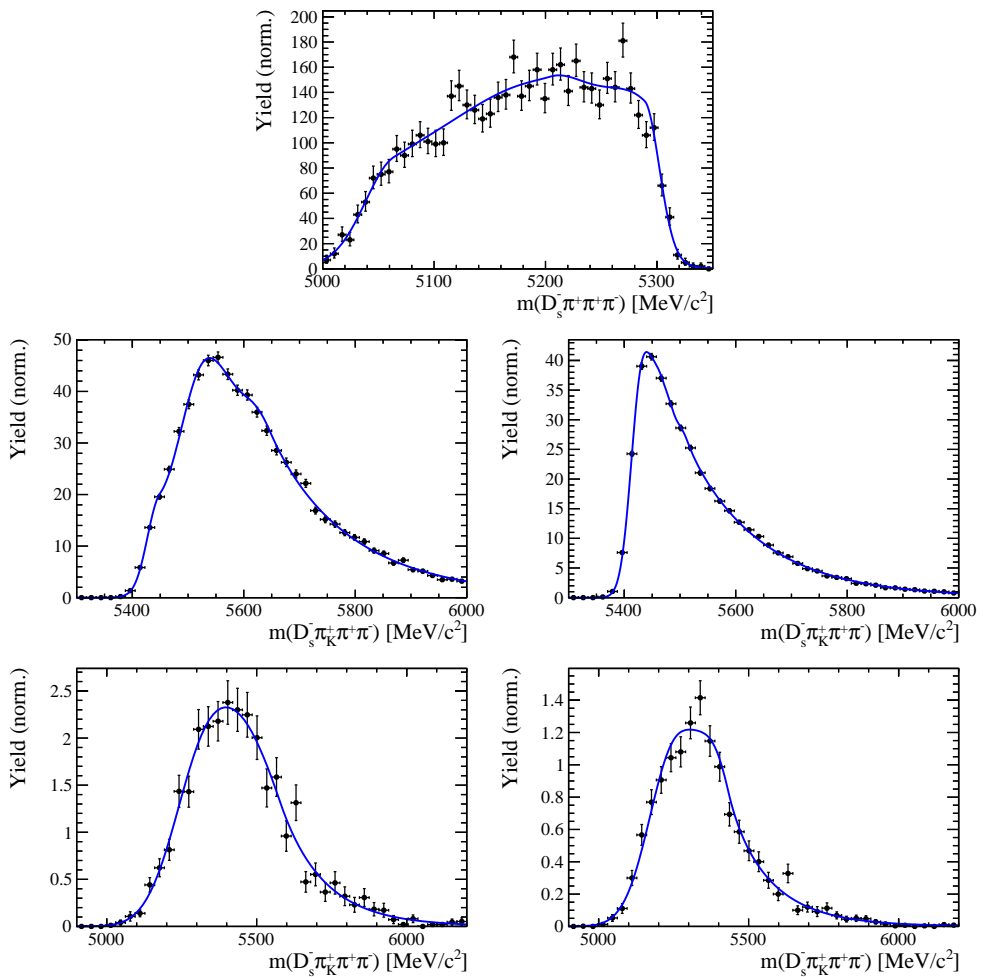


Figure 5.2: Top: Invariant mass distribution of simulated $B_s^0 \rightarrow D_s^*\pi\pi\pi$ events, where the γ/π^0 is excluded from the reconstruction. Middle: Invariant mass distribution of simulated $B_s^0 \rightarrow D_s\pi\pi\pi$ events for Run-I (left) and Run-II (right), where one of the pions is reconstructed as a kaon taking the misidentification probability into account. Bottom: Invariant mass distribution for simulated $B_s^0 \rightarrow D_s^*\pi\pi\pi$ events for Run-I (left) and Run-II (right), where the γ/π^0 from the D_s^* is excluded from reconstruction and one of the pions is reconstructed as a kaon taking the misidentification probability into account. The fitted PDFs are shown in blue.

490 5.3 Results

491 Figure 5.3 shows the invariant mass distribution for $B_s^0 \rightarrow D_s\pi\pi\pi$ and $B_s^0 \rightarrow D_sK\pi\pi$ can-
 492 didates passing all selection criteria. The projections for all categories of the simultaneous
 493 fit are shown in Appendix D. The integrated signal and background yields are listed in
 494 Tables 5.1 and 5.2.

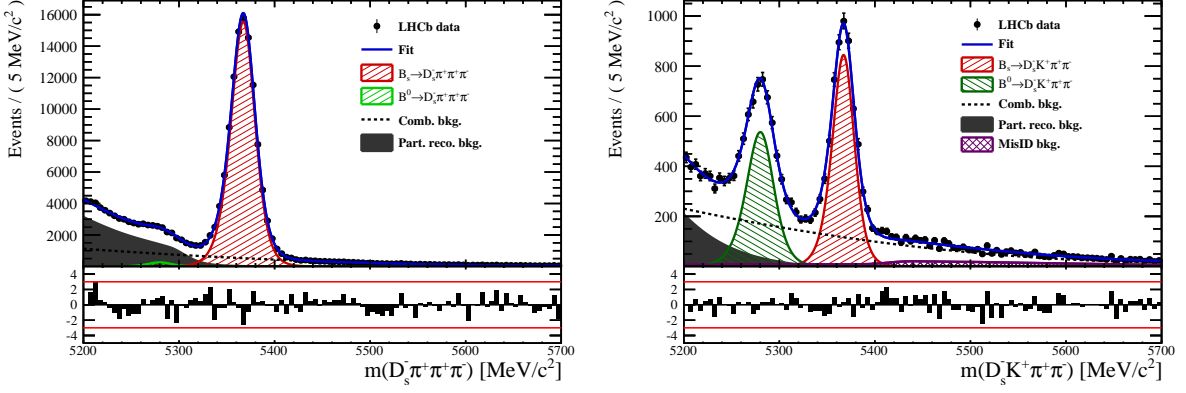


Figure 5.3: Invariant mass distribution of $B_s^0 \rightarrow D_s\pi\pi\pi$ (left) and $B_s^0 \rightarrow D_sK\pi\pi$ (right) candidates integrated over all categories.

Table 5.1: Total signal and background yields for the $B_s \rightarrow D_s\pi\pi\pi$ sample (left) and signal yield for the different D_s final states contributing to the $B_s \rightarrow D_s\pi\pi\pi$ sample (right).

Component	Yield
$B_s \rightarrow D_s\pi\pi\pi$	104176 ± 356
$B^0 \rightarrow D_s\pi\pi\pi$	1742 ± 363
Partially reconstructed bkg.	43157 ± 407
Combinatorial bkg.	40992 ± 455

D_s final state	Signal yield
$D_s^- \rightarrow \phi^0(1020)\pi^-$	35429 ± 202
$D_s^- \rightarrow K^{*0}(892)K^-$	29388 ± 194
$D_s^- \rightarrow (K^- h^+\pi^-)$	21695 ± 164
$D_s^- \rightarrow \pi^+\pi^-\pi^-$	17665 ± 148

Table 5.2: Total signal and background yields for the $B_s \rightarrow D_sK\pi\pi$ sample (left) and signal yield for the different D_s final states contributing to the $B_s \rightarrow D_sK\pi\pi$ sample (right).

Component	Yield
$B_s \rightarrow D_sK\pi\pi$	5172 ± 88
$B^0 \rightarrow D_sK\pi\pi$	4109 ± 100
Partially reconstructed bkg.	1825 ± 204
Misidentified bkg.	1186 ± 0
Combinatorial bkg.	9172 ± 221

D_s final state	Signal yield
$D_s^- \rightarrow \phi^0(1020)\pi^-$	1637 ± 47
$D_s^- \rightarrow K^{*0}(892)K^-$	1537 ± 47
$D_s^- \rightarrow (K^- h^+\pi^-)$	1134 ± 41
$D_s^- \rightarrow \pi^+\pi^-\pi^-$	864 ± 41

495 6 Decay-time Resolution

496 The observed oscillation of B mesons is prone to dilution, if the detector resolution is
 497 of similar magnitude as the oscillation period. In the B_s^0 system, considering that the
 498 measured oscillation frequency of the B_s^0 [28] and the average LHCb detector resolution [29]
 499 are both $\mathcal{O}(50 \text{ fs}^{-1})$, this is the case. Therefore, it is crucial to correctly describe the
 500 decay time resolution in order to avoid a bias on the measurement of time dependent CP
 501 violation. Since the time resolution depends on the particular event, especially the decay
 502 time itself, the sensitivity on γ can be significantly improved by using an event dependent
 503 resolution model rather than an average resolution. For this purpose, we use the per-event
 504 decay time error that is estimated based on the uncertainty obtained from the global
 505 kinematic fit of the momenta and vertex positions (DTF) with additional constraints on
 506 the PV position and the D_s mass. In order to apply it correctly, it has to be calibrated.
 507 The raw decay time error distributions for $B_s^0 \rightarrow D_s\pi\pi\pi$ signal candidates are shown in
 508 Figure 6.1 for Run-I and Run-II data. Significant deviations between the two different
 509 data taking periods are observed due to the increase in center of mass energy from Run-I
 510 to Run-II, as well as (among others) new tunings in the pattern and vertex reconstruction.
 511 The decay time error calibration is consequently performed separately for both data taking
 512 periods.

513 For Run-I data, we use the calibration from the closely related $B_s^0 \rightarrow D_s K$ analysis
 514 which was performed on a data sample of prompt- D_s candidates combined with a random
 515 pion track from the PV. We verify the portability to our decay channel on MC.

516 For Run-II data, a new lifetime unbiased stripping line (LTUB) has been implemented
 517 which selects prompt- D_s candidates combined with random $K\pi\pi$ tracks from the PV.

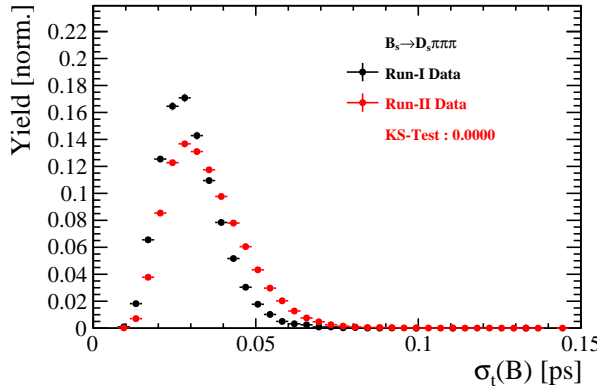


Figure 6.1: Distribution of the decay time error for $B_s^0 \rightarrow D_s\pi\pi\pi$ signal candidates for Run-I (black) and Run-II (red) data (sWeighted).

518 6.1 Calibration for Run-I data

519 For simulated $B_s^0 \rightarrow D_s K \pi\pi$ events, the spread of the differences between reconstructed
520 decay time and true decay time, $\Delta t = t - t_{true}$, is a direct measure of the decay time
521 resolution. The sum of two Gaussian pdfs with common mean but different widths is used
522 to fit the distribution of the decay time difference Δt as shown in Fig. 6.2. The effective
523 damping of the CP amplitudes due to the finite time resolution is described by the dilution
524 \mathcal{D} . In the case of infinite precision, there would be no damping and therefore $\mathcal{D} = 1$ would
525 hold, while for a resolution that is much larger than the B_s^0 oscillation frequency, \mathcal{D} would
526 approach 0. For a double-Gaussian resolution model, the dilution is given by [7]

$$\mathcal{D} = f_1 e^{-\sigma_1^2 \Delta m_s^2 / 2} + (1 - f_1) e^{-\sigma_2^2 \Delta m_s^2 / 2}, \quad (6.1)$$

527 where σ_1 and σ_2 are the widths of the Gaussians, f_1 is the relative fraction of events
528 described by the first Gaussian relative to the second and Δm_s is the oscillation frequency
529 of B_s^0 mesons. An effective single Gaussian width is calculated from the dilution as,

$$\sigma_{eff} = \sqrt{(-2/\Delta m_s^2) \ln \mathcal{D}}, \quad (6.2)$$

530 which converts the resolution into a single-Gaussian function with an effective resolution
531 that causes the same damping effect on the magnitude of the B_s oscillation. For the Run-I
532 $B_s^0 \rightarrow D_s K \pi\pi$ MC sample the effective average resolution is found to be $\sigma_{eff} = 39.1 \pm 0.3$ fs.

533 To analyze the relation between the per-event decay time error σ_t and the actual
534 resolution σ_{eff} , the simulated $B_s^0 \rightarrow D_s K \pi\pi$ sample is divided into equal-statistics slices
535 of σ_t . For each slice, the effective resolution is determined as described above. Details of
536 the fit results in each slice are shown in appendix E. Figure 6.2 shows the obtained values
537 for σ_{eff} as a function of the per-event decay time error σ_t . To account for the variable
538 binning, the bin values are not placed at the bin center but at the weighted mean of the
539 respective per-event-error bin. A linear function is used to parametrize the distribution.
540 The obtained values are

$$\sigma_{eff}^{MC}(\sigma_t) = (0.0 \pm 0.0) \text{ fs} + (1.232 \pm 0.010) \sigma_t \quad (6.3)$$

541 where the offset is fixed to 0. For comparison, the calibration function found for $B_s^0 \rightarrow D_s K$
542 MC is also shown in Figure 6.2 [7]:

$$\sigma_{eff}^{D_s K, MC}(\sigma_t) = (0.0 \pm 0.0) \text{ fs} + (1.201 \pm 0.013) \sigma_t. \quad (6.4)$$

543 Due to the good agreement between the scale factors for $B_s^0 \rightarrow D_s K$ and $B_s^0 \rightarrow D_s K \pi\pi$
544 MC, we conclude that the resolution calibration for $B_s^0 \rightarrow D_s K$ data [7]:

$$\sigma_{eff}^{D_s K}(\sigma_t) = (10.26 \pm 1.52) \text{ fs} + (1.280 \pm 0.042) \sigma_t \quad (6.5)$$

545 can be used for our analysis. The following calibration functions were used in the
546 $B_s^0 \rightarrow D_s K$ analysis to estimate the systematic uncertainty on the decay-time resolution:

$$\sigma_{eff}^{D_s K}(\sigma_t) = (-0.568 \pm 1.570) \text{ fs} + (1.243 \pm 0.044) \sigma_t \quad (6.6)$$

$$\sigma_{eff}^{D_s K}(\sigma_t) = (0.0 \pm 0.0) \text{ fs} + (1.772 \pm 0.012) \sigma_t \quad (6.7)$$

548 It was also observed in this analysis that the scale factor is largely independent of the B_s
549 kinematics and decay-time [6], consistent with other studies, for example in [30].

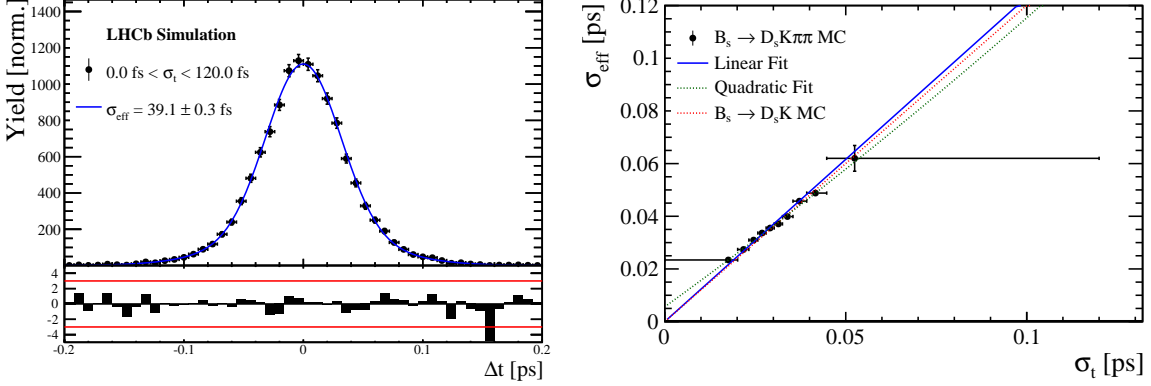


Figure 6.2: (Left) Difference of the true and measured decay time of $B_s^0 \rightarrow D_s K\pi\pi$ MC candidates. (Right) The measured resolution σ_{eff} as function of the per-event decay time error estimate σ_t for $B_s \rightarrow D_s K\pi\pi$ MC (Run-I). The fitted calibration curve is shown in blue.

550 6.2 Calibration for Run-II data

551 For the resolution calibration of Run-II data, a sample of promptly produced D_s candidates
 552 is selected using the B02DsKPiPiLTUBD2HHHBeauty2CharmLine stripping line. This
 553 lifetime-unbiased stripping line does not apply selection requirements related to lifetime
 554 or impact parameter, allowing for a study of the resolution. In order to reduce the rate
 555 of this sample it is pre-scaled in the stripping. Each D_s candidate is combined with a
 556 random kaon track and two random pion tracks which originate from the PV to obtain a
 557 sample of fake B_s candidates with a known true decay-time of $t_{true} = 0$. The difference of
 558 the measured decay time, t , of these candidates with respect to the true decay time is
 559 attributed to the decay time resolution.

560 The offline selection of the fake B_s candidates is summarized in Tab. 6.1. The selection
 561 is similar than the one for real data with the important difference that the D_s candidate
 562 is required to come from the PV by cutting on the impact parameter significance. Even
 563 after the full selection, a significant number of multiple candidates is observed. These
 564 are predominantly fake B_s candidates that share the same D_s candidate combined with
 565 different random tracks from the PV. We select one of these multiple candidates randomly
 566 which retains approximately 20% of the total candidates. As can be seen in Figure K.3,
 567 the shapes of the distributions of the unscaled decay time error σ_t for data taken in 2016
 568 and 2017 are significantly different. Therefore, the scaling of the decay time error is
 569 treated separately for 2015+2016 and 2017 data. The invariant mass distribution of the
 570 selected D_s candidates is shown in Fig. 6.3. To separate true D_s candidates from random
 571 combinations, the sPlot method is used to statistically subtract combinatorial background
 572 from the sample.

573 Figure 6.4 and 6.5 show the sWeighted decay-time distributions for fake B_s candidates
 574 from 2016 and 2017 data, respectively. Similar as in the previous section, the decay-time
 575 distribution is fitted with a double-Gaussian resolution model in slices of the per-event
 576 decay time error. Since some D_s candidates might actually originate from true B_s decays,
 577 the decay-time distribution of the fake B_s candidates might show a bias towards positive
 578 decay times. Therefore, we determine the decay-time resolution from the negative decay-
 579 time distribution only. Details of the fit results in each slice are shown in appendix E.

580 The resulting calibration functions are:

$$\sigma_{eff}^{Data,16}(\sigma_t) = (11.6 \pm 1.6) \text{ fs} + (0.877 \pm 0.040) \sigma_t \quad (6.8)$$

581

$$\sigma_{eff}^{Data,17}(\sigma_t) = (6.5 \pm 1.4) \text{ fs} + (0.961 \pm 0.036) \sigma_t \quad (6.9)$$

582 For 2016, the result is in good agreement with the one obtained for the $B_s \rightarrow J/\psi\phi$
583 (Run-II) analysis that uses 2016 data [31].

$$\sigma_{eff}^{J/\psi\phi}(\sigma_t) = (12.25 \pm 0.33) \text{ fs} + (0.8721 \pm 0.0080) \sigma_t \quad (6.10)$$

Table 6.1: Offline selection requirements for fake B_s candidates from promptly produced D_s candidates combined with random prompt $K\pi\pi$ bachelor tracks. The PID and veto cuts depending on the D_s final state and Dalitz plot position are the same as in Table. 4.1.

	Description	Requirement
$B_s \rightarrow D_s K\pi\pi$	χ_{vtx}^2/ndof	< 8
	χ_{DTF}^2/ndof	< 15
	t	< 0 ps
$D_s \rightarrow hh$	χ_{vtx}^2/ndof	< 5
	DIRA	> 0.99994
	χ_{FD}^2	> 9
	p_T	> 1800 MeV
	χ_{IP}^2	< 9
	$\chi_{IP}^2(h)$	> 5
Wrong PV veto	nPV = 1 min($\Delta\chi_{IP}^2$) > 20	
$X_s \rightarrow K\pi\pi$	$\chi_{IP}^2(h)$	< 40
	PIDK(K)	> 10
	PIDK(π)	< 5
	isMuon(h)	False
All tracks	p_T	> 500 MeV

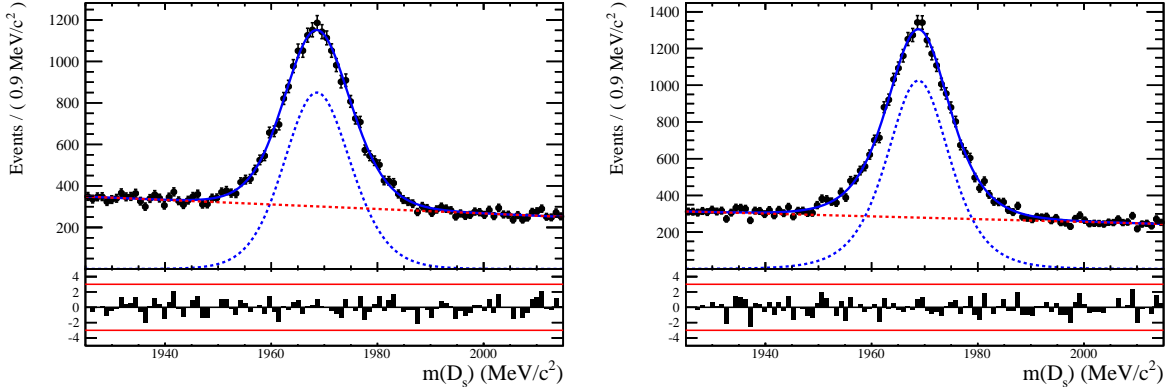


Figure 6.3: The invariant mass distribution for prompt D_s candidates for data taken from the LTUB stripping line in (left) 2016 and (right) 2017.

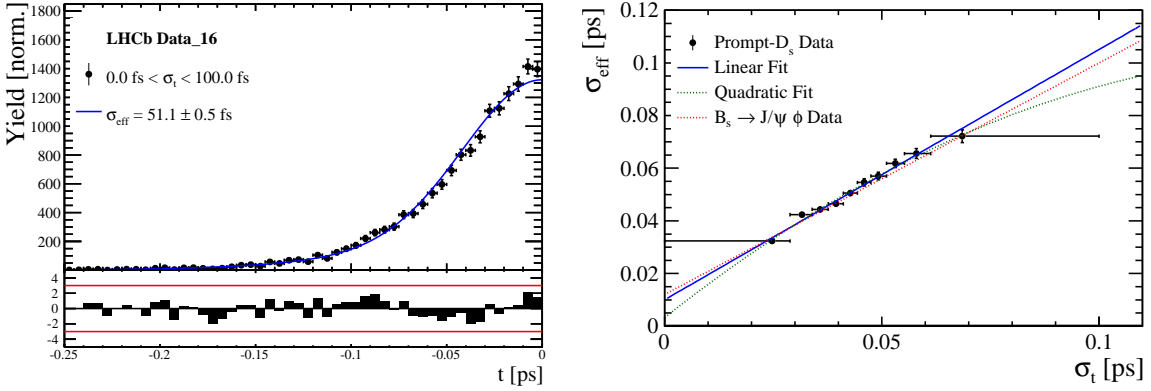


Figure 6.4: (Left) Decay-time distribution for fake B_s candidates from promptly produced D_s candidates, combined with random prompt $K\pi\pi$ bachelor tracks. (Right) The measured resolution σ_{eff} as function of the per-event decay time error estimate σ_t for fake B_s candidates (Run-II data). The fitted calibration curve is shown in blue. Data taken in 2016.

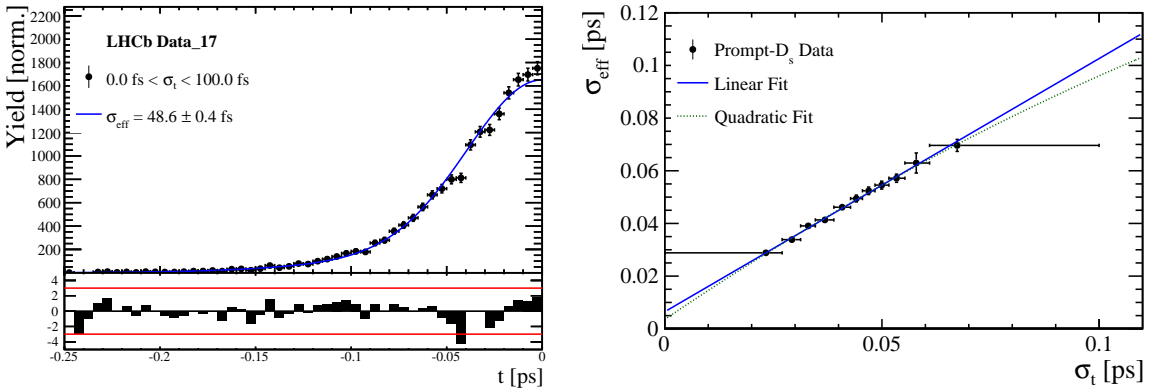


Figure 6.5: (Left) Decay-time distribution for fake B_s candidates from promptly produced D_s candidates, combined with random prompt $K\pi\pi$ bachelor tracks. (Right) The measured resolution σ_{eff} as function of the per-event decay time error estimate σ_t for fake B_s candidates (Run-II data). The fitted calibration curve is shown in blue. Data taken in 2017.

584 7 Acceptance

585 7.1 MC corrections

586 7.1.1 Truth matching of simulated candidates

587 We use the `BackgroundCategory` tool to truth match our simulated candidates. Candidates
 588 with background category (`BKGCAT`) 20 or 50 are considered to be true signal. Background
 589 category 60 is more peculiar since it contains both badly reconstructed signal candidates
 590 and ghost background. This is due to the fact that the classification algorithms identifies
 591 all tracks for which less than 70% of the reconstructed hits are matched to generated
 592 truth-level quantities as ghosts. In particular for signal decays involving many tracks (as
 593 in our case), this arbitrary cutoff is not 100% efficient. Moreover, the efficiency is expected
 594 to depend on the kinematics which would lead to a biased acceptance determination if
 595 candidates with `BKGCAT`= 60 would be removed. We therefore include `BKGCAT`= 60 and
 596 statistically subtract the ghost background by using the `sPlot` technique. The `sWeights`
 597 are calculated from a fit to the reconstructed B_s mass. The signal contribution is modeled
 598 as described in Sec. 5.1 and the background with a polynomial. The fit is performed
 599 simultaneously in two categories; the first includes events with `BKGCAT` = 20 or 50 and
 600 the second events with `BKGCAT` = 60. To account for the different mass resolution we
 601 use a different σ for each category, while the mean and the tail parameters are shared
 602 between them. The background component is only included for the second category.

603 A significant fraction of 7% of the true signal candidates are classified as ghosts, while
 604 only 20% of the events classified with `BKGCAT`= 60 are indeed genuine ghosts.

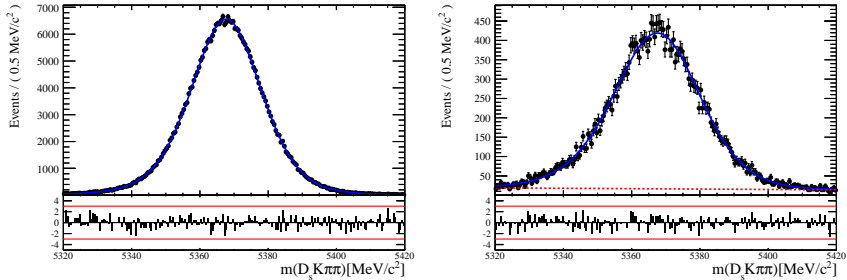


Figure 7.1: The reconstructed B_s mass distribution for simulated $B_s \rightarrow D_s K\pi\pi$ decays
 classified with `BKGCAT` = 20 or 50 (left) and `BKGCAT` = 60 (right) after the full selection.

605 7.1.2 Correction of data-simulation differences

606 For the evaluation of phase space efficiency and to a lesser extend also the decay-time
 607 efficiency we rely on simulated data as discussed in the following sections. A number
 608 of data-driven corrections are applied to the MC samples to account for known data-
 609 simulation differences. The MC sample is reweighted to match the three-dimensional
 610 p_T , η and track multiplicity distribution observed on real data. These corrections are
 611 derived from the calibration channel $B_s \rightarrow D_s \pi\pi\pi$ and applied to both the signal and
 612 calibration channel MC samples. The distributions before and after reweighting are shown
 613 in Appendix L. We use the `PIDCorr` tool to correct the simulated PID responses based on
 614 PID calibration samples [32].

615 7.2 Decay-time acceptance

616 The decay-time distribution of the B_s^0 mesons is sculpted due to the geometry of the LHCb
 617 detector and the applied selection cuts, which are described in Section 4. In particular, any
 618 requirement on the flight distance, the impact parameter or the direction angle (DIRA)
 619 of the B_s^0 mesons, as well as the direct cut on the proper-time, will lead to a decay-time
 620 dependent efficiency $\epsilon(t)$.

621 We use a combination of control channels to derive the acceptance function $\epsilon(t)$,
 622 because for $B_s^0 \rightarrow D_s K\pi\pi$ decays the decay-time acceptance is strongly correlated with
 623 the CP -observables which we aim to measure. Therefore, extracting the CP -observables
 624 and the acceptance shape at the same time is not possible. A fit to the decay-time
 625 distribution of $B_s^0 \rightarrow D_s \pi\pi\pi$ candidates is performed and the obtained acceptance shape
 626 is corrected for the small difference observed between the $B_s^0 \rightarrow D_s K\pi\pi$ and $B_s^0 \rightarrow D_s \pi\pi\pi$
 627 MC samples. In addition, we include the control channel $B^0 \rightarrow D_s K\pi\pi$ to increase
 628 the statistical precision. A simultaneous fit to the four datasets ($B_s^0 \rightarrow D_s \pi\pi\pi$ data,
 629 $B^0 \rightarrow D_s K\pi\pi$ data, $B_s^0 \rightarrow D_s K\pi\pi$ MC and $B_s^0 \rightarrow D_s \pi\pi\pi$ MC) is performed to allow for
 630 a straightforward propagation of uncertainties. In each case, a PDF of the following form

$$\mathcal{P}(t, \sigma_t) = \left[e^{-\Gamma t} \cdot \cosh\left(\frac{\Delta\Gamma t'}{2}\right) \otimes \mathcal{R}(t - t', \sigma_t) \right] \cdot \epsilon(t), \quad (7.1)$$

631 is used to describe the decay-time distribution. For real data, the values for $\Gamma_{s,d}$ and
 632 $\Delta\Gamma_{s,d}$ are fixed to the latest HFLAV results [33], while for simulated data, the generated
 633 values are used. A single Gaussian resolution function $\mathcal{R}(t - t', \sigma_t)$ is used where the
 634 decay-time error estimate is scaled with the respective calibration functions determined in
 635 Sec. 6. Each decay-time acceptance $\epsilon(t)$ is modeled using cubic splines, allowing for the
 636 analytical computation of the decay-time integrals appearing in the PDF [34]. The splines
 637 are parametrized by so-called knots (t_0, t_1, \dots, t_N) which determine their boundaries. Two
 638 knots are located by default at the lower and upper edge of the interval allowed for the
 639 decay time, the remaining ones are chosen such that there is an approximately equal
 640 amount of data in-between two consecutive knots. In the basis of cubic b-splines, $b_i(t)$,
 641 the acceptance is then constructed as:

$$\epsilon(t) = \sum_{i=0}^N v_i b_i(t) \quad (7.2)$$

642 where the spline coefficients v_i are determined from the fit. We fix coefficient v_{N-1} to unity
 643 in order to normalize the overall acceptance function. To stabilize the upper decay-time
 644 acceptance, v_N is fixed by a linear extrapolation from the two previous coefficients:

$$v_N = v_{N-1} + \frac{v_{N-2} - v_{N-1}}{t_{N-2} - t_{N-1}} \cdot (t_N - t_{N-1}). \quad (7.3)$$

645 It was found that at least $N = 6$ knots are necessary for a sufficient fit quality.

646 Three distinct splines are used in the following combinations to describe the acceptances
 647 for the four datasets:

- 648 • $B_s^0 \rightarrow D_s K\pi\pi$ MC: $\epsilon_{D_s K\pi\pi}^{MC}(t)$
- 649 • $B_s^0 \rightarrow D_s \pi\pi\pi$ MC: $\epsilon_{D_s \pi\pi\pi}^{MC}(t) = R(t) \cdot \epsilon_{D_s K\pi\pi}^{MC}(t)$
- 650 • $B_s^0 \rightarrow D_s \pi\pi\pi$ data: $\epsilon_{D_s \pi\pi\pi}^{Data}(t) = R(t) \cdot \epsilon_{D_s K\pi\pi}^{Data}(t)$
- 651 • $B^0 \rightarrow D_s K\pi\pi$ data: $\epsilon_{D_s K\pi\pi}^{Data}(t)$

652 where $\epsilon_{D_s K\pi\pi}^{MC}(t)$ represents the acceptance in $B_s^0 \rightarrow D_s K\pi\pi$ MC, $R(t)$ represents the
 653 ratio of acceptances in $B_s^0 \rightarrow D_s \pi\pi\pi$ and $B_s^0 \rightarrow D_s K\pi\pi$ MC and the final acceptance in
 654 $B_s^0 \rightarrow D_s K\pi\pi$ data is represented by $\epsilon_{D_s K\pi\pi}^{Data}(t)$.

655 The acceptances are determined separately for each data-taking period and each trigger
 656 category as discussed in more detail in Appendix F. The fit results are shown in Figs. 7.2
 657 to 7.5 and the fitted parameters are summarized in Tables 7.1 to 7.4.

Table 7.1: Time acceptance parameters for events in category [Run-I,L0-TOS].

Knot position	Coefficient	$B_s^0 \rightarrow D_s K\pi\pi$ data	$B_s^0 \rightarrow D_s K\pi\pi$ MC	Ratio
0.4	v_0	0.309 ± 0.018	0.410 ± 0.007	1.007 ± 0.029
0.5	v_1	0.694 ± 0.031	0.776 ± 0.011	0.936 ± 0.021
1.4	v_2	0.858 ± 0.043	0.896 ± 0.015	1.004 ± 0.024
2.5	v_3	1.090 ± 0.028	1.099 ± 0.009	0.992 ± 0.015
6.5	v_4	1.0 (fixed)	1.0 (fixed)	1.0 (fixed)
10.0	v_5	0.921 (interpolated)	0.913 (interpolated)	1.007 (interpolated)

Table 7.2: Time acceptance parameters for events in category [Run-I,L0-TIS].

Knot position	Coefficient	$B_s^0 \rightarrow D_s K\pi\pi$ data	$B_s^0 \rightarrow D_s K\pi\pi$ MC	Ratio
0.4	v_0	0.158 ± 0.014	0.216 ± 0.005	0.986 ± 0.040
0.5	v_1	0.422 ± 0.029	0.524 ± 0.010	0.965 ± 0.029
1.4	v_2	0.802 ± 0.047	0.860 ± 0.017	0.982 ± 0.029
2.5	v_3	1.099 ± 0.034	1.098 ± 0.011	1.002 ± 0.019
6.5	v_4	1.0 (fixed)	1.0 (fixed)	1.0 (fixed)
10.0	v_5	0.913 (interpolated)	0.914 (interpolated)	0.998 (interpolated)

Table 7.3: Time acceptance parameters for events in category [Run-II,L0-TOS].

Knot position	Coefficient	$B_s^0 \rightarrow D_s K\pi\pi$ data	$B_s^0 \rightarrow D_s K\pi\pi$ MC	Ratio
0.4	v_0	0.285 ± 0.009	0.368 ± 0.005	1.023 ± 0.020
0.5	v_1	0.663 ± 0.017	0.749 ± 0.009	0.911 ± 0.016
1.4	v_2	0.856 ± 0.025	0.893 ± 0.012	1.016 ± 0.019
2.5	v_3	1.060 ± 0.017	1.071 ± 0.008	0.996 ± 0.013
6.5	v_4	1.0 (fixed)	1.0 (fixed)	1.0 (fixed)
10.0	v_5	0.948 (interpolated)	0.938 (interpolated)	1.004 (interpolated)

Table 7.4: Time acceptance parameters for events in category [Run-II,L0-TIS].

Knot position	Coefficient	$B_s^0 \rightarrow D_s K\pi\pi$ data	$B_s^0 \rightarrow D_s K\pi\pi$ MC	Ratio
0.4	v_0	0.117 ± 0.008	0.171 ± 0.003	0.965 ± 0.034
0.5	v_1	0.422 ± 0.019	0.474 ± 0.008	0.952 ± 0.024
1.4	v_2	0.733 ± 0.027	0.777 ± 0.013	0.973 ± 0.025
2.5	v_3	1.071 ± 0.020	1.046 ± 0.010	0.989 ± 0.015
6.5	v_4	1.0 (fixed)	1.0 (fixed)	1.0 (fixed)
10.0	v_5	0.938 (interpolated)	0.959 (interpolated)	1.009 (interpolated)

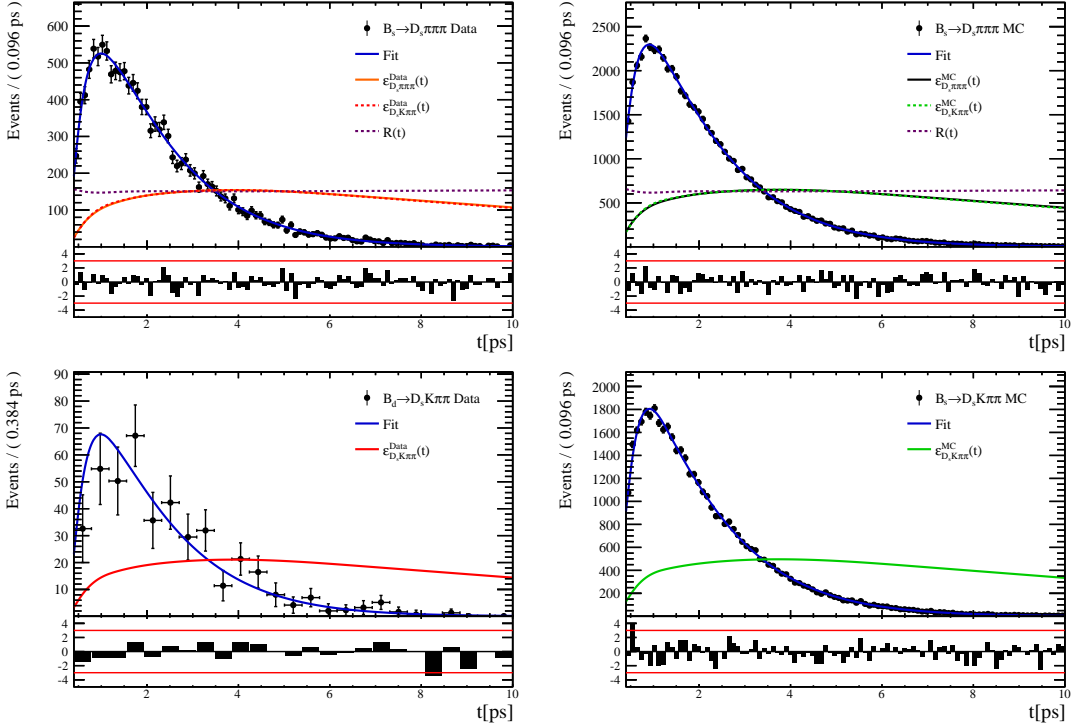


Figure 7.2: Decay-time fit projections for $B_s^0 \rightarrow D_s\pi\pi\pi$ data (top-left), $B_s^0 \rightarrow D_s\pi\pi\pi$ MC (top-right), $B^0 \rightarrow D_s K\pi\pi$ data (bottom-left) and $B_s^0 \rightarrow D_s K\pi\pi$ MC (bottom-right) in category [Run-I,L0-TOS]. The respective acceptance function is overlaid in an arbitrary scale.

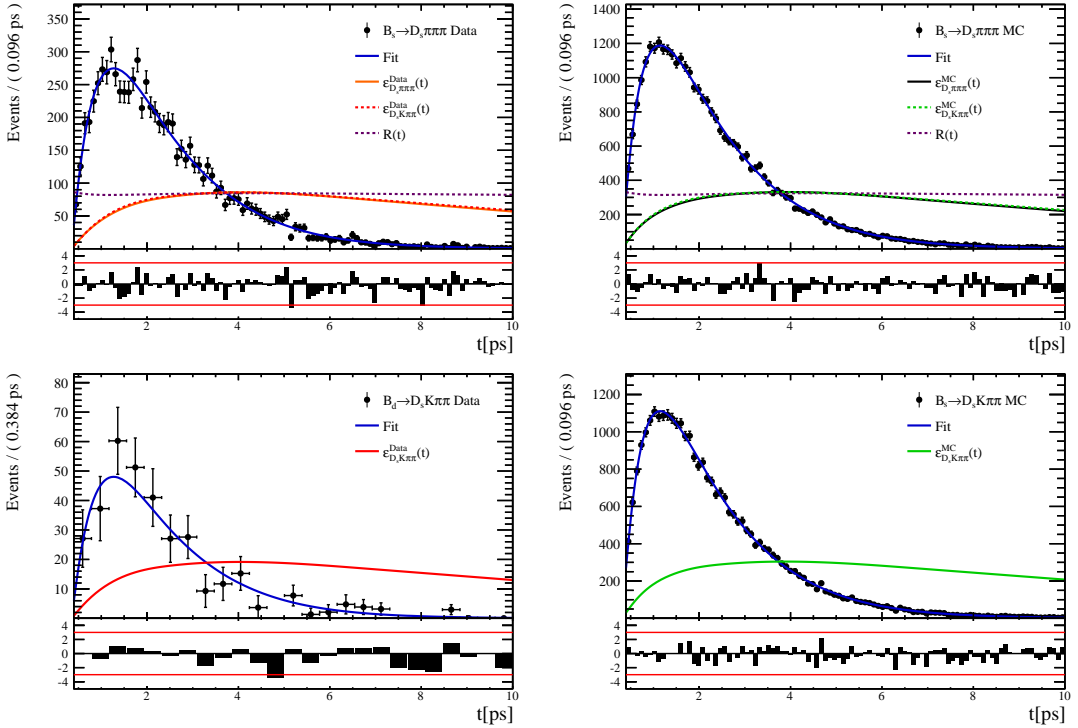


Figure 7.3: Decay-time fit projections for $B_s^0 \rightarrow D_s\pi\pi\pi$ data (top-left), $B_s^0 \rightarrow D_s\pi\pi\pi$ MC (top-right), $B^0 \rightarrow D_s K\pi\pi$ data (bottom-left) and $B_s^0 \rightarrow D_s K\pi\pi$ MC (bottom-right) in category [Run-I,L0-TIS]. The respective acceptance function is overlaid in an arbitrary scale.

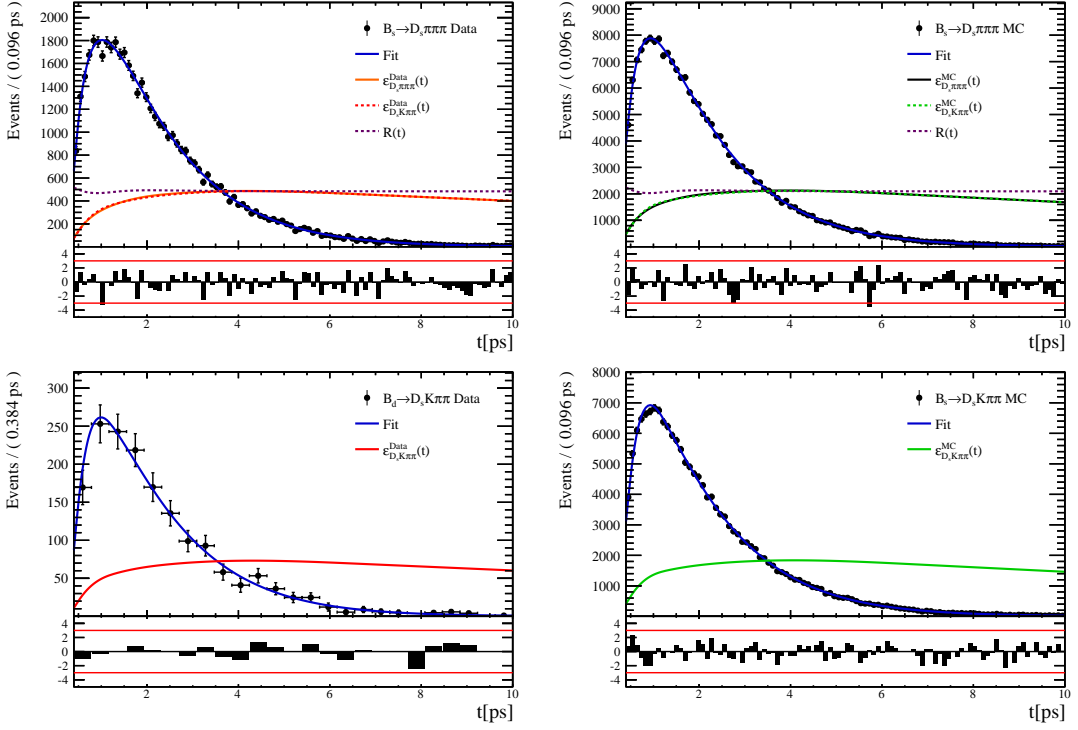


Figure 7.4: Decay-time fit projections for $B_s^0 \rightarrow D_s\pi\pi\pi$ data (top-left), $B_s^0 \rightarrow D_s\pi\pi\pi$ MC (top-right), $B^0 \rightarrow D_s K\pi\pi$ data (bottom-left) and $B_s^0 \rightarrow D_s K\pi\pi$ MC (bottom-right) in category [Run-II,L0-TOS]. The respective acceptance function is overlaid in an arbitrary scale.

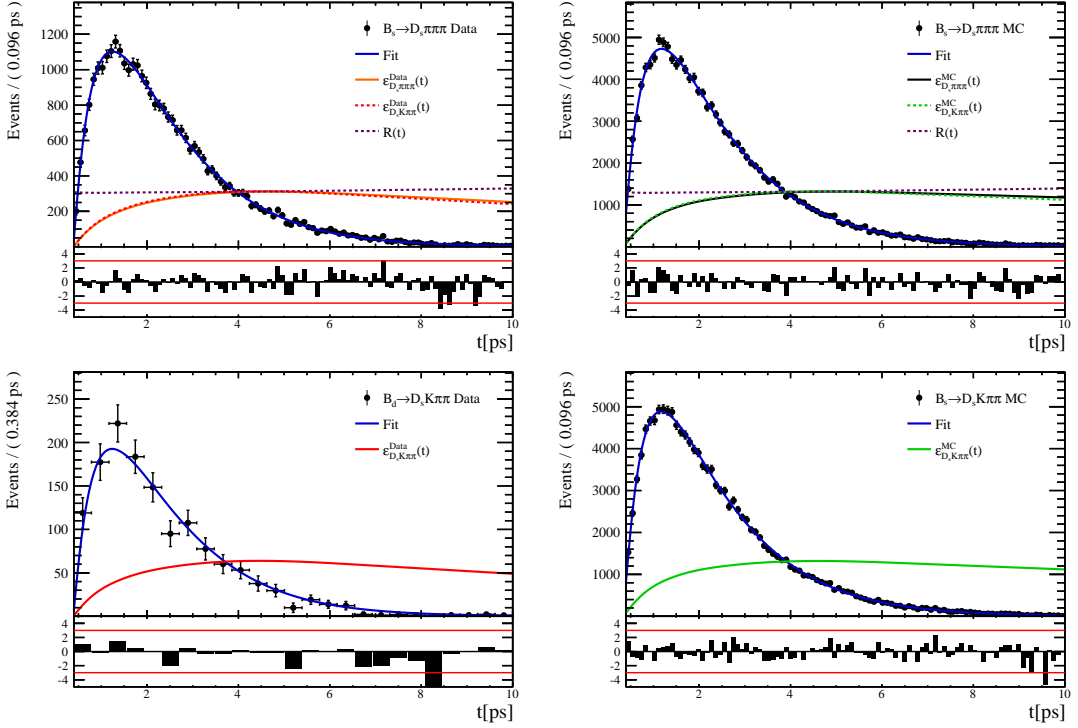


Figure 7.5: Decay-time fit projections for $B_s^0 \rightarrow D_s\pi\pi\pi$ data (top-left), $B_s^0 \rightarrow D_s\pi\pi\pi$ MC (top-right), $B^0 \rightarrow D_s K\pi\pi$ data (bottom-left) and $B_s^0 \rightarrow D_s K\pi\pi$ MC (bottom-right) in category [Run-II,L0-TIS]. The respective acceptance function is overlaid in an arbitrary scale.

658 7.3 Phase space acceptance

659 The signal PDF used for the full time-dependent amplitude fit can be written in terms of
 660 the differential decay rate from Equation 2.28 as

$$\mathcal{P}(\mathbf{x}, t, g, f) = \frac{\left(\frac{d\Gamma(\mathbf{x}, t, q, f)}{dt d\Phi_4} \right) \cdot \epsilon(\mathbf{x}) \cdot \epsilon(t)}{\int \sum_{q,f} \left(\frac{d\Gamma(\mathbf{x}, t, q, f)}{dt d\Phi_4} \right) \cdot \epsilon(\mathbf{x}) \cdot \epsilon(t) dt d\Phi_4} \quad (7.4)$$

661 where $\epsilon(\mathbf{x})$ is the phase-space efficiency. Note that the efficiency in the numerator appears
 662 as an additive constant in the log \mathcal{L} that does not depend on any fit parameters such that it
 663 can be ignored. However, the efficiency function still enters via the normalization integrals.
 664 In contrast to the time integrals which can be performed analytically as discussed in
 665 Sec. 7.2, the phase-space integrals are determined numerically. For this purpose, we use
 666 simulated events generated with **EVTGEN**, pass them through the full detector simulation
 667 and apply the same selection criteria as for data in order to perform the MC integrals. As
 668 an example, the integral of the total $b \rightarrow c$ amplitude squared can be approximated as

$$\int |\mathcal{A}_f^c(\mathbf{x})|^2 \epsilon(\mathbf{x}) d\Phi_4 \approx \frac{1}{N_{MC}} \sum_k^{N_{MC}} \frac{|\mathcal{A}_f^c(\mathbf{x}_k)|^2}{|A'(\mathbf{x}_k)|^2} \quad (7.5)$$

669 where A' labels the amplitude model used for the generation and x_k is the k -th MC
 670 event. As a result, the phase-space efficiency can be included in the fit without explicitly
 671 modeling it. The size of the fully selected MC sample ($N_{MC} = 380k$) is more than 70 times
 672 larger as the data sample which results in an integral precision smaller than 0.2%. The
 673 efficiency projections are shown in Fig. 7.6 for visualization purposes only. As discussed
 674 in Appendix G, the phase space efficiency differs significantly among L0-trigger categories
 675 while the differences are small between the data-taking periods and negligible between
 676 the D_s final states. To account for this, the MC events are scaled such that the relative
 677 proportions of the four categories [Run-I,L0-TOS], [Run-I,L0-TIS], [Run-II,L0-TOS] and
 678 [Run-II,L0-TIS] are the same as observed on the $B_s \rightarrow D_s K\pi\pi$ data sample.

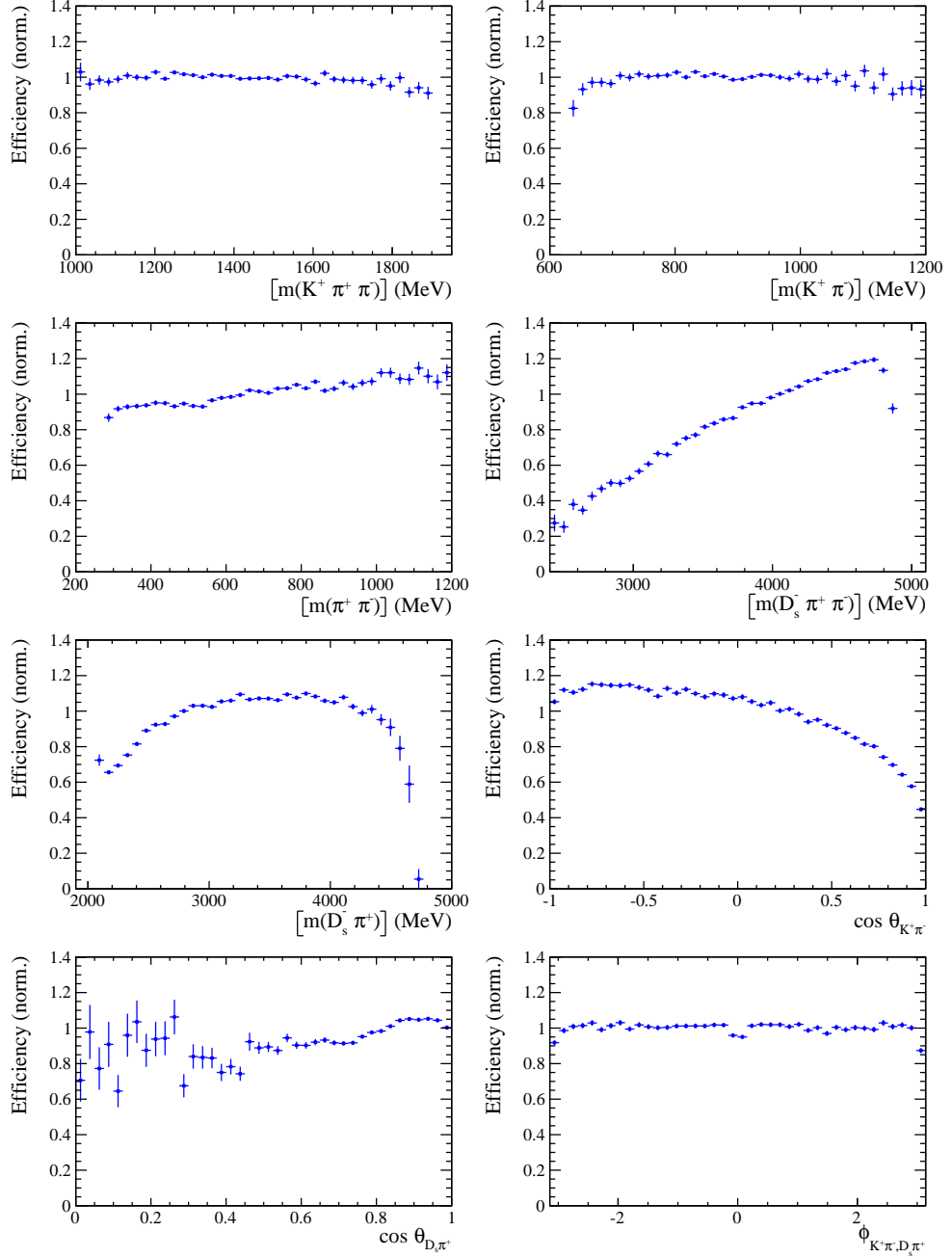


Figure 7.6: Efficiency variation as a function of the phase-space variables obtained from the ratio of selected and generated MC events.

679 8 Flavour Tagging

680 To identify the initial flavour state of the B_s^0 meson, a number of flavour tagging algorithms
 681 are used that either determine the flavour of the non-signal b-hadron produced in the
 682 event (opposite site, OS [35]) or use particles produced in the fragmentation of the signal
 683 candidate B_s^0/\bar{B}_s^0 (same side, SS [36]). For the same side, the algorithm searching for the
 684 charge of an additional kaon that accompanies the fragmentation of the signal candidate is
 685 used (SS-Kaon). For the opposite site, five different taggers are chosen: the algorithms that
 686 use the charge of an electron or a muon from semi-leptonic B decays (OS- e,μ), the tagger
 687 that uses the charge of a kaon from a $b \rightarrow c \rightarrow s$ decay chain (OS-Kaon), the algorithm
 688 which reconstructs opposite-side charm hadrons from a number of decay channels (OS-c)
 689 and the algorithm that determines the B_s^0/\bar{B}_s^0 candidate flavour from the charge of a
 690 secondary vertex, reconstructed from the OS b decay product (OS-VtxCharge).

691 Every tagging algorithm is prone to misidentify the signal candidate at a certain
 692 mistag rate ω . This might be caused by particle misidentification, flavour oscillation
 693 of the neutral opposite site B-meson or by tracks that are wrongly picked up from the
 694 underlying event. An imperfect determination of the B_s^0 production flavor dilutes the
 695 observed CP asymmetry by a factor $D_{tag} = 1 - 2\omega$. This means that the statistical
 696 precision, with which the CP asymmetry can be measured, scales as the inverse square
 697 root of the effective tagging efficiency:

$$\epsilon_{eff} = \epsilon_{tag}(1 - 2\omega)^2, \quad (8.1)$$

698 where ϵ_{tag} is the fraction of tagged candidates.

699 For each B_s^0/\bar{B}_s^0 candidate, the tagging algorithms provide, besides a flavour tag
 700 $q = 1, -1, 0$ (for an initial B_s^0 , \bar{B}_s^0 or no tag), a prediction for the mistag probability η
 701 based on the output of multivariate classifiers. These are trained on either simulated or
 702 **sWeighted** samples of flavour specific control channels ($B_s^0 \rightarrow D_s^- \pi^+$ (SS algorithm) and
 703 $B^+ \rightarrow J/\psi K^+$ (OS algorithms)) and are optimized for highest ϵ_{eff} on data. Utilizing
 704 flavour-specific final states, the estimated mistag η of each tagger has to be calibrated to
 705 match the actual mistag probability ω . For the calibration, a linear model

$$\omega(\eta) = p_0 + p_1 \cdot (\eta - \langle \eta \rangle), \quad (8.2)$$

706 is used where $\langle \eta \rangle$ is the average estimated mistag probability. A perfectly calibrated
 707 tagger would lead to $\omega(\eta) = \eta$ and one would expect $p_1 = 1$ and $p_0 = \langle \eta \rangle$. Due to the
 708 different interaction cross-sections of oppositely charged particles, the tagging calibration
 709 parameters depend on the initial state flavour of the B_s^0 . Therefore, the flavour asymmetry
 710 parameters Δp_0 , Δp_1 and $\Delta \epsilon_{tag}$ are introduced.

711 8.1 OS tagger combination

712 First, the OS electron, muon, kaon, charm and the secondary vertex charge taggers are
 713 individually calibrated and then combined into a single OS-Combo tagger using the
 714 `EspressoPerformanceMonitor` tool. We choose the flavour specific decay $B_s \rightarrow D_s \pi\pi\pi$ as
 715 calibration mode since it is very similar to the signal decay $B_s \rightarrow D_s K\pi\pi$. The calibration
 716 is performed separately for Run-I and Run-II data. The OS-c tagger is not included for
 717 Run-I data since the statistics is too low. Where available the latest Run-II tuning is used
 718 for Run-II data, otherwise the Run-I tuning of the taggers is used. The calibration sample
 719 is split in two subsamples. The single tagger calibration is performed for each and then
 720 applied to the other sample. Figures 8.1 and 8.2 show the fitted calibration functions
 721 and Tables 8.1 and 8.2 list the measured tagging performances (for both subsamples
 722 combined). The tagging calibration parameters are listed in Appendix H.

Table 8.1: The flavour tagging performances for the used OS taggers for Run-I data.

Tagger	ϵ	ω	$\epsilon \langle D^2 \rangle = \epsilon (1 - 2\omega)^2$
OS μ	$(8.713 \pm 0.206)\%$	$(28.893 \pm 0.180(\text{stat}) \pm 2.291(\text{cal}))\%$	$(1.553 \pm 0.045(\text{stat}) \pm 0.337(\text{cal}))\%$
OS e	$(3.201 \pm 0.129)\%$	$(28.792 \pm 0.363(\text{stat}) \pm 3.611(\text{cal}))\%$	$(0.576 \pm 0.030(\text{stat}) \pm 0.196(\text{cal}))\%$
OS K	$(32.230 \pm 0.342)\%$	$(38.451 \pm 0.093(\text{stat}) \pm 1.145(\text{cal}))\%$	$(1.719 \pm 0.033(\text{stat}) \pm 0.341(\text{cal}))\%$
Vertex Charge	$(21.855 \pm 0.302)\%$	$(35.712 \pm 0.091(\text{stat}) \pm 1.474(\text{cal}))\%$	$(1.785 \pm 0.033(\text{stat}) \pm 0.368(\text{cal}))\%$

Table 8.2: The flavour tagging performances for the used OS taggers for Run-II data.

Tagger	ϵ	ω	$\epsilon \langle D^2 \rangle = \epsilon (1 - 2\omega)^2$
OS μ	$(9.664 \pm 0.151)\%$	$(30.911 \pm 0.115(\text{stat}) \pm 1.369(\text{cal}))\%$	$(1.409 \pm 0.028(\text{stat}) \pm 0.202(\text{cal}))\%$
OS e	$(4.590 \pm 0.107)\%$	$(33.577 \pm 0.140(\text{stat}) \pm 2.007(\text{cal}))\%$	$(0.495 \pm 0.014(\text{stat}) \pm 0.121(\text{cal}))\%$
OS K	$(20.185 \pm 0.205)\%$	$(36.918 \pm 0.071(\text{stat}) \pm 0.969(\text{cal}))\%$	$(1.382 \pm 0.021(\text{stat}) \pm 0.205(\text{cal}))\%$
Vertex Charge	$(20.597 \pm 0.207)\%$	$(34.751 \pm 0.075(\text{stat}) \pm 0.961(\text{cal}))\%$	$(1.916 \pm 0.027(\text{stat}) \pm 0.242(\text{cal}))\%$
OS c	$(5.500 \pm 0.116)\%$	$(32.581 \pm 0.092(\text{stat}) \pm 1.848(\text{cal}))\%$	$(0.668 \pm 0.016(\text{stat}) \pm 0.142(\text{cal}))\%$

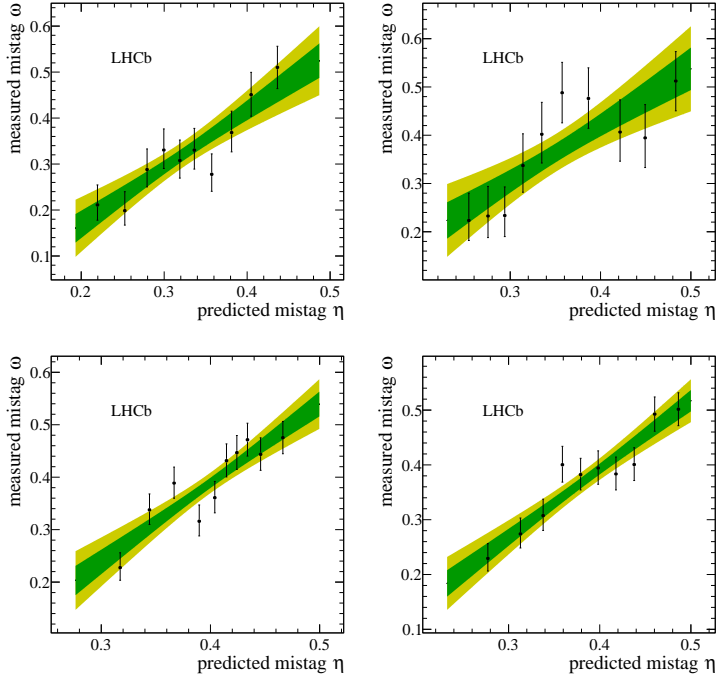


Figure 8.1: Predicted versus measured mistag probability for the (top left) OS muon, (top right) OS electron, (bottom left) OS kaon and (bottom right) OS vertex charge tagger for Run-I. A linear fit, including the 1σ and 2σ error bands is overlaid for each tagger.

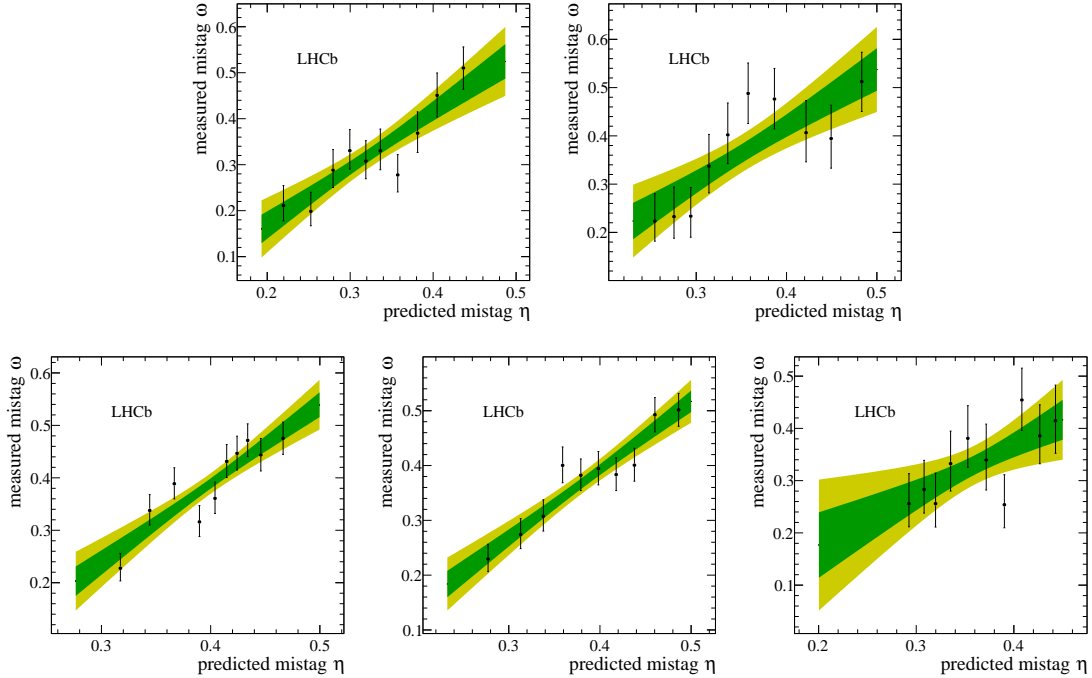


Figure 8.2: Predicted versus measured mistag probability for the (top left) OS muon, (top right) OS electron, (bottom left) OS kaon, (bottom middle) OS vertex charge and (bottom right) OS charm tagger for Run-II. A linear fit, including the 1σ and 2σ error bands is overlaid for each tagger.

723 8.2 Tagging performance

724 The OS-Combo and SS-Kaon taggers are calibrated simultaneously by fitting the $B_s \rightarrow$
 725 $D_s\pi\pi\pi$ decay-time distribution as discussed in Sec. 10. In this fit, the predicted mistag
 726 probabilities η_{OS} and η_{SS} , shown Fig. 8.3 for $B_s \rightarrow D_s\pi\pi\pi$ and $B_s \rightarrow D_sK\pi\pi$ data, are
 727 included as per-event observables, effectively giving a larger weight to the events that have
 728 a lower mistag probability. The tagger responses are combined into a single response on
 729 an event-by-event basis during the fit. Tables 8.3 and 8.4 report the tagging performances
 730 for the OS and SS combination considering three mutually exclusive categories of tagged
 731 events: OS only, SS only and both OS and SS. The tagging calibration parameters are
 732 listed in Table 10.1.

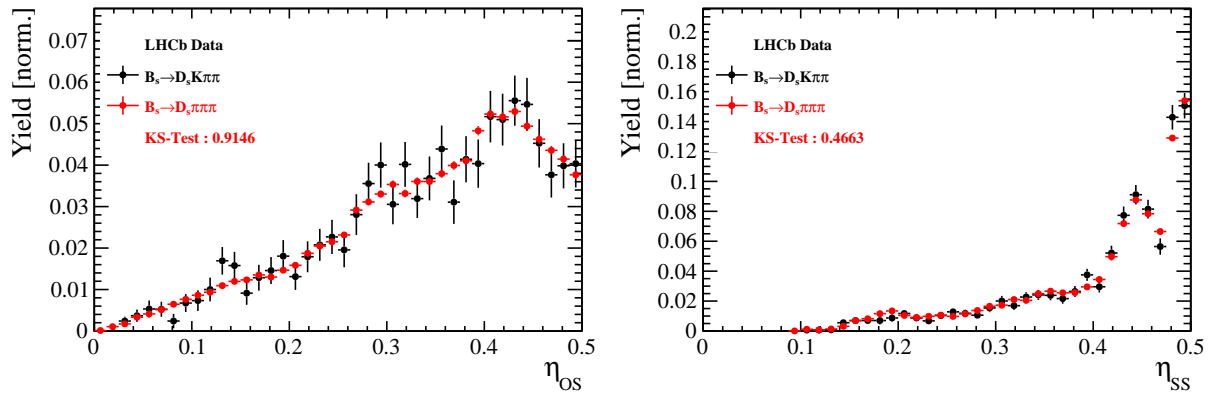


Figure 8.3: Distributions of the predicted mistag η for the OS combination (left) and the SS kaon tagger (right) for signal candidates in the $B_s^0 \rightarrow D_s K\pi\pi$ (black) and $B_s^0 \rightarrow D_s \pi\pi\pi$ (red) data samples.

Table 8.3: The flavour tagging performances for only OS tagged, only SS tagged and both OS and SS tagged events for Run-I data.

$B_s \rightarrow D_s\pi\pi\pi$	$\epsilon_{tag} [\%]$	$\langle \omega \rangle [\%]$	$\epsilon_{eff} [\%]$
Only OS	14.74 ± 0.11	39.09 ± 0.80	1.25 ± 0.16
Only SS	35.38 ± 0.18	44.26 ± 0.62	1.05 ± 0.18
Both OS-SS	33.04 ± 0.30	37.33 ± 0.73	3.41 ± 0.33
Combined	83.16 ± 0.37	40.59 ± 0.70	5.71 ± 0.40

Table 8.4: The flavour tagging performances for only OS tagged, only SS tagged and both OS and SS tagged events for Run-II data.

$B_s \rightarrow D_s\pi\pi\pi$	$\epsilon_{tag} [\%]$	$\langle \omega \rangle [\%]$	$\epsilon_{eff} [\%]$
Only OS	11.78 ± 0.05	37.01 ± 0.51	1.15 ± 0.07
Only SS	41.28 ± 0.10	42.65 ± 0.35	1.79 ± 0.12
Both OS-SS	28.62 ± 0.15	35.35 ± 0.40	3.63 ± 0.16
Combined	81.68 ± 0.19	39.28 ± 0.40	6.57 ± 0.21

9 Production and Detection Asymmetries

9.1 B_s Production Asymmetry

The production rates of b and \bar{b} hadrons in pp collisions are not expected to be identical, therefore this effect must be taken into account when computing CP asymmetries. The production asymmetry for B_s mesons is defined as:

$$A_p(B_s^0) = \frac{\sigma(\bar{B}_s^0) - \sigma(B_s^0)}{\sigma(\bar{B}_s^0) + \sigma(B_s^0)} \quad (9.1)$$

where σ are the corresponding production cross-section. This asymmetry was measured by LHCb in pp collisions at $\sqrt{s} = 7$ TeV and $\sqrt{s} = 8$ TeV by means of a time-dependent analysis of $B_s \rightarrow D_s^- \pi^+$ decays [37]. The results in bins of p_T and η of the B_s meson are shown in Table 9.1. To correct for the different kinematics of $B_s \rightarrow D_s^- \pi^+$ and $B_s^0 \rightarrow D_s K\pi\pi$ decays, the measured B_s production asymmetries $A_p(p_T, \eta)$ are folded with the sWeighted p_T, η distribution of our signal channel. The resulting effective production asymmetries are:

$$A_p(B_s^0)_{2011} = (-0.506 \pm 1.90)\% \quad (9.2)$$

$$A_p(B_s^0)_{2012} = (-0.164 \pm 1.30)\% \quad (9.3)$$

$$A_p(B_s^0)_{\text{Run-I}} = (-0.045 \pm 1.04)\%. \quad (9.4)$$

As for Run-II data no measurement is available yet, we determine the production asymmetry from $B_s \rightarrow D_s \pi\pi\pi$ data together with the tagging parameters.

Table 9.1: B_s production asymmetries in kinematic bins for 2011 and 2012 data. [37]

p_T [GeV/c]	η	$A_p(B_s^0)_{\sqrt{s}=7 \text{ TeV}}$	$A_p(B_s^0)_{\sqrt{s}=8 \text{ TeV}}$
(2.00, 7.00)	(2.10, 3.00)	$0.0166 \pm 0.0632 \pm 0.0125$	$0.0412 \pm 0.0416 \pm 0.0150$
(2.00, 7.00)	(3.00, 3.30)	$0.0311 \pm 0.0773 \pm 0.0151$	$-0.0241 \pm 0.0574 \pm 0.0079$
(2.00, 7.00)	(3.30, 4.50)	$-0.0833 \pm 0.0558 \pm 0.0132$	$0.0166 \pm 0.0391 \pm 0.0092$
(7.00, 9.50)	(2.10, 3.00)	$0.0364 \pm 0.0479 \pm 0.0068$	$0.0482 \pm 0.0320 \pm 0.0067$
(7.00, 9.50)	(3.00, 3.30)	$0.0206 \pm 0.0682 \pm 0.0127$	$0.0983 \pm 0.0470 \pm 0.0155$
(7.00, 9.50)	(3.30, 4.50)	$0.0058 \pm 0.0584 \pm 0.0089$	$-0.0430 \pm 0.0386 \pm 0.0079$
(9.50, 12.00)	(2.10, 3.00)	$-0.0039 \pm 0.0456 \pm 0.0121$	$0.0067 \pm 0.0303 \pm 0.0063$
(9.50, 12.00)	(3.00, 3.30)	$0.1095 \pm 0.0723 \pm 0.0179$	$-0.1283 \pm 0.0503 \pm 0.0171$
(9.50, 12.00)	(3.30, 4.50)	$0.1539 \pm 0.0722 \pm 0.0212$	$-0.0500 \pm 0.0460 \pm 0.0104$
(12.00, 30.00)	(2.10, 3.00)	$-0.0271 \pm 0.0336 \pm 0.0061$	$-0.0012 \pm 0.0222 \pm 0.0050$
(12.00, 30.00)	(3.00, 3.30)	$-0.0542 \pm 0.0612 \pm 0.0106$	$0.0421 \pm 0.0416 \pm 0.0162$
(12.00, 30.00)	(3.30, 4.50)	$-0.0586 \pm 0.0648 \pm 0.0150$	$0.0537 \pm 0.0447 \pm 0.0124$

747 9.2 $K^-\pi^+$ Detection Asymmetry

748 The presented measurement of the CKM-angle γ using $B_s^0 \rightarrow D_s K\pi\pi$ decays is sensitive to
 749 a possible charge asymmetry of the kaon. Kaons are known to have a nuclear cross-section
 750 which is asymmetrically dependent on the sign of their charge. It is indispensable to
 751 determine the charge asymmetry of the kaon, as fitting without taking this effect into
 752 account would introduce a 'fake' CP violation. Instead of determining the single track
 753 detection asymmetry of a kaon, it is found that the combined two track asymmetry of a
 754 kaon-pion pair is much easier to access [38]. Therefore, the two track asymmetry defined
 755 as

$$A^{det}(K^-\pi^+) = \frac{\epsilon^{det}(K^-\pi^+) - \epsilon^{det}(K^+\pi^-)}{\epsilon^{det}(K^-\pi^+) + \epsilon^{det}(K^+\pi^-)}, \quad (9.5)$$

756 is used. This asymmetry can be measured from the difference in asymmetries in the
 757 $D^+ \rightarrow K^-\pi^+\pi^+$ and $D^+ \rightarrow K_s^0\pi^+$ modes [39]:

$$\begin{aligned} A^{det}(K^-\pi^+) &= \frac{N(D^+ \rightarrow K^-\pi^+\pi^+) - N(D^- \rightarrow K^+\pi^-\pi^-)}{N(D^+ \rightarrow K^-\pi^+\pi^+) + N(D^- \rightarrow K^+\pi^-\pi^-)} \\ &\quad - \frac{N(D^+ \rightarrow K_s^0\pi^+) - N(D^- \rightarrow K_s^0\pi^-)}{N(D^+ \rightarrow K_s^0\pi^+) + N(D^- \rightarrow K_s^0\pi^-)} \\ &\quad - A(K^0), \end{aligned} \quad (9.6)$$

758 where possible CP violation in the $D^+ \rightarrow K_s^0\pi^+$ mode is predicted to be smaller than
 759 10^{-4} in the Standard Model [40]. The small asymmetry in the neutral kaon system,
 760 $A(\bar{K}^0) = -A(K^0) = (-0.054 \pm 0.014)\%$ [39], has to be taken into account as a correction.

761 We use a dedicated LHCb tool to determine $A^{det}(K^-\pi^+)$ for all data taking periods
 762 used in this analysis. A detailed description can be found in [39]. The tool provides
 763 large calibration samples of $D^\pm \rightarrow K^\pm\pi^\pm\pi^\pm$ and $D^\pm \rightarrow K_s^0\pi^\pm$ decays, which are used
 764 to determine the asymmetry following Eq. 9.6. Several weighting steps are performed
 765 to match the kinematics of the calibration samples to our signal decay sample. First,
 766 weights are assigned to the K^\pm and π^\pm of the $D^\pm \rightarrow K^\pm\pi^\pm\pi^\pm$ sample, using p, η of the
 767 K^\pm and p_T, η of the π^\pm from our $B_s^0 \rightarrow D_s K\pi\pi$ signal decay. Then, weights are assigned
 768 to the $D^\pm (p_T, \eta)$ and the $\pi^\pm (p_T)$ of the $D^\pm \rightarrow K_s^0\pi^\pm$ sample to match the corresponding,
 769 weighted distributions of the $D^\pm \rightarrow K^\pm\pi^\pm\pi^\pm$ sample. In a last step, weights are assigned
 770 to match the bachelor pions ϕ distributions between the two calibration samples. After the
 771 samples are weighted, fits are performed to the invariant $m(K^-\pi^+\pi^+)/m(K^+\pi^-\pi^-)$ and
 772 $m(K_s^0\pi^+)/m(K_s^0\pi^-)$ distributions to determine $A^{det}(K^-\pi^+)$. The PDFs used to describe
 773 the invariant mass distributions consist of gaussian functions for the signal component
 774 and exponentials describing the residual background.

775 The detection asymmetry is determined separately for every year and (since it is a
 776 charge asymmetry effect) magnet polarity. Serving as an example for Run-I and Run-
 777 II, the fits used to determine $N(D^+ \rightarrow K^-\pi^+\pi^+)/N(D^- \rightarrow K^+\pi^-\pi^-)$ and $N(D^+ \rightarrow$
 $778 K_s^0\pi^+)/N(D^- \rightarrow K_s^0\pi^-)$ for 2011, magnet up data and 2015, magnet up data are shown
 779 in Fig. 9.1 and 9.2 respectively. The obtained values of $A^{det}(K^-\pi^+) + A(K^0)$ for all
 780 years and polarities are shown in Table 9.2. Here, only the decay modes $B_s^0 \rightarrow (D_s \rightarrow$
 $781 KK\pi)K\pi\pi$ and $B_s^0 \rightarrow (D_s \rightarrow \pi\pi\pi)K\pi\pi$ are considered. For $B_s^0 \rightarrow (D_s \rightarrow K\pi\pi)K\pi\pi$,
 782 the contributions of the two oppositely charged kaons cancel each other and a detection
 783 asymmetry of zero with the same uncertainty as determined for $D_s \rightarrow KK\pi$ and $D_s \rightarrow \pi\pi\pi$

⁷⁸⁴ is assumed. In contrast, only the decay mode $D_s \rightarrow KK\pi$ is a source of detection
⁷⁸⁵ asymmetry for $B_s^0 \rightarrow D_s\pi\pi\pi$ decays resulting in an average detection asymmetry of
⁷⁸⁶ $A^{det}(K^-\pi^+) = -0.07 \pm 0.15\%$ (Run-I) and $A^{det}(K^-\pi^+) = -0.08 \pm 0.21\%$ (Run-II).

Data sample	$A^{det}(K^-\pi^+) + A(K^0)$ [%]
Run-I	
2011, mag. up	-2.01 ± 0.32
2011, mag. down	-0.16 ± 0.28
2011, average	-1.09 ± 0.21
2012, mag. up	-0.90 ± 0.20
2012, mag. down	-1.01 ± 0.22
2012, average	-0.96 ± 0.15
Run-II	
mag. up	-1.16 ± 0.34
mag. down	-0.65 ± 0.27
average	-0.91 ± 0.22

Table 9.2: Summary of the $K^-\pi^+$ detection asymmetries for $B_s^0 \rightarrow D_s K\pi\pi$ decays obtained from the fits to the Run-I and Run-II calibration samples.

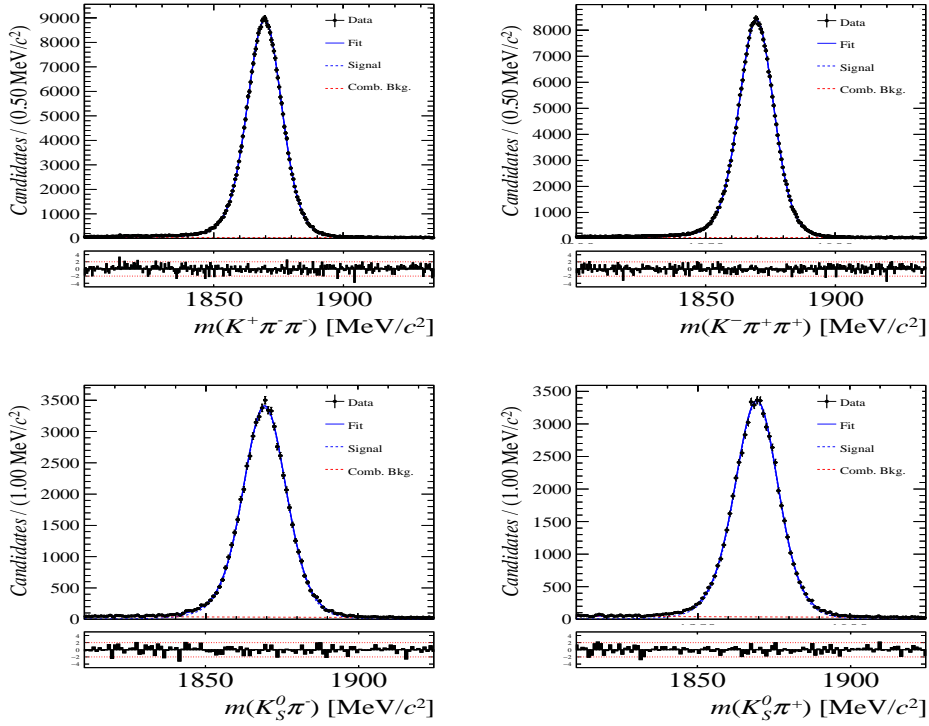


Figure 9.1: Distributions of the invariant mass of (top) $D^\pm \rightarrow K^\pm \pi^\pm \pi^\pm$ and (bottom) $D^\pm \rightarrow K_s^0 \pi^\pm$ candidates for Run-I data from the calibration samples. A fit described in the text is overlaid.

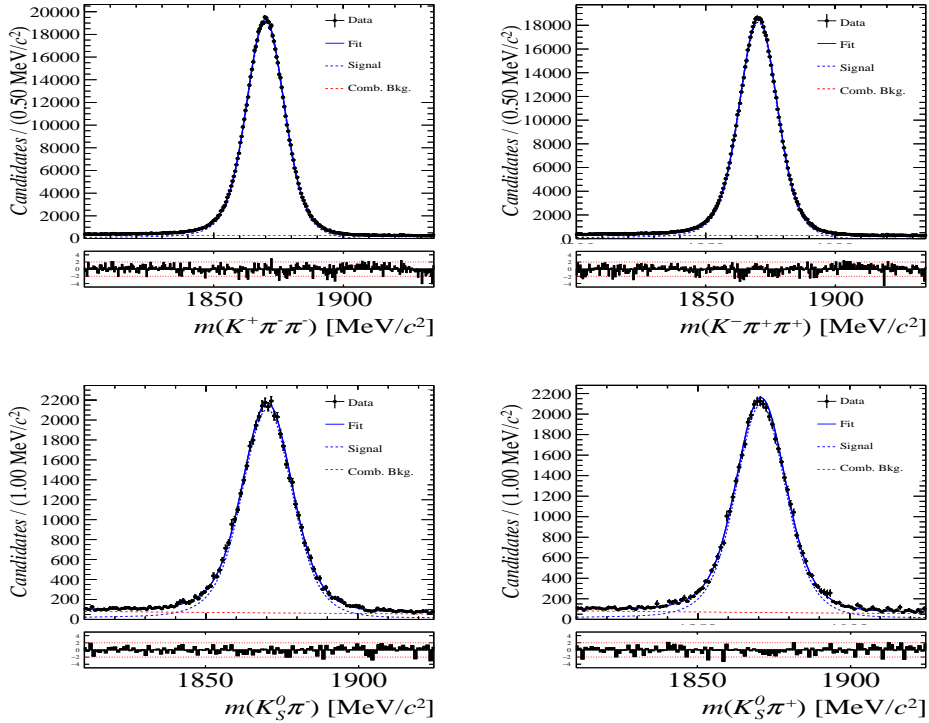


Figure 9.2: Distributions of the invariant mass of (top) $D^\pm \rightarrow K^\pm \pi^\pm \pi^\pm$ and (bottom) $D^\pm \rightarrow K_s^0 \pi^\pm$ candidates for Run-II data from the calibration samples. A fit described in the text is overlaid.

787 10 Decay-time fit

788 This section covers the (phase space integrated) decay-time fits to $B_s^0 \rightarrow D_s h\pi\pi$ data. We
 789 use the **sFit** technique [41] to statistically subtract the background, leaving only the signal
 790 PDF to describe the decay-time. The **sWeights** are calculated based on the fit to the
 791 reconstructed B_s mass distribution described in Sec. 5. The signal PDF is conditional on
 792 the tagging decisions q_i , the mistag estimates η_i ($i = \text{OS,SS}$) and the decay-time error σ_t :

$$\mathcal{P}(t|\sigma_t, q_{\text{OS}}, \eta_{\text{OS}}, q_{\text{SS}}, \eta_{\text{SS}}) \propto \left[p(t'|q_{\text{OS}}, \eta_{\text{OS}}, q_{\text{SS}}, \eta_{\text{SS}}) \otimes \mathcal{R}(t - t', \sigma_t) \right] \cdot \epsilon(t) \quad (10.1)$$

793 where $p(t|q_{\text{OS}}, \eta_{\text{OS}}, q_{\text{SS}}, \eta_{\text{SS}})$ is given by Equation 2.7 taking the tagging dilution into
 794 account. The decay-time acceptance $\epsilon(t)$ (Sec. 7) and the Gaussian time-resolution
 795 function $\mathcal{R}(t - t', \sigma_t)$ (Sec. 6) are fixed to the values obtained by the dedicated studies.
 796 We fix the values of Γ_s and $\Delta\Gamma_s$ to the latest HFLAV results [33].

797 The unbinned maximum likelihood fits are performed simultaneously in six categories:
 798 [Run-I,L0-TOS], [Run-I,L0-TIS], [Year-15/16,L0-TOS], [Year-15/16,L0-TIS], [Year-17,L0-
 799 TOS] and [Year-17,L0-TIS] to account for different time-acceptance shapes, time-resolution
 800 and tagging calibrations.

801 10.1 Fit to $B_s^0 \rightarrow D_s\pi\pi\pi$ data

802 Since the decay $B_s^0 \rightarrow D_s\pi\pi\pi$ is flavour specific, the CP coefficients can be fixed to $C = 1$
 803 and $D_f = D_{\bar{f}} = S_f = S_{\bar{f}} = 0$. The fit determines the calibration parameters for the
 804 OS-Combo and SS-Kaon taggers, the B_s^0 production asymmetry for Run-II data as well as
 805 the mixing frequency Δm_s . Table 10.1 summarizes the fitted parameters. The **sWeighted**
 806 decay-time distribution and the time-dependent asymmetry A_{mix} between mixed and
 807 unmixed B_s^0 candidates are shown in Fig. 10.1 along with the fit projections.

808 10.2 Fit to $B_s^0 \rightarrow D_sK\pi\pi$ data

809 The measured CP coefficients $C, D_f, D_{\bar{f}}, S_f$ and $S_{\bar{f}}$ extracted from a fit to the $B_s \rightarrow$
 810 $D_s K\pi\pi$ decay-time distribution are reported in Table 10.2. The fit projection is shown in
 811 Fig. 10.2. We included a multi-dimensional Gaussian-constraint for the tagging calibration
 812 parameters (including the tagging asymmetries) with the central values and covariance
 813 matrix determined in Sec. 10.1.

814 The CP coefficients are converted to the observables $r, \kappa, \delta, \gamma$ using the GammaCombo
 815 package. The corresponding confidence levels are shown in Fig 10.3.

Table 10.1: Parameters determined from a fit to the $B_s \rightarrow D_s \pi\pi\pi$ decay-time distribution. The uncertainties are statistical and systematic, respectively.

Fit Parameter	Run-I	Run-II
p_0^{OS}	$0.398 \pm 0.010 \pm 0.010$	$0.372 \pm 0.005 \pm 0.005$
p_1^{OS}	$0.895 \pm 0.085 \pm 0.090$	$0.788 \pm 0.043 \pm 0.030$
Δp_0^{OS}	$0.030 \pm 0.011 \pm 0.002$	$0.008 \pm 0.006 \pm 0.001$
Δp_1^{OS}	$0.011 \pm 0.095 \pm 0.017$	$0.067 \pm 0.052 \pm 0.002$
$\epsilon_{tag}^{OS} [\%]$	$47.775 \pm 0.365 \pm 0.067$	$40.399 \pm 0.182 \pm 0.029$
$\Delta \epsilon_{tag}^{OS} [\%]$	$0.016 \pm 1.353 \pm 0.097$	$0.316 \pm 0.618 \pm 0.046$
p_0^{SS}	$0.444 \pm 0.008 \pm 0.005$	$0.428 \pm 0.004 \pm 0.002$
p_1^{SS}	$0.949 \pm 0.111 \pm 0.067$	$0.787 \pm 0.039 \pm 0.025$
Δp_0^{SS}	$-0.019 \pm 0.009 \pm 0.001$	$-0.017 \pm 0.004 \pm 0.000$
Δp_1^{SS}	$0.064 \pm 0.124 \pm 0.017$	$0.028 \pm 0.048 \pm 0.006$
$\epsilon_{tag}^{SS} [\%]$	$68.426 \pm 0.340 \pm 0.013$	$69.903 \pm 0.170 \pm 0.007$
$\Delta \epsilon_{tag}^{SS} [\%]$	$-0.046 \pm 1.242 \pm 0.082$	$-0.319 \pm 0.575 \pm 0.062$
$A_P [\%]$	-0.045 (fixed)	$-0.183 \pm 0.642 \pm 0.048$
$\Delta m_s [\text{ps}^{-1}]$		$17.7651 \pm 0.0084 \pm 0.0058$

Table 10.2: CP coefficients determined from a fit to the $B_s \rightarrow D_s K\pi\pi$ decay-time distribution. The uncertainties are statistical and systematic, respectively.

Fit Parameter	Value
C	$0.68 \pm 0.12 \pm 0.03$
D	$-0.00 \pm 0.32 \pm 0.07$
\bar{D}	$0.39 \pm 0.30 \pm 0.07$
S	$-0.14 \pm 0.17 \pm 0.03$
\bar{S}	$-0.54 \pm 0.17 \pm 0.02$

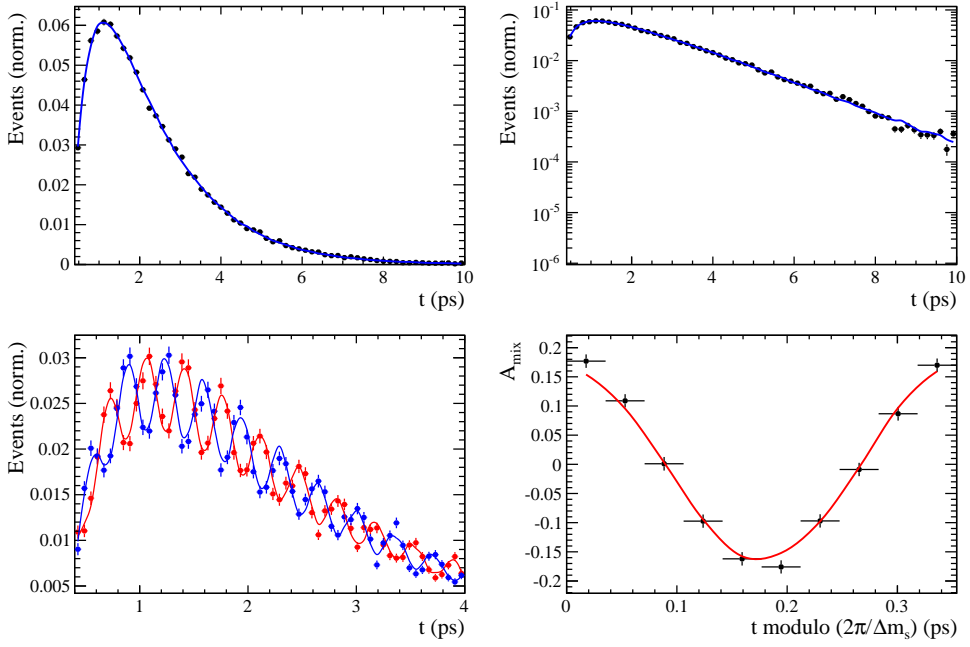


Figure 10.1: Top: Flavour averaged decay time distribution of $B_s^0 \rightarrow D_s\pi\pi\pi$ candidates. Bottom-left: Tagged decay time distribution of mixed (red) and unmixed (blue) signal candidates. Bottom-right: Time-dependent asymmetry A_{mix} between mixed and unmixed B_s^0 candidates folded into one oscillation period.

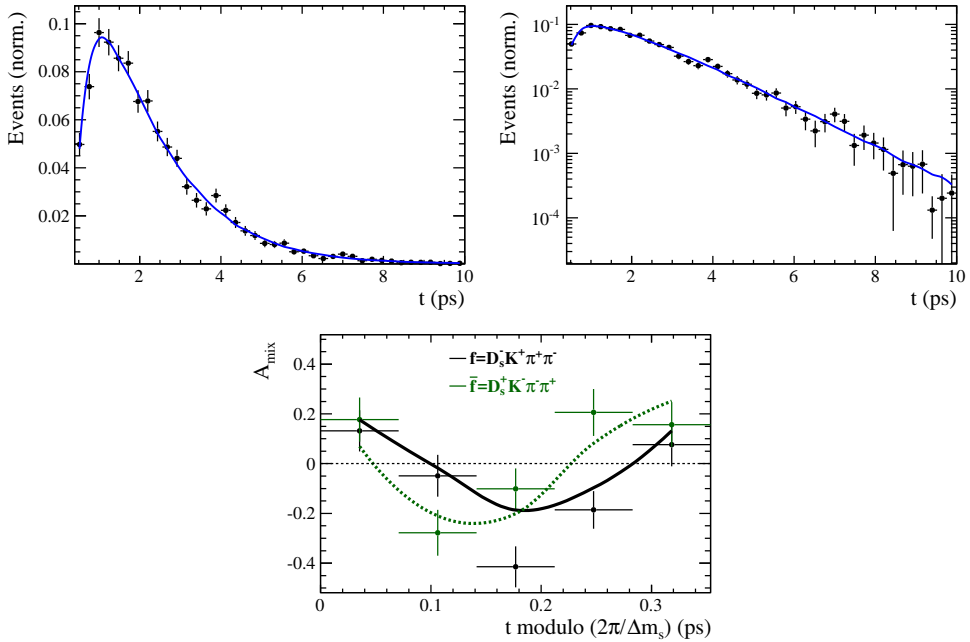


Figure 10.2: Decay-time distribution of $B_s^0 \rightarrow D_s K\pi\pi$ signal candidates with the fit projection overlaid.

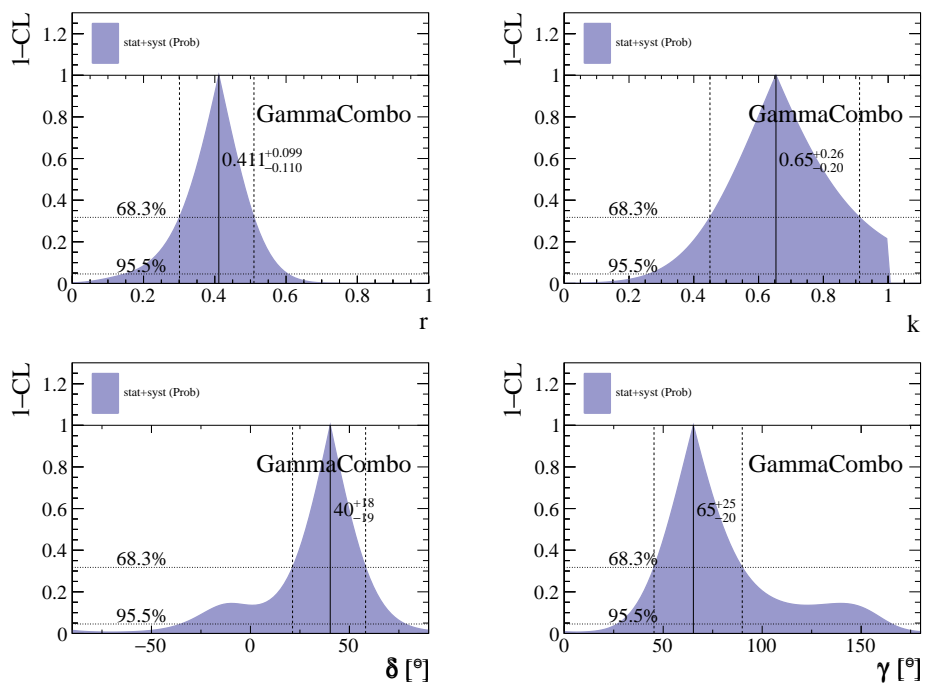


Figure 10.3: The 1-CL contours for the physical observable r , κ , δ and γ obtained with the phasespace-integrated fit.

816 11 Time-dependent amplitude fit

817 The signal PDF used for the full time-dependent fit is defined as

$$\mathcal{P}(\mathbf{x}, t | \sigma_t, q_{os}, \eta_{os}, q_{ss}, \eta_{ss}) \propto [p(\mathbf{x}, t' | q_{os}, \eta_{os}, q_{ss}, \eta_{ss}) \otimes \mathcal{R}(t - t', \sigma_t)] \cdot \epsilon(t) \quad (11.1)$$

818 where $p(\mathbf{x}, t | q_{os}, \eta_{os}, q_{ss}, \eta_{ss})$ is given the differential decay rate in Equation 2.28 taking
819 the tagging dilution into account. The phase space efficiency $\epsilon(\mathbf{x})$ is only included in the
820 normalization of $\mathcal{P}(\mathbf{x}, t | \sigma_t, q_{os}, \eta_{os}, q_{ss}, \eta_{ss})$ as discussed in Sec 7.3. The model selection
821 of the amplitude components is described in the following Section. The remaining fitting
822 strategy is exactly the same as for the decay-time fits, see Sec. 10.

823 11.1 Signal Model Construction

824 The light meson spectrum comprises multiple resonances which are expected to contribute
825 to $B_s \rightarrow D_s K\pi\pi$ decays as intermediate states. Apart from clear contributions coming
826 from resonances such as $K_1(1270)$, $K_1(1400)$, $\rho(770)$ and $K^*(892)^0$, the remaining structure
827 is impossible to infer due to the cornucopia of broad, overlapping and interfering resonances
828 within the phase space boundary. We follow the LASSO [42, 43] approach to limit the
829 model complexity in two steps.

830 First, we fit the time-integrated and flavour averaged phase-space distribution of
831 $B_s \rightarrow D_s K\pi\pi$ decays. In this case, a single total amplitude can be used:

$$\mathcal{A}_f^{eff}(\mathbf{x}) = \sum_i a_i^{eff} A_i(\mathbf{x}) \quad (11.2)$$

832 which effectively describes the incoherent superposition of the $b \rightarrow c$ and $b \rightarrow u$ amplitudes:

$$|A_f^{eff}(\mathbf{x})|^2 = |A_f^c(\mathbf{x})|^2 + |A_f^u(\mathbf{x})|^2. \quad (11.3)$$

833 This significantly simplifies the fitting procedure and allows us to include the whole pool
834 of considered intermediate state amplitudes A_i which can be found in Appendix J. The
835 LASSO penalty term added to the likelihood function

$$-2 \log \mathcal{L} \rightarrow -2 \log \mathcal{L} + \lambda \sum_i \sqrt{\int |a_i^{eff} A_i(\mathbf{x})|^2 d\Phi_4}, \quad (11.4)$$

836 shrinks the amplitude coefficients towards zero. The amount of shrinkage is controlled by
837 the parameter λ , to be tuned on data. Higher values for λ encourage sparse models, *i.e.*
838 models with only a few non-zero amplitude coefficients. The optimal value for λ is found
839 by minimizing the Bayesian information criteria [44] (BIC),

$$BIC(\lambda) = -2 \log \mathcal{L} + r \log N_{Sig}, \quad (11.5)$$

840 where N_{Sig} is the number of signal events and r is the number of amplitudes with a decay
841 fraction above a certain threshold. The fit fractions are defined as

$$F_i \equiv \frac{\int |a_i^{eff} A_i(\mathbf{x})|^2 d\Phi_4}{\int |\mathcal{A}_f^{eff}(\mathbf{x})|^2 d\Phi_4}, \quad (11.6)$$

and are a measure of the relative strength between the different transitions. Figure 11.1(left) shows the distribution of BIC values obtained by scanning over λ where we choose the decay fraction threshold to be 0.5%. At the optimal value of $\lambda = 50$, the set of amplitudes with a decay fraction above the threshold are considered further for step two of the model selection. The selected amplitudes and their fractions are summarized in Table 11.1. The fit projections are shown in Fig. 11.2. The set of selected amplitudes is stable for thresholds between 0.1% and 1%.. Other choices result in marginally different models containing one component more or less. These are included in the set of alternative models used for the systematic studies presented in Sec. 12.10.

In Stage 2, the LASSO procedure is again performed by fitting the full time-dependent amplitude PDF. The components selected by Stage 1 are included for both $b \rightarrow c$ and $b \rightarrow u$ transitions and the likelihood is extended as follows:

$$-2 \log \mathcal{L} \rightarrow -2 \log \mathcal{L} + \lambda \sum_i \sqrt{\int |a_i^c A_i(\mathbf{x})|^2 d\Phi_4} + \lambda \sum_i \sqrt{\int |a_i^u A_i(\mathbf{x})|^2 d\Phi_4} \quad (11.7)$$

Figure 11.1(right) shows a plot of the complexity factor λ , against the resulting BIC values. The final set of $b \rightarrow c$ and $b \rightarrow u$ amplitudes is selected using the optimal value of $\lambda = 6$, and is henceforth called the LASSO model. The parameters of chosen resonances are summarized in Appendix K.

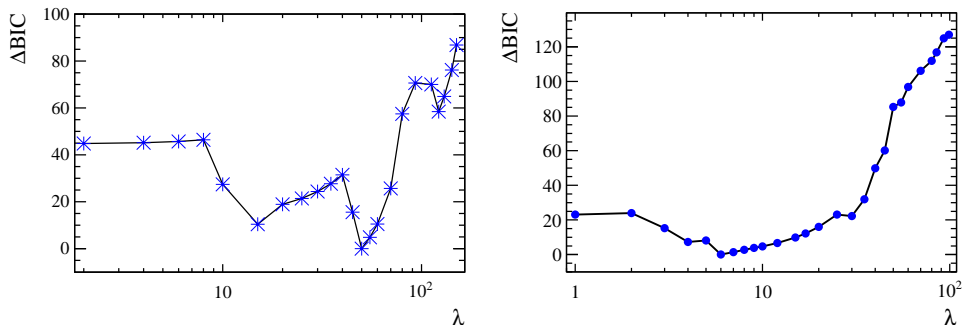


Figure 11.1: Difference in the BIC value from its minimum as function of the LASSO parameter λ for step 1 (left) and step 2 (right) of the model selection.

Table 11.1: Fit fractions of the amplitudes selected by Stage 1 of the model selection procedure.

Decay channel	Fraction [%]
$B_s \rightarrow K(1)(1270)^+ (\rightarrow K^*(892)^0 (\rightarrow K^+ \pi^-) \pi^+) D_s^-$	8.56 ± 1.43
$B_s \rightarrow K(1)(1400)^+ (\rightarrow K^*(892)^0 (\rightarrow K^+ \pi^-) \pi^+) D_s^-$	43.72 ± 2.80
$B_s \rightarrow K(1460)^+ (\rightarrow K^*(892)^0 (\rightarrow K^+ \pi^-) \pi^+) D_s^-$	3.25 ± 0.69
$B_s \rightarrow K^*(1410)^+ (\rightarrow K^*(892)^0 (\rightarrow K^+ \pi^-) \pi^+) D_s^-$	15.33 ± 1.13
$B_s \rightarrow (D_s^- \pi^+)_P K^*(892)^0 (\rightarrow K^+ \pi^-)$	4.63 ± 0.69
$B_s \rightarrow K^*(1410)^+ (\rightarrow \rho(770)^0 (\rightarrow \pi^+ \pi^-) K^+) D_s^-$	5.58 ± 0.62
$B_s \rightarrow (D_s^- K^+)_P \rho(770)^0 (\rightarrow \pi^+ \pi^-)$	1.49 ± 0.40
$B_s \rightarrow K(1)(1270)^+ (\rightarrow K(0)^*(1430)^0 (\rightarrow K^+ \pi^-) \pi^+) D_s^-$	4.72 ± 0.54
$B_s \rightarrow K(1)(1270)^+ (\rightarrow \rho(770)^0 (\rightarrow \pi^+ \pi^-) K^+) D_s^-$	14.20 ± 1.56
Sum	101.47 ± 3.86

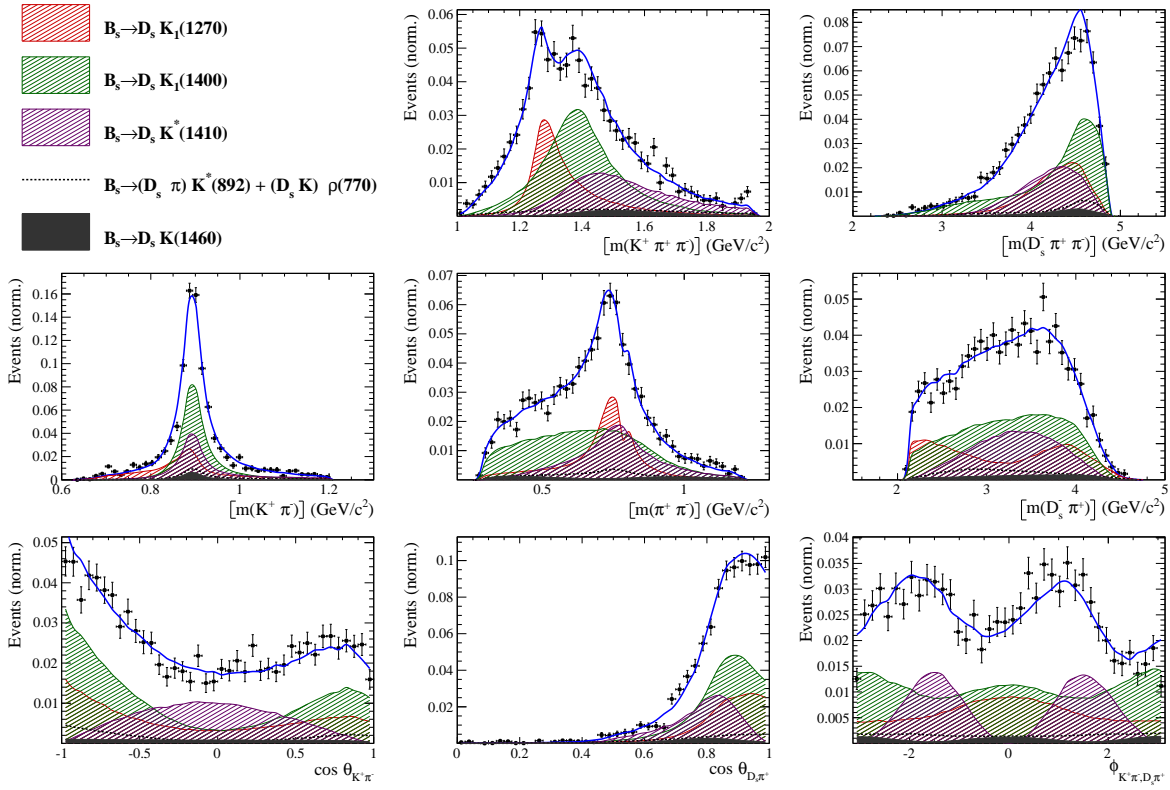


Figure 11.2: Projections of the fit result to the time-integrated and flavour averaged phase-space distribution of $B_s \rightarrow D_s K\pi\pi$ decays. The incoherent contributions of the selected decay channels are plotted as well.

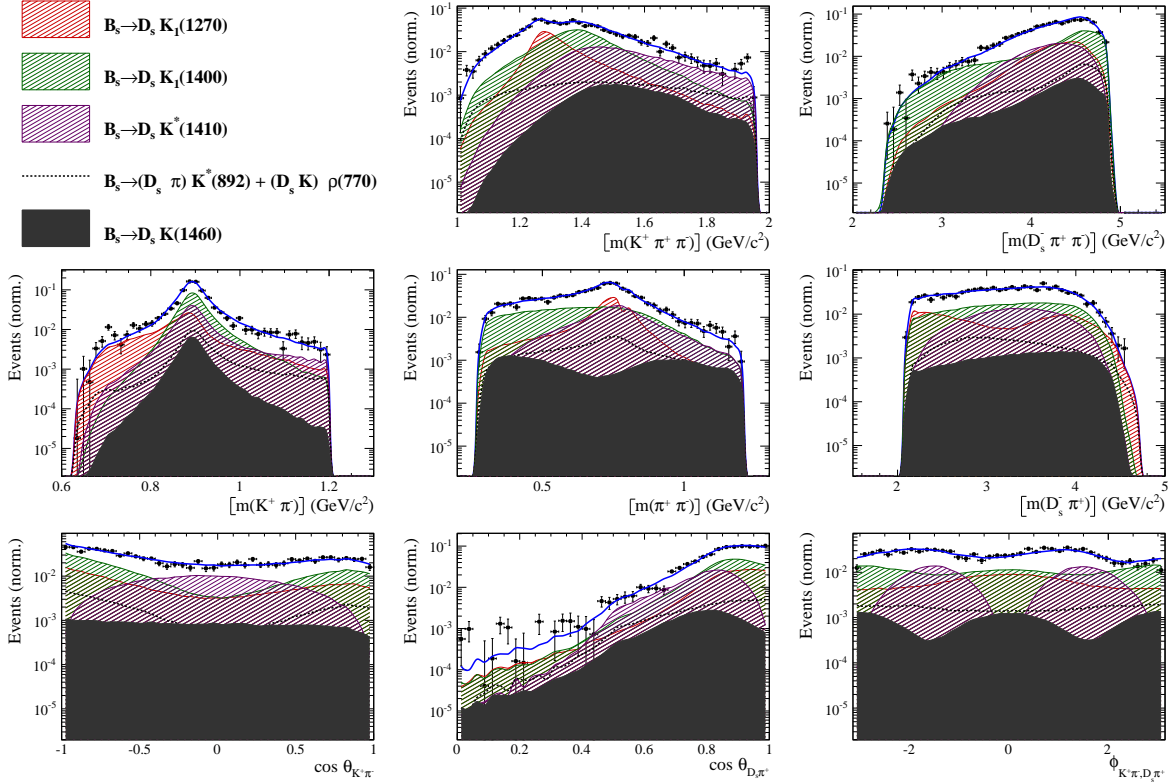


Figure 11.3: Projections of the fit result to the time-integrated and flavour averaged phase-space distribution of $B_s \rightarrow D_s K\pi\pi$ decays in logarithmic scale. The incoherent contributions of the selected decay channels are plotted as well.

858 11.2 Results

859 Table 11.2 lists the modulus and phases of the complex amplitude coefficients a_i^c and a_i^u ,
 860 obtained by fitting the LASSO model to the data. The corresponding fit fractions for the
 861 $b \rightarrow c$ and $b \rightarrow u$ amplitudes are individually normalized

$$F_i^{c,u} \equiv \frac{\int |a_i^{c,u} A_i(\mathbf{x})|^2 d\Phi_4}{\int |\mathcal{A}_f^{c,u}(\mathbf{x})|^2 d\Phi_4} \quad (11.8)$$

862 and shown in Table 11.3. The statistical significances of the three smallest contributions
 863 are: 4.5σ for $B_s \rightarrow (D_s K)_P \rho(770)$; 6.2σ for $B_s \rightarrow D_s (K(1460) \rightarrow K^*(892) \pi)$ and
 864 8.2σ for $B_s \rightarrow (D_s \pi)_P K^*(892)$. These are calculated from the likelihood difference
 865 $\sqrt{\Delta(-2LL)}$ between a fit with and without the respective component assuming Wilk's
 866 theorem. In addition to the amplitude coefficients, the amplitude ratio and the strong and
 867 weak phase differences between the $b \rightarrow c$ and $b \rightarrow u$ decays are determined. Moreover,
 868 the masses and widths of the $K_1(1400)$ and $K^*(1410)$ resonances are fitted.

869 Figure 11.4 shows the distributions of selected phase space observables, which demon-
 870 strate reasonable agreement between data and the fit model. We also project into the
 871 transversity basis to demonstrate good description of the overall angular structure (see
 872 11.4 bottom row). The acoplanarity angle χ , is the angle between the two decay planes
 873 formed by the $K^+ \pi^-$ system and the $D_s^- \pi^+$ system in the B_s rest frame; boosting into the
 874 rest frames of the two-body systems defining these decay planes, the two helicity variables
 875 are defined as the cosine of the angle, θ , of the K^+ or D_S^- momentum with the B_s flight
 876 direction.

877 In order to quantify the quality of the fit in the five-dimensional phase space, a χ^2
 878 value is determined by binning the data;

$$\chi^2 = \sum_{b=1}^{N_{\text{bins}}} \frac{(N_b - N_b^{\text{exp}})^2}{N_b^{\text{exp}}}, \quad (11.9)$$

879 where N_b is the number of data events in a given bin, N_b^{exp} is the event count predicted
 880 by the fitted PDF and N_{bins} is the number of bins. An adaptive binning is used to ensure
 881 sufficient statistics in each bin for a robust χ^2 calculation [45]. At least 25 events per
 882 bin are required. The number of degrees of freedom ν , in an unbinned fit is bounded by
 883 $N_{\text{bins}} - 1$ and $(N_{\text{bins}} - 1) - N_{\text{par}}$, where N_{par} is the number of free fit parameters. We use
 884 the χ^2 value divided by $\nu = (N_{\text{bins}} - 1) - N_{\text{par}}$ as a conservative estimate. For the LASSO
 885 model, this amounts to $\chi^2/\nu = 1.40$ with $\nu = 137$, indicating a decent fit quality.

Table 11.2: Modulus and phases of the amplitudes contributing to $b \rightarrow c$ and $b \rightarrow u$ decays. In case of multiple decay modes of three-body resonances, the amplitude coefficients are defined relative to the one listed first. Additional fit parameters are listed below. The first quoted uncertainty is statistical, while the second arises from systematic sources. The third uncertainty arises from the alternative models considered.

Decay Channel	$A^c(\mathbf{x})$		$A^u(\mathbf{x})$	
	$ a_i^c $	$\arg(a_i^c)[^\circ]$	$ a_i^u $	$\arg(a_i^u)[^\circ]$
$B_s \rightarrow D_s (K_1(1270) \rightarrow K \rho(770))$	1.0	0.0	1.0	0.0
$K_1(1270) \rightarrow K^*(892) \pi$	$0.72 \pm 0.11 \pm 0.08$	$50.2 \pm 7.8 \pm 5.3$		
$K_1(1270) \rightarrow K_0^*(1430) \pi$	$0.52 \pm 0.05 \pm 0.05$	$128.9 \pm 5.8 \pm 17.8$		
$B_s \rightarrow D_s (K_1(1400) \rightarrow K^*(892) \pi)$	$1.98 \pm 0.26 \pm 0.18$	$10.5 \pm 7.6 \pm 5.6$	$0.75 \pm 0.21 \pm 0.16$	$-64.3 \pm 16.0 \pm 11.2$
$B_s \rightarrow D_s (K^*(1410) \rightarrow K^*(892) \pi)$	$1.14 \pm 0.09 \pm 0.07$	$55.0 \pm 6.3 \pm 5.2$		
$K^*(1410) \rightarrow K \rho(770)$	$0.63 \pm 0.05 \pm 0.03$	$-164.1 \pm 5.1 \pm 2.7$		
$B_s \rightarrow D_s (K(1460) \rightarrow K^*(892) \pi)$			$0.87 \pm 0.13 \pm 0.08$	$-96.1 \pm 13.1 \pm 9.7$
$B_s \rightarrow (D_s \pi)_P K^*(892)$	$0.72 \pm 0.13 \pm 0.12$	$-17.2 \pm 13.8 \pm 11.3$	$1.13 \pm 0.20 \pm 0.14$	$-16.7 \pm 17.7 \pm 15.3$
$B_s \rightarrow (D_s K)_P \rho(770)$			$0.53 \pm 0.08 \pm 0.07$	$33.7 \pm 11.4 \pm 10.4$
Fit parameter	Value			
$m_{K_1(1400)}$ [MeV]	$1397 \pm 8 \pm 5 \pm 7$			
$\Gamma_{K_1(1400)}$ [MeV]	$205 \pm 17 \pm 9 \pm 8$			
$m_{K^*(1410)}$ [MeV]	$1432 \pm 13 \pm 16 \pm 8$			
$\Gamma_{K^*(1410)}$ [MeV]	$345 \pm 27 \pm 36 \pm 17$			
r	$0.50 \pm 0.04 \pm 0.03 \pm 0.02$			
$\delta [^\circ]$	$46 \pm 15 \pm 6 \pm 8$			
$\gamma - 2\beta_s [^\circ]$	$61 \pm 15 \pm 6 \pm 6$			

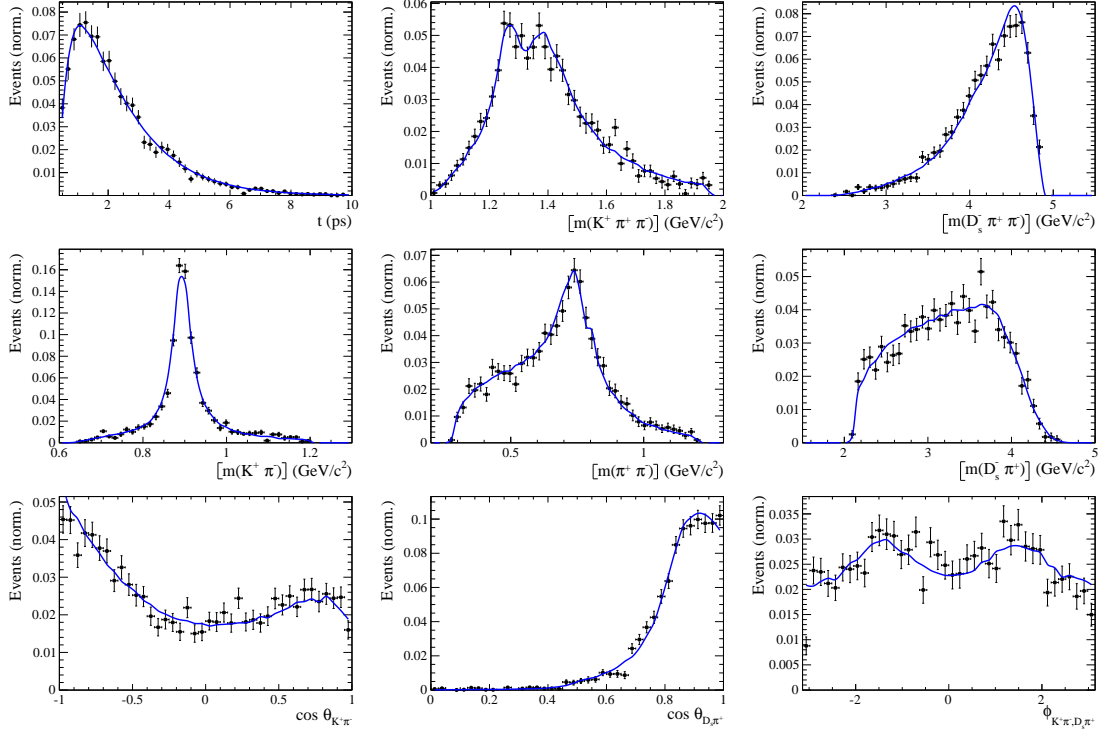


Figure 11.4: Projections of the full time-dependent amplitude fit.

Table 11.3: Fit fractions of the amplitudes contributing to $b \rightarrow c$ and $b \rightarrow u$ decays.

Decay Channel	$F^c[\%]$	$F^u[\%]$
$B_s \rightarrow D_s (K_1(1270) \rightarrow K \rho(770))$	$12.3 \pm 1.4 \pm 1.3 \pm 1.9$	$29.1 \pm 6.1 \pm 6.4 \pm 6.2$
$B_s \rightarrow D_s (K_1(1270) \rightarrow K^*(892) \pi)$	$6.3 \pm 1.6 \pm 1.5 \pm 0.8$	$14.9 \pm 4.5 \pm 4.2 \pm 4.3$
$B_s \rightarrow D_s (K_1(1270) \rightarrow K_0^*(1430) \pi)$	$3.4 \pm 0.5 \pm 0.9 \pm 0.5$	$8.0 \pm 2.1 \pm 2.5 \pm 1.7$
$B_s \rightarrow D_s (K_1(1400) \rightarrow K^*(892) \pi)$	$48.3 \pm 4.5 \pm 6.8 \pm 4.5$	$17.2 \pm 8.6 \pm 7.6 \pm 6.4$
$B_s \rightarrow D_s (K^*(1410) \rightarrow K^*(892) \pi)$	$15.5 \pm 1.0 \pm 1.0 \pm 1.1$	
$B_s \rightarrow D_s (K^*(1410) \rightarrow K \rho(770))$	$6.7 \pm 0.6 \pm 0.7 \pm 0.5$	
$B_s \rightarrow D_s (K(1460) \rightarrow K^*(892) \pi)$		$21.0 \pm 4.6 \pm 4.0 \pm 5.1$
$B_s \rightarrow (D_s \pi)_P K^*(892)$	$6.8 \pm 1.5 \pm 2.4 \pm 2.3$	$36.0 \pm 8.0 \pm 10.1 \pm 13.2$
$B_s \rightarrow (D_s K)_P \rho(770)$		$9.7 \pm 4.0 \pm 4.1 \pm 3.5$
Sum	$99.3 \pm 4.7 \pm 6.8 \pm 4.0$	$135.9 \pm 12.9 \pm 12.5 \pm 11.7$

886 12 Systematic uncertainties

887 The systematic uncertainties on the measured observables are summarized in Table 12.3 for
888 the decay-time fit to $B_s \rightarrow D_s \pi\pi\pi$, in Table 12.4 for the decay-time fit to $B_s \rightarrow D_s K\pi\pi$
889 and in Table 12.5 for the full time-dependent amplitude fit to $B_s \rightarrow D_s K\pi\pi$ decays. A
890 description of each systematic effect is given in the following subsections starting with the
891 ones common to all fits. Afterwards, systematic effect specific to the amplitude description
892 are discussed. Systematic uncertainties estimated from pseudo-experiments (toys) are
893 calculated relative to the statistical error.

894 12.1 Fit bias

895 Pseudo-experiments are performed, where a signal toy sample of the same size as the
896 number of observed signal data events is generated according to the nominal fit model and
897 subsequently fitted with the same model. The means of the pull distributions are taken
898 as systematic uncertainties of the fit parameters. The width of the pull distributions are
899 compatible with 1.

900 12.2 Background subtraction

901 The statistical subtraction of the residual background [41], left after the full selection,
902 relies on the correct description of the invariant B_s^0 mass distribution. Since the choice of
903 signal and background models is not unique, alternative parameterizations are tested:

- 904 • The Johnson's SU function which is used as nominal signal model is replaced by the
905 sum of two Crystal Ball functions [46].
- 906 • For the combinatorial background, the nominal second order polynomial is replaced
907 by an exponential function.
- 908 • For the description of the partially reconstructed background, a combination of the
909 RooHILLdini and RooHORNsdini model [47] is used instead of the nominal model of
910 three bifurcated gaussians.
- 911 • For the shape of the mis-ID background, the nominal approach is to use a simulated
912 sample of $B_s^0 \rightarrow D_s^- \pi^+ \pi^- \pi^+$ or $B_s^0 \rightarrow D_s^{*-} \pi^+ \pi^- \pi^+$ decays and flip the mass
913 hypothesis of the π^+ with the higher misidentification probability (see Sec. 5).
914 Two alternative approaches are considered: we flip the mass hypothesis of the π^+
915 candidate with the lower probability of being misidentified; we randomly flip the
916 mass hypothesis of a π^+ candidate. To account for the systematic of the $\pi \rightarrow K$
917 fake rate, we vary the default PIDK cut ($\text{PIDK} > 10$) by ± 2 when calculating the
918 misID weights from `PIDCalib`.

919 In total 10 (7) different combinations of the modifications discussed above are tested
920 for the fit to the $D_s K\pi\pi$ ($D_s \pi\pi\pi$) mass distribution. For each case, new signal `sWeights`
921 are calculated and the `sFits` to data are repeated. The sample variance of the obtained
922 differences to the nominal fit value are used as systematic uncertainty due to the background
923 subtraction.

924 12.3 Decay-time acceptance

925 The systematic uncertainty related to the decay-time efficiency as well as Γ_s and $\Delta\Gamma_s$ are
 926 studied simultaneously. We generate toys in the nominal configuration and fit back in
 927 both this nominal configuration and a configuration in which we have randomized the
 928 acceptance parameters together with Γ_s and $\Delta\Gamma_s$ within their uncertainties. For each toy,
 929 a pull is calculated by dividing the difference between the fitted values of the nominal
 930 and shifted configurations by the uncertainty in the nominal toy. We add the bias in the
 931 mean of this pull to its width, in quadrature, in order to arrive at the final systematic
 932 uncertainty.

933 To improve the coverage of the multi-dimensional parameter space, a Cholesky decom-
 934 position [48] is used to generate a set of uncorrelated vectors from the covariance matrix
 935 $\text{cov}(\lambda_i, \lambda_j)$, where the vector λ includes the parameters Γ_s , $\Delta\Gamma_s$ and the $N = 4$ spline
 936 coefficients for each category of the simultaneous fit. The correlations between Γ_s ($\Delta\Gamma_s$)
 937 and the spline coefficients are measured by rerunning the acceptance fits described in
 938 Sec. 7.2 with the values of Γ_s ($\Delta\Gamma_s$) varied by $\pm 1\sigma$ and measuring the shift in the spline
 939 coefficients as a fraction of their uncertainty. For the correlation between Γ_s and $\Delta\Gamma_s$ we
 940 use the HFLAV value [33].

941 12.4 Decay-time resolution and tagging

942 To study systematic effects originating from the scaling of the decay-time error estimate,
 943 two different approaches which either slightly overestimate or underestimate the resolution
 944 are used:

- 945 • A double Gaussian is fit to the decay-time distributions of fake B_s^0 candidates, but
 946 only the width of the core Gaussian is considered to represent the time resolution in
 947 the respective bin. Therefore the resolution is slightly underestimated in this case.
- 948 • A single Gaussian is fit to the decay-time distributions of fake B_s^0 candidates in a
 949 wide range of $[-3\sigma_t : 1.5\sigma_t]$. Due to the tails of the distribution, which broaden the
 950 width of the Gaussian function, this method slightly overestimates the decay-time
 951 resolution.

952 For each case, a new scaling function is derived:

$$\sigma_{\text{eff},\text{Data},16}^{\text{core-Gauss}}(\sigma_t) = (6.8 \pm 1.9) \text{ fs} + (0.797 \pm 0.050) \sigma_t \quad (12.1)$$

$$\sigma_{\text{effData},16}^{\text{single-Gauss}}(\sigma_t) = (10.1 \pm 1.5) \text{ fs} + (0.950 \pm 0.039) \sigma_t \quad (12.2)$$

$$\sigma_{\text{eff},\text{Data},17}^{\text{core-Gauss}}(\sigma_t) = (0.1 \pm 1.5) \text{ fs} + (0.957 \pm 0.037) \sigma_t \quad (12.3)$$

$$\sigma_{\text{effData},17}^{\text{single-Gauss}}(\sigma_t) = (5.6 \pm 1.2) \text{ fs} + (1.012 \pm 0.031) \sigma_t \quad (12.4)$$

956 They are compared to the nominal result in Fig. 12.1.

957 Due to the high correlation between the decay-time resolution and the tagging calibra-
 958 tion, their systematic uncertainty has to be studied simultaneously. First, the decay-time
 959 fits to $B_s \rightarrow D_s \pi\pi\pi$ data are repeated using the alternative decay-time error scaling
 960 functions. New tagging calibration parameters are obtained which are then used (together
 961 with the respective decay-time error scaling function) in the fits to $B_s \rightarrow D_s K\pi\pi$ data to

962 define the Gaussian-constraints as discussed in Sec. 10. For the width of the Gaussians
 963 only the statistical error of the tagging calibration parameters are used since systematic
 964 uncertainties (except the systematic arising from the decay-time resolution which is already
 965 included by the procedure described above) are found to be negligible, see Table 12.3.
 966 Finally, we take the biggest change in fit central value as the systematic for each parameter
 967 of the $B_s \rightarrow D_s K\pi\pi$ fits.

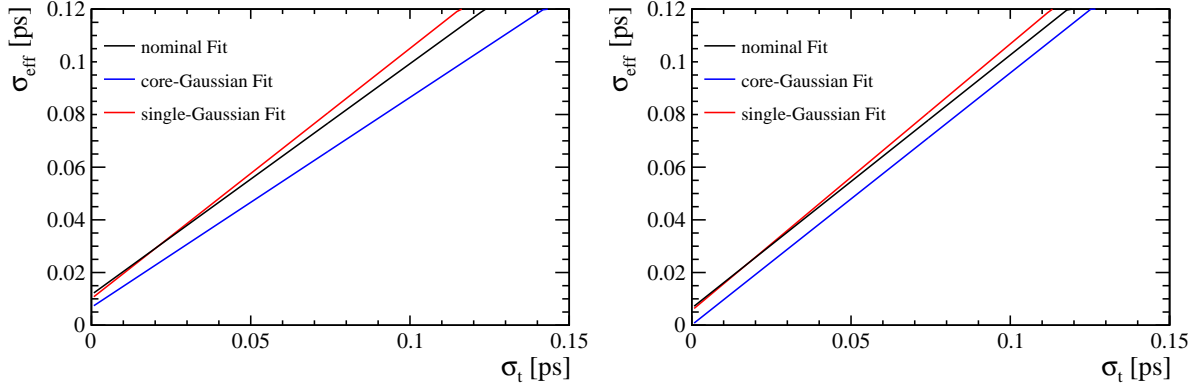


Figure 12.1: The measured resolution scaling function of the per-event decay time error estimate σ_t for fake B_s candidates (Run-II data) for (black line) the nominal scaling, (blue line) only using the narrow gaussian width of the double gaussian fit model or (red line) when determining the resolution using a single gaussian model. Data taken in (left) 2016 and (right) 2017.

968 12.5 Production, detection asymmetries and mixing frequency

969 The systematic from the production, detection asymmetries and Δm_s (in case of $B_s \rightarrow$
 970 $D_s K\pi\pi$ decays) which are fixed in the fit are evaluated by means of a toy study similar
 971 to the procedure performed for the time-acceptance. The parameters are assumed to be
 972 uncorrelated.

973 12.6 Multiple candidates

974 The fraction of events with multiple candidates has been found to be very small, it is
 975 1.6% for $D_s K\pi\pi$ and 1.5% for $D_s \pi\pi\pi$. Thus the nominal result is obtained keeping all
 976 candidates, while a systematic uncertainty is assigned by repeating the fit randomly
 977 keeping only one candidate when multiple ones are founds. No shifts in the fit central
 978 values are observed.

979 12.7 Length and momentum scales

980 The uncertainty on the LHCb length scale is estimated to be at most 0.020% [49, 50],
 981 which translates directly in an uncertainty on Δm_s of 0.020% with other parameters
 982 being unaffected. The momentum scale uncertainty is at most 0.022%. In the fit to
 983 $B_s \rightarrow D_s K\pi\pi$ data, the scale uncertainties are then implicitly included in the systematic
 984 due to Δm_s which we vary within its uncertainties, see above.

985 **12.8 Phase space acceptance**

986 For the phase space acceptance we rely on simulated data. The integration error due to
987 the limited size of the MC sample used to normalize the signal PDF is below 0.2% and
988 thus negligible small.

989 To asses the uncertainty due to possible data-simulation differences, we determine
990 alternative phase space efficiencies by varying the selection requirements on quantities
991 that are expected not to be well described by the simulation. In particular, we consider
992 the following variations:

- 993 • No BDT cut is applied
- 994 • A tighter BDT requirement is used ($\text{BDTG} > 0.6$)
- 995 • No reweighting is applied
- 996 • Instead of the PID responses obtained from the `PIDCorr` tool, we use the `PIDGen`
997 tool to resample the PID variables [32]
- 998 • The raw MC PID variables are used
- 999 • Candidates with `BKGCAT`= 60 are removed
- 1000 • A tight cut on the B_s transverse momentum is applied ($p_T > 10 \text{ GeV}$)
- 1001 • We require `L0Hadron-TOS` instead of (`L0Hadron-TOS` || `L0Global-TIS`)
- 1002 • We require `L0Global-TIS` instead of (`L0Hadron-TOS` || `L0Global-TIS`)

1003 We assign the sample variance of the fitted values using the alternative phase space
1004 acceptances as systematic.

1005 **12.9 Resonance description**

1006 The following alternative line shape parameterizations are considered as part of the
1007 systematic studies:

- 1008 • The Lass description for the $K\pi$ S -wave is replaced by a more general model
1009 (Glass [51, 52])
- 1010 • The Gounaris-Sakurai description for the $\rho(770)$ is replaced by a relativistic Breit-
1011 Wigner propagator (Equation 2.16)
- 1012 • The ω contribution to the decay channel $K_1(1270) \rightarrow K \rho(770)/\omega$ is set to zero
- 1013 • For the decay channel $K^*(1410) \rightarrow K \rho(770)$, we include $\rho(770) - \omega$ mixing with a
1014 relative magnitude and phase determined from data
- 1015 • Instead of taking the energy-dependent widths of the three-body resonances from
1016 Refs. [12, 23], we derive them from Equation 2.17 taking only the dominant $K\pi\pi$
1017 decay mode into account

1018 The data fits are repeated for each alternative model and the RMS of the central values
1019 are taken as systematic uncertainties.

1020 The uncertainties due to fixed masses and widths of resonances are evaluated from
1021 toys where we vary them one-by-one within their quoted errors. In our nominal fit, the
1022 Blatt-Weisskopf radial parameter is set to $r_{BW} = 1.5 \text{ GeV}^{-1}$. Again, toys are generated
1023 according to this nominal configuration and then fitted whereby the radial parameter is
1024 uniformly varied within the interval $[0, 3] \text{ GeV}^{-1}$.

1025 12.10 Alternative amplitude models

1026 We tested several modifications of the LASSO model to assign an additional model
1027 uncertainty to the measured observables r, δ and $\gamma - 2\beta_s$ as well as to the measured
1028 masses and widths of the $K_1(1400)$ and $K^*(1410)$ resonances. The amplitude coefficients
1029 are by definition parameters of a given model which is why we do not evaluate a model
1030 uncertainty for them. The fit results of the following alternative models (Alt. 1 - Alt. 12)
1031 are summarized in Tables 12.1 and 12.2.

- 1032 • All amplitudes selected by Stage 1 of the model selection are included for both $b \rightarrow c$ and
1033 $b \rightarrow u$ transitions (Alt. 1)
- 1034 • The decay channel $K_1(1270)[D] \rightarrow K^*(892) \pi$, where the $K^*(892) \pi$ system is in relative a
1035 D-wave state, is added (Alt. 2)
- 1036 • The decay channel $K_1(1400) \rightarrow K \rho(770)$ is added (Alt. 12)
- 1037 • The decay channels $K(1460) \rightarrow K \rho(770)$ and $K(1460) \rightarrow K \sigma$ are added (Alt. 3)
- 1038 • The decay channels $K^*(1680) \rightarrow K \rho(770)$ and $K^*(1680) \rightarrow K^*(892) \pi$ are added (Alt. 9)
- 1039 • The decay channel $K_2(1770) \rightarrow K^*(892) \pi$ is added (Alt. 10)
- 1040 • The amplitude $B_s \rightarrow (D_s K)_P \rho(770)$ is replaced by $B_s \rightarrow (D_s K)_S \rho(770)$ (Alt. 11)
- 1041 • Higher orbital angular momentum states are added for the amplitudes: $B_s \rightarrow (D_s \pi)_P K^*(892)$ and $B_s \rightarrow (D_s K)_P \rho(770)$ (Alt. 4 and Alt. 5)
- 1042 • The amplitudes $B_s \rightarrow (D_s K) \sigma$, $B_s \rightarrow (D_s K) f_0(980)$, $B_s \rightarrow (D_s K) f_2(1270)$ and
1043 $B_s \rightarrow (D_s K) f_0(1370)$ are added in different combinations and angular momentum
1044 configurations (Alt. 6, Alt. 7 and Alt. 8)
- 1045 • The decay channels $K_2^*(1430) \rightarrow K \rho(770)$ and $K_2^*(1430) \rightarrow K^*(892) \pi$ are added (not
1046 used)
- 1047 • The amplitudes $B_s \rightarrow (D_s \pi)_P K_0^*(1430)$ and $B_s \rightarrow (D_s K)_S K_2^*(1430)$ are added (not
1048 used)
- 1049 • A flat non-resonant $B_s \rightarrow D_s K \pi \pi$ component is added (not used)

1050 In total 15 different sets of amplitudes are fitted. In some cases, the fit fractions of
1051 additionally added amplitudes turn out to be exactly zero. These model are effectively
1052 not distinguishable from the baseline LASSO model and are not considered further. From
1053 the remaining 12 models, we compute the sample variance for each observable and take it
1054 as model uncertainty.

Table 12.1: Fit fractions in percent for the baseline and several alternative amplitude models (Alt. 1 - Alt. 6). Resonance parameters and the physical observables $r, \kappa, \delta, \gamma - 2\beta_s$ are also given. The values of the physical observables are given relative to the baseline result. The uncertainties are statistical only.

	Baseline	Alt.1	Alt.2	Alt.3	Alt.4	Alt.5	Alt.6
$B_s \rightarrow D_s (K_1(1270) \rightarrow K^*(892) \pi)$	6.2	6.5	6.7	5.2	5.4	6.1	6.0
$B_s \rightarrow D_s (K_1(1270)[D] \rightarrow K^*(892) \pi)$			1.3				
$B_s \rightarrow D_s (K_1(1270) \rightarrow K \rho(770))$	12.3	10.3	9.8	9.4	13.9	11.2	12.9
$B_s \rightarrow D_s (K_1(1270) \rightarrow K \rho(1450))$							
$B_s \rightarrow D_s (K_1(1270) \rightarrow K_0^*(1430) \pi)$	3.3	2.5	2.3	2.6	3.5	2.8	3.5
$B_s \rightarrow D_s (K_1(1400) \rightarrow K^*(892) \pi)$	47.9	54.3	53.5	58.8	47.0	53.7	43.7
$B_s \rightarrow D_s (K_1(1400) \rightarrow K \rho(770))$							
$B_s \rightarrow D_s (K^*(1410) \rightarrow K^*(892) \pi)$	15.9	15.0	15.6	15.7	17.6	15.7	16.1
$B_s \rightarrow D_s (K^*(1410) \rightarrow K \rho(770))$	6.5	5.5	6.2	6.3	6.5	6.5	6.6
$B_s \rightarrow D_s (K(1460) \rightarrow K^*(892) \pi)$		0.8					
$B_s \rightarrow D_s (K(1460) \rightarrow K \rho(770))$							
$B_s \rightarrow D_s (K(1460) \rightarrow K \sigma)$							
$B_s \rightarrow D_s (K^*(1680) \rightarrow K^*(892) \pi)$							
$B_s \rightarrow D_s (K^*(1680) \rightarrow K \rho(770))$							
$b \rightarrow c$							
$B_s \rightarrow (D_s \pi)_S K^*(892)$							
$B_s \rightarrow (D_s \pi)_P K^*(892)$		6.7	9.2	7.9	10.3	13.9	6.8
$B_s[P] \rightarrow (D_s \pi)_P K^*(892)$						0.1	
$B_s[D] \rightarrow (D_s \pi)_P K^*(892)$						0.9	
$B_s \rightarrow (D_s K)_S \sigma$							
$B_s \rightarrow (D_s K)_P \sigma$							
$B_s \rightarrow (D_s K)_S f_0(980)$							
$B_s \rightarrow (D_s K)_S f_2(1270)$							0.0
$B_s \rightarrow (D_s K)_P f_2(1270)$							
$B_s \rightarrow (D_s K)_S f_0(1370)$							
$B_s \rightarrow (D_s K)_S \rho(770)$							
$B_s \rightarrow (D_s K)_P \rho(770)$			0.7			0.1	
$B_s[P] \rightarrow (D_s K)_P \rho(770)$							
$B_s[D] \rightarrow (D_s K)_P \rho(770)$							
Sum	98.9	104.7	103.2	108.3	108.8	103.1	95.2
$b \rightarrow u$							
$B_s \rightarrow D_s (K_1(1270) \rightarrow K^*(892) \pi)$	15.0	20.9	21.0	18.2	11.5	19.1	13.8
$B_s \rightarrow D_s (K_1(1270)[D] \rightarrow K^*(892) \pi)$			4.0				
$B_s \rightarrow D_s (K_1(1270) \rightarrow K \rho(770))$	29.5	33.3	30.8	33.0	29.8	35.2	29.6
$B_s \rightarrow D_s (K_1(1270) \rightarrow K \rho(1450))$							
$B_s \rightarrow D_s (K_1(1270) \rightarrow K_0^*(1430) \pi)$	8.0	8.2	7.2	9.2	7.5	8.9	8.2
$B_s \rightarrow D_s (K_1(1400) \rightarrow K^*(892) \pi)$	15.5	29.5	21.2	22.1	23.5	15.4	19.6
$B_s \rightarrow D_s (K_1(1400) \rightarrow K \rho(770))$							
$B_s \rightarrow D_s (K^*(1410) \rightarrow K^*(892) \pi)$		2.2					
$B_s \rightarrow D_s (K^*(1410) \rightarrow K \rho(770))$		0.8					
$B_s \rightarrow D_s (K(1460) \rightarrow K^*(892) \pi)$	22.3	19.1	12.9	17.2	15.1	21.7	21.9
$B_s \rightarrow D_s (K(1460) \rightarrow K \rho(770))$				3.5			
$B_s \rightarrow D_s (K(1460) \rightarrow K \sigma)$				2.3			
$B_s \rightarrow D_s (K^*(1680) \rightarrow K^*(892) \pi)$							
$B_s \rightarrow D_s (K^*(1680) \rightarrow K \rho(770))$							
$B_s \rightarrow D_s (K_2(1770) \rightarrow K^*(892) \pi)$							
$B_s \rightarrow (D_s \pi)_S K^*(892)$							
$B_s \rightarrow (D_s \pi)_P K^*(892)$		37.6	16.3	23.1	17.3	61.2	29.3
$B_s[P] \rightarrow (D_s \pi)_P K^*(892)$						0.6	
$B_s[D] \rightarrow (D_s \pi)_P K^*(892)$						3.8	
$B_s \rightarrow (D_s K)_S \sigma$							
$B_s \rightarrow (D_s K)_P \sigma$							
$B_s \rightarrow (D_s K)_S f_0(980)$							
$B_s \rightarrow (D_s K)_S f_2(1270)$							0.2
$B_s \rightarrow (D_s K)_P f_2(1270)$							
$B_s \rightarrow (D_s K)_S f_0(1370)$							
$B_s \rightarrow (D_s K)_S \rho(770)$							
$B_s \rightarrow (D_s K)_P \rho(770)$	8.4	8.2	4.8	13.3	8.4	12.6	7.5
$B_s[P] \rightarrow (D_s K)_P \rho(770)$						0.9	
$B_s[D] \rightarrow (D_s K)_P \rho(770)$						0.8	
Sum	136.4	138.7	124.9	136.0	161.5	143.8	142.6
$m_{K_1(1400)} [\text{MeV}]$	1397	1389	1389	1394	1410	1392	1403
$\Gamma_{K_1(1400)} [\text{MeV}]$	205	210	207	220	222	207	205
$m_{K^*(1410)} [\text{MeV}]$	1432	1435	1436	1429	1435	1428	1432
$\Gamma_{K^*(1410)} [\text{MeV}]$	345	351	348	347	360	346	347
r	0.50	0.46	0.48	0.49	0.51	0.49	0.51
κ	0.52	0.61	0.54	0.30	0.53	0.51	0.51
$\delta [{}^\circ]$	46	58	57	46	42	55	45
$\gamma - 2\beta_s [{}^\circ]$	61	70	57	60	54	67	62

Table 12.2: Fit fractions in percent for several alternative amplitude models (Alt. 7 - Alt. 12). Resonance parameters and the physical observables $r, \kappa, \delta, \gamma - 2\beta_s$ are also given. The values of the physical observables are given relative to the baseline result. The uncertainties are statistical only.

		Alt.7	Alt.8	Alt.9	Alt.10	Alt.11	Alt.12
$B_s \rightarrow D_s (K_1(1270) \rightarrow K^*(892) \pi)$ & 6.9 & 7.6 & 6.1 & 6.7 & 8.1 & 6.3 $B_s \rightarrow D_s (K_1(1270)[D] \rightarrow K^*(892) \pi)$ $B_s \rightarrow D_s (K_1(1270) \rightarrow K \rho(770))$ & 13.8 & 12.8 & 13.2 & 11.0 & 14.7 & 14.9 $B_s \rightarrow D_s (K_1(1270) \rightarrow K \rho(1450))$ $B_s \rightarrow D_s (K_1(1270) \rightarrow K_0^*(1430) \pi)$ & 3.8 & 3.1 & 3.3 & 3.3 & 4.0 & 3.3 $B_s \rightarrow D_s (K_1(1400) \rightarrow K^*(892) \pi)$ & 47.8 & 45.7 & 49.8 & 52.6 & 46.4 & 49.9 $B_s \rightarrow D_s (K_1(1400) \rightarrow K \rho(770))$ $B_s \rightarrow D_s (K_1(1400) \rightarrow K \rho(770))$ & 0.6 $B_s \rightarrow D_s (K^*(1410) \rightarrow K^*(892) \pi)$ & 15.4 & 15.5 & 18.8 & 15.2 & 15.5 & 15.9 $B_s \rightarrow D_s (K^*(1410) \rightarrow K \rho(770))$ & 5.8 & 6.0 & 5.2 & 6.3 & 6.2 & 6.3 $B_s \rightarrow D_s (K(1460) \rightarrow K^*(892) \pi)$ $B_s \rightarrow D_s (K(1460) \rightarrow K \rho(770))$ $B_s \rightarrow D_s (K(1460) \rightarrow K \sigma)$ $B_s \rightarrow D_s (K^*(1680) \rightarrow K^*(892) \pi)$ & 0.8 $B_s \rightarrow D_s (K^*(1680) \rightarrow K \rho(770))$ & 0.9 $b \rightarrow c$ $B_s \rightarrow D_s (K_2(1770) \rightarrow K^*(892) \pi)$ & 0.7 $B_s \rightarrow (D_s \pi)_S K^*(892)$ $B_s \rightarrow (D_s \pi)_P K^*(892)$ & 7.8 & 5.7 & 7.7 & 7.3 & 7.1 & 6.5 $B_s [P] \rightarrow (D_s \pi)_P K^*(892)$ $B_s [D] \rightarrow (D_s \pi)_P K^*(892)$ $B_s \rightarrow (D_s K)_S \sigma$ & 1.6 & 0.4 $B_s \rightarrow (D_s K)_P \sigma$ & 2.9 $B_s \rightarrow (D_s K)_S f_0(980)$ $B_s \rightarrow (D_s K)_S f_2(1270)$ $B_s \rightarrow (D_s K)_P f_2(1270)$ $B_s \rightarrow (D_s K)_S f_0(1370)$ $B_s \rightarrow (D_s K)_S \rho(770)$ $B_s \rightarrow (D_s K)_P \rho(770)$ $B_s [P] \rightarrow (D_s K)_P \rho(770)$ $B_s [D] \rightarrow (D_s K)_P \rho(770)$ Sum & 105.7 & 97.4 & 105.8 & 103.1 & 102.0 & 103.8 <hr/> $B_s \rightarrow D_s (K_1(1270) \rightarrow K^*(892) \pi)$ & 9.7 & 14.3 & 14.4 & 19.3 & 8.0 & 13.3 $B_s \rightarrow D_s (K_1(1270)[D] \rightarrow K^*(892) \pi)$ $B_s \rightarrow D_s (K_1(1270) \rightarrow K \rho(770))$ & 19.3 & 24.1 & 31.3 & 31.7 & 14.5 & 31.5 $B_s \rightarrow D_s (K_1(1270) \rightarrow K \rho(1450))$ $B_s \rightarrow D_s (K_1(1270) \rightarrow K_0^*(1430) \pi)$ & 5.3 & 5.9 & 7.8 & 9.5 & 4.0 & 7.1 $B_s \rightarrow D_s (K_1(1400) \rightarrow K^*(892) \pi)$ & 6.8 & 14.3 & 12.0 & 18.7 & 8.9 & 15.7 $B_s \rightarrow D_s (K_1(1400) \rightarrow K \rho(770))$ $B_s \rightarrow D_s (K^*(1410) \rightarrow K^*(892) \pi)$ $B_s \rightarrow D_s (K^*(1410) \rightarrow K \rho(770))$ $B_s \rightarrow D_s (K(1460) \rightarrow K^*(892) \pi)$ & 29.4 & 27.0 & 23.1 & 22.6 & 28.9 & 22.8 $B_s \rightarrow D_s (K(1460) \rightarrow K \rho(770))$ $B_s \rightarrow D_s (K(1460) \rightarrow K \sigma)$ $B_s \rightarrow D_s (K^*(1680) \rightarrow K^*(892) \pi)$ $b \rightarrow u$ $B_s \rightarrow D_s (K^*(1680) \rightarrow K \rho(770))$ $B_s \rightarrow D_s (K_2(1770) \rightarrow K^*(892) \pi)$ & 0.8 $B_s \rightarrow (D_s \pi)_S K^*(892)$ $B_s \rightarrow (D_s \pi)_P K^*(892)$ & 45.5 & 40.9 & 39.3 & 27.0 & 46.6 & 35.3 $B_s [P] \rightarrow (D_s \pi)_P K^*(892)$ $B_s [D] \rightarrow (D_s \pi)_P K^*(892)$ $B_s \rightarrow (D_s K)_S \sigma$ & 0.3 & 0.7 $B_s \rightarrow (D_s K)_P \sigma$ & 0.6 $B_s \rightarrow (D_s K)_S f_0(980)$ $B_s \rightarrow (D_s K)_S f_2(1270)$ $B_s \rightarrow (D_s K)_P f_2(1270)$ $B_s \rightarrow (D_s K)_S f_0(1370)$ $B_s \rightarrow (D_s K)_S \rho(770)$ $B_s \rightarrow (D_s K)_P \rho(770)$ & 4.1 $B_s [P] \rightarrow (D_s K)_P \rho(770)$ $B_s [D] \rightarrow (D_s K)_P \rho(770)$ Sum & 121.6 & 136.5 & 136.5 & 137.5 & 115.0 & 133.1 <hr/> $m_{K_1}(1400)$ [MeV] & 1401 & 1393 & 1399 & 1394 & 1400 & 1393 $\Gamma_{K_1}(1400)$ [MeV] & 195 & 199 & 200 & 208 & 194 & 205 $m_{K^*}(1410)$ [MeV] & 1444 & 1438 & 1413 & 1432 & 1435 & 1433 $\Gamma_{K^*}(1410)$ [MeV] & 329 & 342 & 400 & 351 & 337 & 346 r & 0.44 & 0.46 & 0.49 & 0.46 & 0.46 & 0.49 κ & 0.46 & 0.51 & 0.51 & 0.54 & 0.56 & 0.44 δ [$^\circ$] & 34 & 49 & 47 & 49 & 34 & 44 $\gamma - 2\beta_s$ [$^\circ$] & 54 & 69 & 57 & 68 & 51 & 61							

Table 12.3: Systematic uncertainties on the fit parameters of the fit to $B_s \rightarrow D_s\pi\pi$ data in units of statistical standard deviations.

Fit Parameter	Fit-bias	Background	Acceptance	Resolution	Asymmetries	Mom./z-Scale	Total
p_0^{OS} Run-I	0.05	0.09	0.00	0.99	0.01		1.00
p_1^{OS} Run-I	0.01	0.13	0.01	1.04	0.01		1.05
Δp_0^{OS} Run-I	0.14	0.03	0.15	0.02	0.00		0.21
Δp_1^{OS} Run-I	0.07	0.06	0.15	0.03	0.00		0.18
ϵ_{tag}^{OS} Run-I	0.06	0.17	0.01	0.00	0.00		0.18
$\Delta \epsilon_{tag}^{OS}$ Run-I	0.04	0.01	0.01	0.06	0.00		0.07
p_0^{SS} Run-I	0.03	0.03	0.00	0.56	0.01		0.56
p_1^{SS} Run-I	0.10	0.03	0.01	0.60	0.01		0.60
Δp_0^{SS} Run-I	0.04	0.01	0.10	0.00	0.00		0.11
Δp_1^{SS} Run-I	0.03	0.04	0.12	0.01	0.00		0.13
ϵ_{tag}^{SS} Run-I	0.02	0.02	0.01	0.00	0.00		0.04
$\Delta \epsilon_{tag}^{SS}$ Run-I	0.04	0.03	0.01	0.05	0.00		0.07
p_0^{OS} Run-II	0.02	0.20	0.00	0.93	0.02		0.96
p_1^{OS} Run-II	0.02	0.08	0.00	0.70	0.01		0.70
Δp_0^{OS} Run-II	0.07	0.08	0.00	0.02	0.00		0.11
Δp_1^{OS} Run-II	0.02	0.03	0.00	0.02	0.00		0.04
ϵ_{tag}^{OS} Run-II	0.01	0.16	0.00	0.00	0.00		0.16
$\Delta \epsilon_{tag}^{OS}$ Run-II	0.05	0.05	0.00	0.01	0.00		0.07
p_0^{SS} Run-II	0.10	0.06	0.00	0.60	0.01		0.62
p_1^{SS} Run-II	0.01	0.07	0.00	0.64	0.02		0.64
Δp_0^{SS} Run-II	0.07	0.02	0.00	0.02	0.00		0.08
Δp_1^{SS} Run-II	0.11	0.05	0.00	0.02	0.00		0.12
ϵ_{tag}^{SS} Run-II	0.03	0.03	0.00	0.00	0.00		0.04
$\Delta \epsilon_{tag}^{SS}$ Run-II	0.01	0.03	0.00	0.10	0.00		0.11
A_P Run-II	0.04	0.02	0.01	0.06	0.00		0.08
Δm_s	0.01	0.11	0.02	0.16	0.00	0.67	0.69

Table 12.4: Systematic uncertainties on the fit parameters of the phase-space integrated fit to $B_s \rightarrow D_s K\pi\pi$ data in units of statistical standard deviations.

Fit Parameter	Fit bias	Background	Acceptance	Resolution	Asymmetries	Δm_s	Total
C	0.15	0.03	0.06	0.04	0.15	0.06	0.23
D	0.00	0.18	0.10	0.04	0.01	0.01	0.21
\bar{D}	0.05	0.20	0.13	0.04	0.02	0.01	0.24
S	0.05	0.01	0.06	0.04	0.07	0.10	0.15
\bar{S}	0.07	0.02	0.03	0.04	0.05	0.10	0.14

Table 12.5: Systematic uncertainties on the fit parameters of the full time-dependent amplitude fit to $B_s \rightarrow D_s K\pi\pi$ data in units of statistical standard deviations.

Fit Parameter	Fit bias	Background	Time-Acc.	Resolution	Asymmetries	Δm_s	Pisp-Acc.	Lineshapes	Resonances m, Γ	Form-Factors	Amp. Model	Total
$B_s \rightarrow D_s (K_1(1270) \rightarrow K^*(892)\pi)$ Mag	0.10	0.12	0.01	0.03	0.00	0.01	0.07	0.44	0.22	0.47		0.70
$B_s \rightarrow D_s (K_1(1270) \rightarrow K^*(892)\pi)$ Phase	0.07	0.09	0.01	0.04	0.01	0.01	0.26	0.35	0.32	0.38		0.68
$B_s \rightarrow D_s (K_1(1270) \rightarrow K_0^*(1430)\pi)$ Mag	0.04	0.23	0.00	0.01	0.00	0.00	0.05	1.00	0.10	0.16		1.04
$B_s \rightarrow D_s (K_1(1270) \rightarrow K_0^*(1430)\pi)$ Phase	0.04	0.13	0.00	0.02	0.00	0.00	0.05	3.01	0.13	0.43		3.05
$B_s \rightarrow D_s (K_1(1400) \rightarrow K^*(892)\pi)$ Mag($b \rightarrow c$)	0.13	0.15	0.01	0.08	0.01	0.03	0.14	0.51	0.17	0.36		0.69
$B_s \rightarrow D_s (K_1(1400) \rightarrow K^*(892)\pi)$ Phase($b \rightarrow c$)	0.14	0.17	0.01	0.09	0.01	0.02	0.25	0.44	0.25	0.40		0.73
$B_s \rightarrow D_s (K_1(1400) \rightarrow K^*(892)\pi)$ Mag($b \rightarrow u$)	0.10	0.26	0.03	0.04	0.03	0.09	0.21	0.28	0.17	0.59		0.77
$B_s \rightarrow D_s (K_1(1400) \rightarrow K^*(892)\pi)$ Phase($b \rightarrow u$)	0.02	0.08	0.04	0.03	0.03	0.09	0.23	0.55	0.20	0.28		0.70
$B_s \rightarrow D_s (K^*(1410) \rightarrow K^*(892)\pi)$ Mag($b \rightarrow c$)	0.08	0.10	0.02	0.04	0.01	0.04	0.57	0.31	0.14	0.43		0.81
$B_s \rightarrow D_s (K^*(1410) \rightarrow K^*(892)\pi)$ Phase($b \rightarrow c$)	0.35	0.11	0.01	0.05	0.01	0.01	0.09	0.41	0.16	0.58		0.83
$B_s \rightarrow D_s (K^*(1410) \rightarrow K\rho(770))$ Mag	0.35	0.13	0.01	0.01	0.00	0.01	0.07	0.41	0.08	0.24		0.61
$B_s \rightarrow D_s (K^*(1410) \rightarrow K\rho(770))$ Phase	0.18	0.25	0.00	0.01	0.00	0.01	0.15	0.34	0.09	0.22		0.54
$B_s \rightarrow D_s (K(1460) \rightarrow K^*(892)\pi)$ Mag($b \rightarrow u$)	0.14	0.27	0.03	0.04	0.02	0.04	0.09	0.32	0.20	0.44		0.66
$B_s \rightarrow D_s (K(1460) \rightarrow K\rho(770))$ Mag	0.13	0.14	0.03	0.07	0.02	0.04	0.05	0.53	0.34	0.32		0.74
$B_s \rightarrow (D_s \pi)_P K^*(892)$ Mag($b \rightarrow c$)	0.03	0.21	0.01	0.05	0.01	0.02	0.17	0.71	0.10	0.49		0.91
$B_s \rightarrow (D_s \pi)_P K^*(892)$ Phase($b \rightarrow c$)	0.20	0.31	0.01	0.08	0.01	0.01	0.30	0.58	0.11	0.32		0.82
$B_s \rightarrow (D_s \pi)_P K^*(892)$ Mag($b \rightarrow u$)	0.14	0.08	0.03	0.05	0.01	0.05	0.21	0.50	0.17	0.38		0.71
$B_s \rightarrow (D_s \pi)_P K^*(892)$ Phase($b \rightarrow u$)	0.24	0.22	0.02	0.09	0.01	0.03	0.23	0.70	0.13	0.28		0.87
$B_s \rightarrow (D_s K)_P K^*(892)$ Phase($b \rightarrow u$)	0.35	0.23	0.03	0.02	0.02	0.05	0.22	0.53	0.28	0.54		0.93
$B_s \rightarrow (D_s K)_P \rho(770)$ Mag($b \rightarrow u$)	0.12	0.54	0.02	0.04	0.01	0.05	0.10	0.37	0.31	0.53		0.91
$m_{K_1(1400)}$	0.09	0.15	0.01	0.08	0.01	0.01	0.25	0.22	0.14	0.40		0.80
$\Gamma_{K_1(1400)}$	0.01	0.11	0.01	0.01	0.01	0.01	0.14	0.37	0.10	0.35		0.74
$m_{K^*(1410)}$	0.05	0.07	0.01	0.01	0.00	0.01	0.21	0.23	0.04	1.19		0.59
$\Gamma_{K^*(1410)}$	0.25	0.13	0.00	0.01	0.00	0.01	0.08	0.14	0.04	1.29		1.48
r	0.11	0.31	0.03	0.06	0.02	0.08	0.33	0.39	0.08	0.17		0.52
δ	0.19	0.10	0.04	0.07	0.05	0.10	0.29	0.03	0.11	0.53		0.67
$\gamma - 2\beta_s$	0.10	0.13	0.07	0.13	0.02	0.07	0.04	0.28	0.03	0.11		0.56

1056 13 Summary

1057 The B_s^0 oscillation frequency Δm_s is measured from the time-dependent fit to $B_s^0 \rightarrow D_s\pi\pi\pi$
 1058 data to be

$$\Delta m_s = 17.7651 \pm 0.0084 \pm 0.0058,$$

1059 where the errors are statistical and systematic, respectively. Table 13.1 summarizes the
 1060 values for the ratio of the $b \rightarrow u$ and $b \rightarrow c$ transition amplitudes (r) and their strong
 1061 (δ) and weak phase ($\gamma - 2\beta_s$) difference obtained from the phase-space integrated, as
 1062 well as the time-dependent amplitude fit to $B_s^0 \rightarrow D_s K\pi\pi$ data. Their comparison is
 1063 not so straightforward as the results are obtained from the same data set. We define a
 1064 measure of their compatibility as follows: For the statistical error we take the difference
 1065 of the statistical uncertainties of both fits: $\Delta\sigma_{stat} = \sigma_{stat}^{MI} - \sigma_{stat}^{Full}$, where σ_{stat}^{MI} is the
 1066 statistical uncertainty of the phase-space integrated (model-independent) fit and σ_{stat}^{Full}
 1067 is the statistical uncertainty of the full time-dependent amplitude fit. In the limit of
 1068 equal statistical uncertainties, $\Delta\sigma_{stat} = 0$, and the results should agree perfectly. For
 1069 the systematic error we assume that the model-dependent error (including resonance
 1070 line shapes, form factors and alternative amplitude models) of the full time-dependent
 1071 amplitude fit, σ_{model}^{Full} , is uncorrelated to the phase-space integrated results. The remaining
 1072 systematics (including time-acceptance, resolution, tagging, etc.) are assumed to be 100%
 1073 correlated such that their effect should cancel. Hence, the results should agree within
 1074 a spread given by: $\Delta\sigma = \sqrt{\Delta\sigma_{stat}^2 + (\sigma_{model}^{Full})^2}$. The physical parameters agree within a
 1075 range of 0.4 to 1.4 $\Delta\sigma$.

Table 13.1: Parameters determined from the two fits performed to the $B_s^0 \rightarrow D_s K\pi\pi$ data sample. Statistical and systematic uncertainties are combined.

Parameter	Phase-space integrated fit	Time-dependent amplitude fit	Difference [$\Delta\sigma$]
r	0.41 ± 0.10	0.50 ± 0.05	1.4
κ	0.65 ± 0.21	0.52 ± 0.11	0.8
δ [°]	40 ± 18	46 ± 18	0.6
$\gamma - 2\beta_s$ [°]	65 ± 21	61 ± 17	0.4

1076 A Parametrization of Amplitude Lineshapes

1077 Bugg model for σ resonance

1078 For the broad scalar resonance σ , the model from Bugg is used [53]:

$$T(s) = [M^2 - s - g_1^2 \frac{s - s_A}{M^2 - s_A} z(s) - iM\Gamma_{tot}(s)]^{-1}, \quad (1.1)$$

$$M\Gamma_1(s) = g_1^2 \frac{s - s_A}{M^2 - s_A} \rho_1(s), \quad (1.2)$$

$$g_1^2(s) = M(b_1 + b_2 s) \exp[-(s - M^2)A^{-1}], \quad (1.3)$$

$$j_1(s) = \frac{1}{\pi} [2 + \rho_1 \ln_e \frac{1 - \rho_1}{1 + \rho_1}], \quad (1.4)$$

$$z(s) = j_1(s) - j_1(M^2), \quad (1.5)$$

$$M\Gamma_2(s) = 0.6g_1^2(s) \frac{s}{M^2} \exp(-\alpha|s - 4m_K^2|) \rho_2(s), \quad (1.6)$$

$$M\Gamma_3(s) = 0.2g_1^2(s) \frac{s}{M^2} \exp(-\alpha|s - 4m_\eta^2|) \rho_3(s), \quad (1.7)$$

$$M\Gamma_4(s) = Mg_4 \frac{\rho_{4\pi}(s)}{\rho_{4\pi}(M^2)}, \quad (1.8)$$

$$\rho_2(s) = \sqrt{1 - 4m_\pi^2/s}, \quad (1.9)$$

$$\rho_{4\pi}(s) = 1.0[1 + \exp(7.082 - 2.845s)]^{-1}, \quad (1.10)$$

1079 where the numerical values for the parameters are [53] $M = 0.953 \text{ GeV}$, $b_1 = 1.302 \text{ GeV}$,
1080 $b_2 = 0.340 \text{ GeV}^{-1}$, $A = 2.426 \text{ GeV}^2$, $g_{4\pi} = 0.011 \text{ GeV}$ and $s_A = 0.41m_\pi^2$.

1081 Model for $K\pi$ -S-wave

1082 The LASS parameterization is used to model the $K\pi$ S-wave contribution. It consists of
1083 the $K_0^*(1430)$ resonance together with an effective range non-resonant component [54–56]:

$$T_{LASS}(s) = \frac{\sqrt{s}}{q \cot \delta_L - iq} + e^{2i\delta_L} \frac{m_0 \Gamma_0 \frac{m_0}{q_0}}{m_0^2 - s - i m_0 \Gamma_0 \frac{m_0}{\sqrt{s}} \frac{q}{q_0}} \quad (1.11)$$

1084 with $\cot \delta_L = \frac{1}{aq} + \frac{1}{2}rq$. We use the values for the scattering length $a = 2.07 \pm 0.1 \text{ GeV}$
1085 and effective range parameter $r = 3.32 \pm 0.34 \text{ GeV}$ from Ref. [54, 55].

1086 For systematic studies, the GLASS shape is used:

$$T_{GLASS}(s) = F \sin(\phi_B) e^{i\phi_B} + R \sin(\phi_R) e^{i\phi_R} e^{2i\phi_B} \quad (1.12)$$

$$\phi_B = \psi_B + \tan^{-1} \left(\frac{2aq(s)}{2 + arq^2(s)} \right) \quad (1.13)$$

$$\phi_R = \psi_R + \tan^{-1} \left(\frac{m\Gamma(s)}{m_0^2 - s} \right), \quad (1.14)$$

1087 with $F = 0.62 \pm 0.04$, $\phi_F = -0.100 \pm 0.010$, $R = 1$, $\phi_R = 1.10 \pm 0.02$, $a = 0.224 \pm$
1088 0.003 GeV^{-1} and $r = -15.01 \pm 0.13 \text{ GeV}^{-1}$.

1089 **Model for $\rho^0(770)$ resonance**

1090 We use the Gounaris-Sakurai parametrization for the $\rho(770)^0 \rightarrow \pi\pi$ propagator [57]:

$$T_{GS}(m) = \frac{1 + f(0)/m_0^2}{m_0^2 + f(m) - m^2 - i m_0 \Gamma(m)}, \quad (1.15)$$

1091 where $\Gamma(m)$ takes on the same form as in Eq. 2.16 and the function $f(m)$ is defined as

$$f(m) = \Gamma_0 \frac{m_0^2}{q_0^3} \left[q^2 (h(m) - h(m_0)) + (m^2 - m_0^2) q_0^2 \frac{dh}{dm} \Big|_{m_0} \right] \quad (1.16)$$

$$h(m) = \frac{2}{\pi} \frac{q}{m} \ln \left(\frac{m + 2q}{2m_\pi} \right). \quad (1.17)$$

1092 For the decay chain $K_1(1270) \rightarrow \rho(770)K$, we include $\rho - \omega$ mixing [58]:

$$T(s) = T_{GS}(s) \cdot \left(1 + \delta \frac{s}{m_\omega^2} T_\omega(s) \right) \quad (1.18)$$

1093 where T_ω is the relativistic Breit-Wigner propagator (Eq. 2.16) of the ω and the relative
1094 magnitude and phase between ρ and ω fixed to the values determined in Ref. [59, 60]:
1095 $|\delta| = 0.159 \pm 0.012 \pm 0.011$ and $\arg(\delta) = 1.36 \pm 0.07 \pm 0.06$.

1096 **Running width distributions for 3-body resonances**

1097 For the resonances $K_1(1270)$ and $K(1460)$, the energy-dependent widths are reproduced
1098 from Ref. [23]. We further use the energy-dependent widths for the $K_1(1400)$, $K^*(1410)$
1099 and $K^*(1680)$ mesons from Ref. [12]. For all other resonances decaying into a three-
1100 body final state, an energy-dependent width distribution is derived from Equation 2.17
1101 assuming an uniform phase space population. The running width distributions of the
1102 3-body resonances included in the baseline model are shown in Fig. 1.1.

1103 **Additional models**

1104 Lineshape models for resonances which are not part of the nominal model, can be found
1105 in the References. The energy-dependent width of the $f_0(980)$ resonance is given by the
1106 sum of the partial widths into the $\pi\pi$ and KK channels (*i.e.* the Flatté lineshape [61]),
1107 where the coupling constants as well as the mass and width are taken from a measurement
1108 performed by the BES Collaboration [62]. For the $f_2(1270)$ and the $f_0(1370)$ mesons we
1109 use the total decay widths calculated in Ref. [12] which take the channels $\pi\pi$, KK , $\eta\eta$ and
1110 $\pi\pi\pi\pi$ into account.

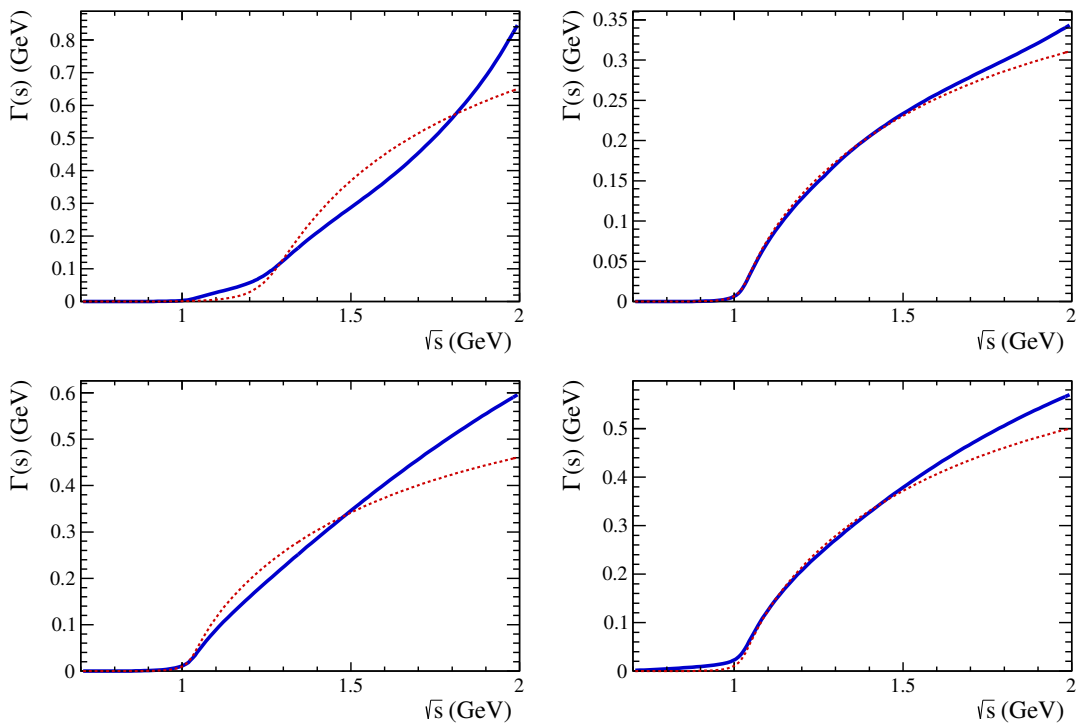


Figure 1.1: Running width distributions of the 3-body resonances included in the baseline model: $K_1(1270)$ (top-left), $K_1(1400)$ (top-right), $K(1460)$ (bottom-left) and $K^*(1410)$ (bottom-right). The nominal models are shown in blue, alternative models used for systematic studies in red.

1111 B Stripping and Trigger cuts

1112 The following text describes variables which are used in Table A.1 and might be ambiguous,
 1113 or which benefits are not straight forward. Where noted, different cut values are applied
 1114 for Run-I and Run-II data. In Table A.1, DOCA is the abbreviation for distance of closest
 1115 approach. This variable is used to ensure that all D_s and $X_{s,d}$ daughters originate from
 1116 the same vertex. DIRA is the abbreviation for the cosine of the angle θ between the
 hadron's flight direction \vec{x} and it's corresponding momentum vector \vec{p} , $\cos \theta_{\vec{x}-\vec{p}}$.

Table A.1: Summary of the stripping selections for $B_s^0 \rightarrow D_s K \pi \pi$ decays. The requirements for Run-II are only given if they have been changed.

Variable	Stripping Cut (Run-I)	Stripping Cut (Run-II)
Track χ^2/nDoF	< 3	
Track p	$> 1000 \text{ MeV}/c$	
Track p_T	$> 100 \text{ MeV}/c$	
Track IP χ^2	> 4	
Track ghost-prob.	< 0.4	
D_s mass	$m_{D_s} \pm 100 \text{ MeV}$	$m_{D_s} \pm 80 \text{ MeV}$
D_s Daughter p_T	$\sum_{i=1}^3 p_{t,i} > 1800 \text{ MeV}/c$	
D_s Daughter DOCA	$< 0.5 \text{ mm}$	
D_s Vertex χ^2/nDoF	< 10	
D_s χ^2 -separation from PV	> 36	
D_s daughter PID(π)	< 20	
D_s daughter PID(K)	> -10	
$X_{s,d}$ mass	$< 4000 \text{ MeV}$	$< 3500 \text{ MeV}$
$X_{s,d}$ Daughter p	$> 2 \text{ GeV}/c$	
$X_{s,d}$ Daughter DOCA	$< 0.4 \text{ mm}$	
$X_{s,d}$ Daughter p_T	$\sum_{i=1}^3 p_{t,i} > 1250 \text{ MeV}/c$	
$X_{s,d}$ Vertex χ^2/nDoF	< 8	
$X_{s,d}$ χ^2 -separation from PV	> 16	
$X_{s,d}$ DIRA	> 0.98	
$X_{s,d}$ $\Delta\rho$	$> 0.1 \text{ mm}$	
$X_{s,d}$ Δz	$> 2.0 \text{ mm}$	
$X_{s,d}$ daughter PID(π)	< 10	
X_s daughter PID(K)	> -2	> 4
B_s^0 mass	$[4750, 7000] \text{ MeV}/c^2$	$[5000, 6000] \text{ MeV}/c^2$
B_s^0 DIRA	> 0.98	> 0.99994
B_s^0 min IP χ^2	< 25	< 20
B_s^0 Vertex χ^2/nDoF	< 10	< 8
$B_s^0 \tau_{B_s^0}$	$> 0.2 \text{ ps}$	

1117

1118 Table A.2 summarizes the trigger requirements imposed by the Hlt1 line used in this
1119 analysis for Run-I. At least one of the six decay particles must pass the listed requirements
1120 in order for the event to be stored for further analysis. For Run-II, this trigger line was
1121 updated and uses a multivariate classifier which takes the variables listed in Table A.2 as
1122 input, rather than directly cutting on them.

1123 The Hlt2 2, 3 and 4-body topological lines use a Boosted Decision Tree based on the
1124 b-hadron p_T , its flight distance χ^2 from the nearest PV and the sum of the B_s^0 and D_s
1125 vertex χ^2 divided by the sum of their number of degrees of freedom. Table A.3 summarizes
1126 the cuts applied by the inclusive ϕ trigger, which requires that a $\phi \rightarrow KK$ candidate can
be formed out of two tracks present in the event.

Table A.2: Summary of the cuts applied by the Hlt1TrackAllL0 trigger for Run-I. At least one of the six decay particles must pass this requirements, in order for the event to be accepted.

Quantity	Hlt1TrackAllL0 requirement
Track IP [mm]	> 0.1
Track IP χ^2	> 16
Track χ^2/nDoF	< 2.5
Track p_T	$> 1.7 \text{ GeV}/c$
Track p	$> 10 \text{ GeV}/c$
Number VELO hits/track	> 9
Number missed VELO hits/track	< 3
Number OT+IT $\times 2$ hits/track	> 16

Table A.3: Summary of the cuts applied by the Hlt2 inclusive ϕ trigger. A $\phi \rightarrow KK$ candidate, formed by two tracks in the event, must pass this requirements in order for the event to be accepted.

Quantity	Hlt2IncPhi requirement
ϕ mass	$m_\phi \pm 12 \text{ MeV}/c^2$ of PDG value
ϕp_T	$> 2.5 \text{ GeV}/c$
ϕ vertex χ^2/nDoF	< 20
ϕ IP χ^2 to any PV	> 5

1127

C Details of multivariate classifier

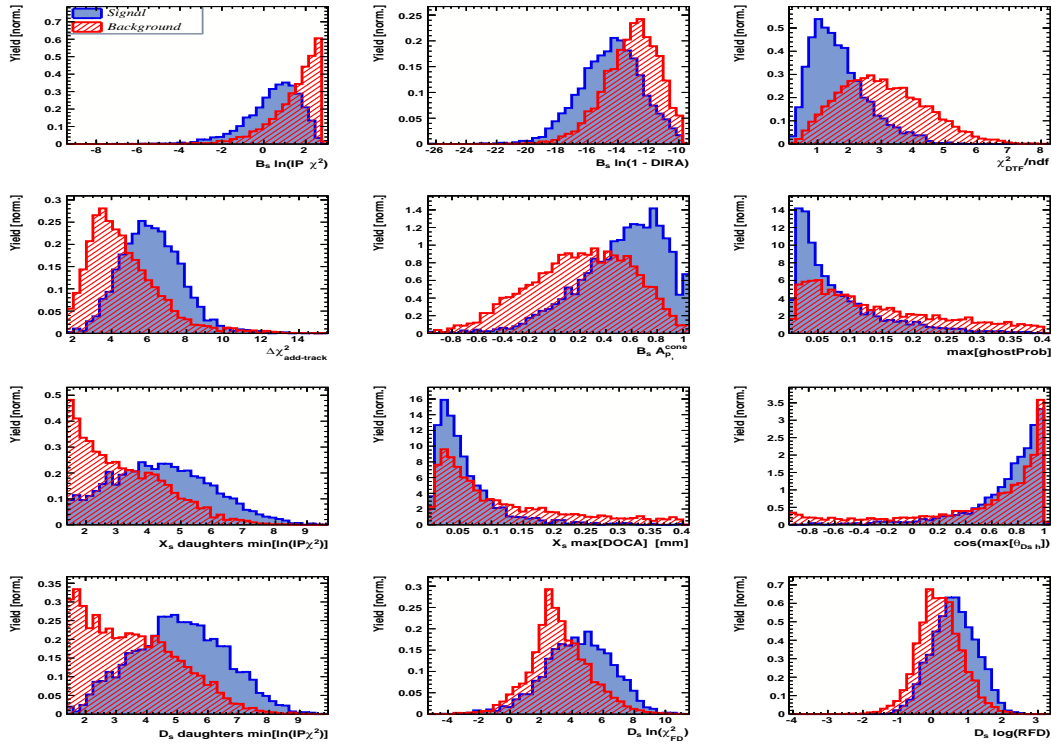


Figure B.1: Variables used to train the BDTG for category [Run-I,L0-TOS].

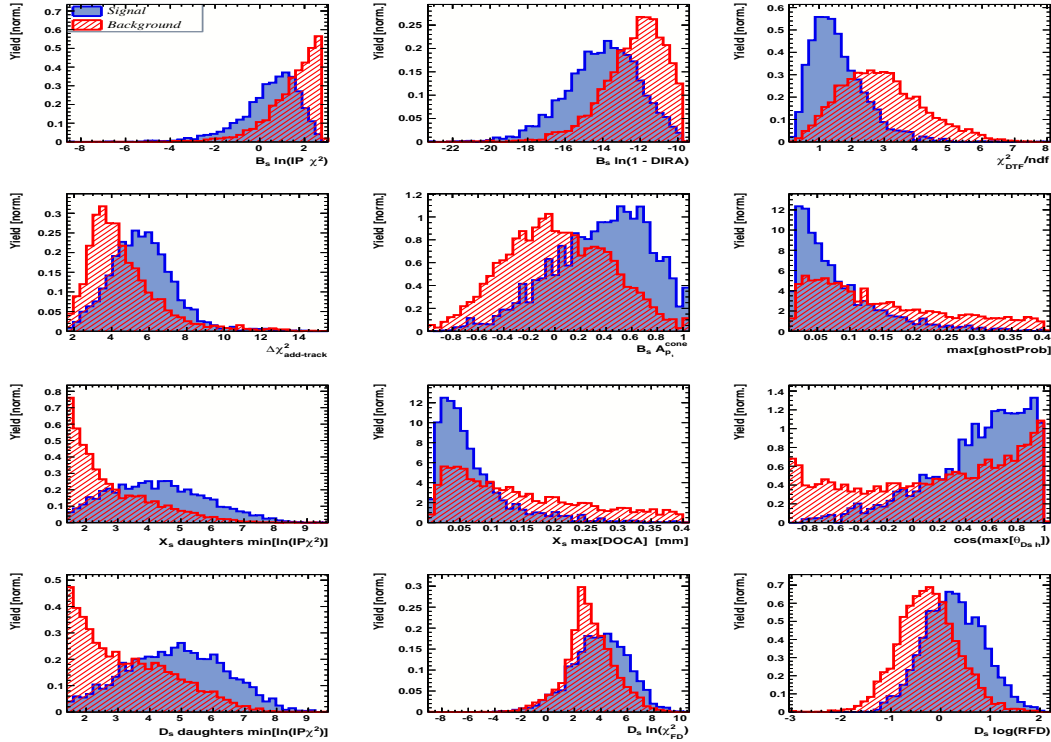


Figure B.2: Variables used to train the BDTG for category [Run-I,L0-TIS].

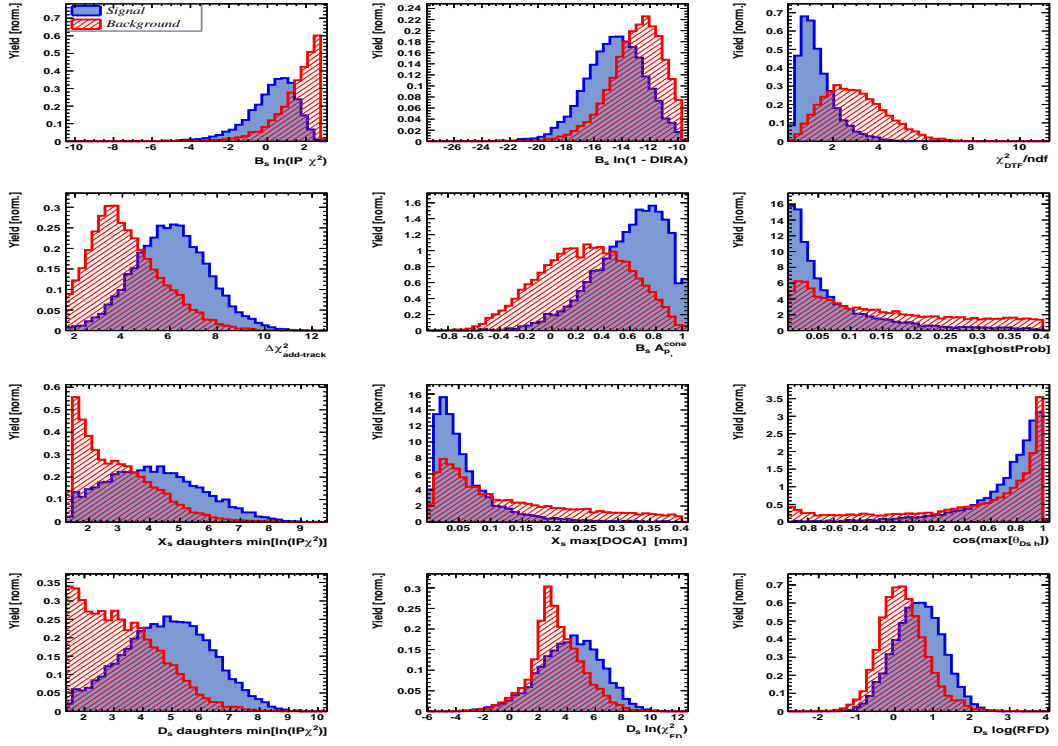


Figure B.3: Variables used to train the BDTG for category [Run-II,L0-TOS].

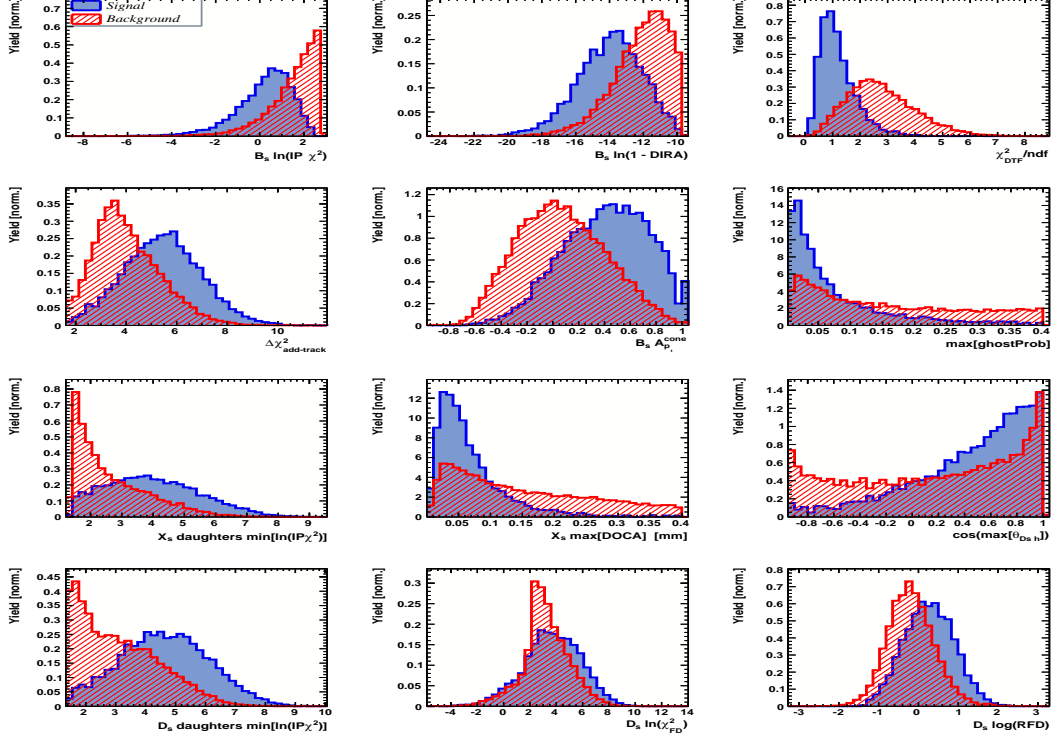


Figure B.4: Variables used to train the BDTG for category [Run-II,L0-TIS].

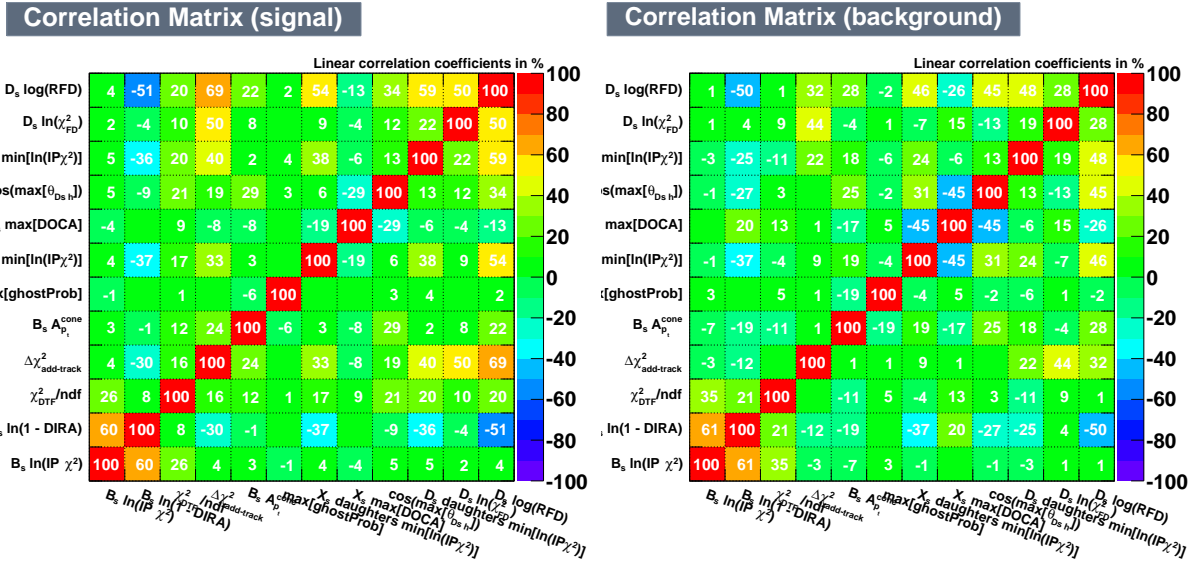


Figure B.5: Correlation matrix for the (left) signal and (right) background input distributions.

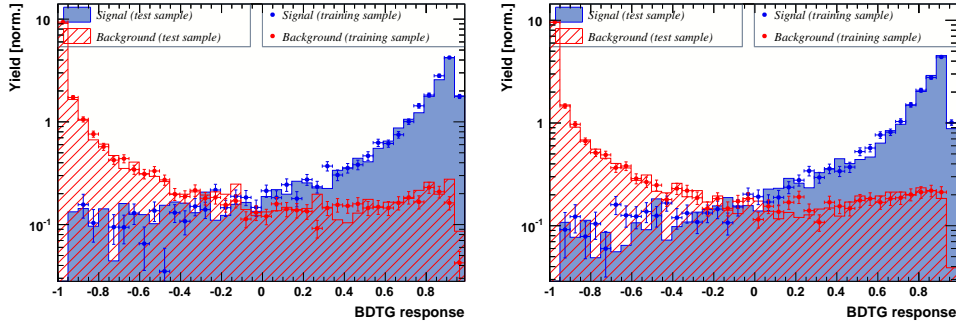


Figure B.6: Response of the classifier trained on the even and tested on the odd sample (left) and trained on the odd and tested on the even sample (right) for category [Run-I,L0-TOS].

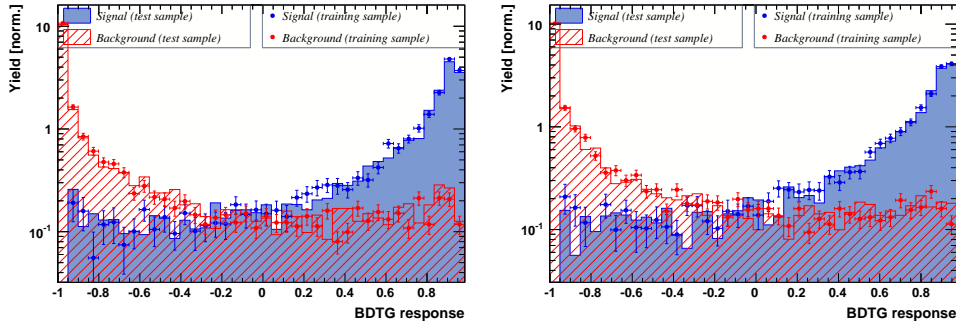


Figure B.7: Response of the classifier trained on the even and tested on the odd sample (left) and trained on the odd and tested on the even sample (right) for category [Run-I,L0-TIS].

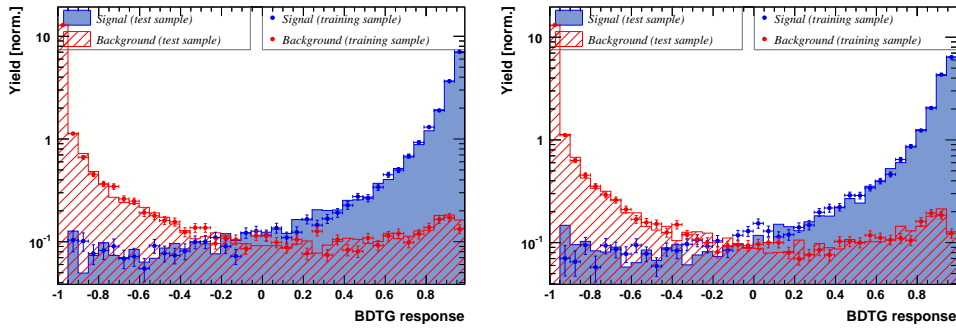


Figure B.8: Response of the classifier trained on the even and tested on the odd sample (left) and trained on the odd and tested on the even sample (right) for category [Run-II,L0-TOS].

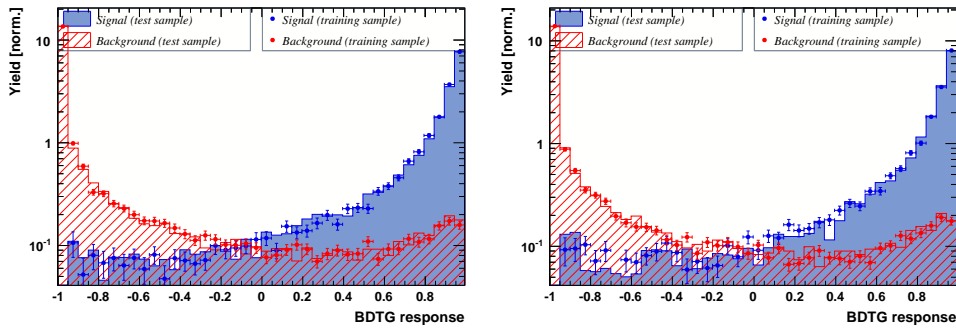


Figure B.9: Response of the classifier trained on the even and tested on the odd sample (left) and trained on the odd and tested on the even sample (right) for category [Run-II,L0-TIS].

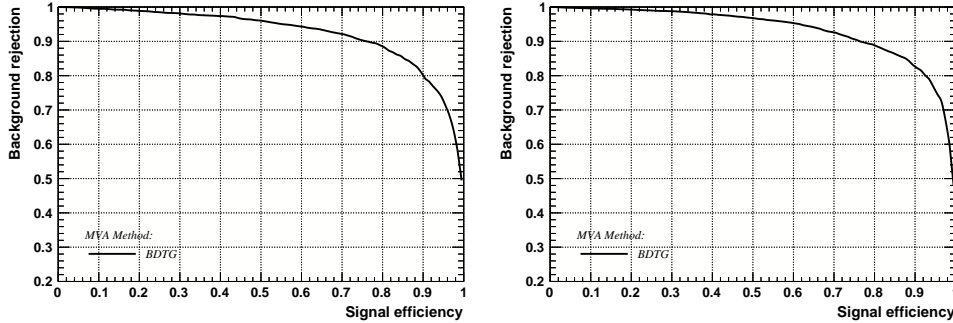


Figure B.10: Signal efficiency versus background rejection for the BDT trained on the even (left) and odd (right) sample for category [Run-I,L0-TOS].

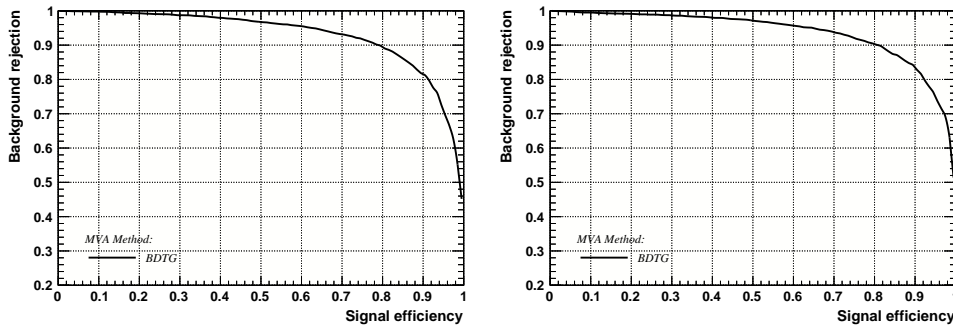


Figure B.11: Signal efficiency versus background rejection for the BDT trained on the even (left) and odd (right) sample for category [Run-I,L0-TIS].

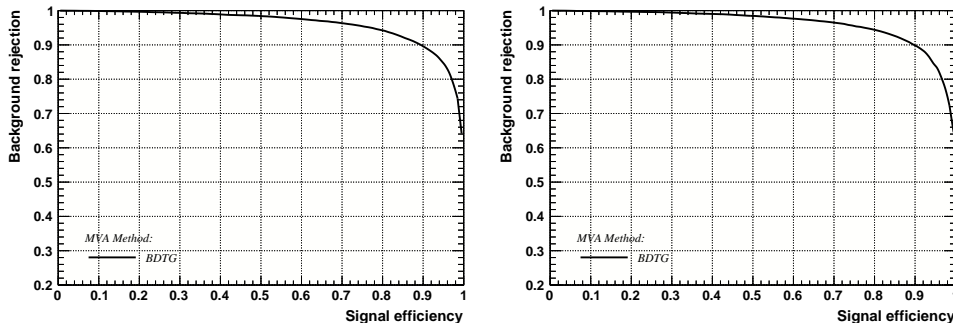


Figure B.12: Signal efficiency versus background rejection for the BDT trained on the even (left) and odd (right) sample for category [Run-II,L0-TOS].

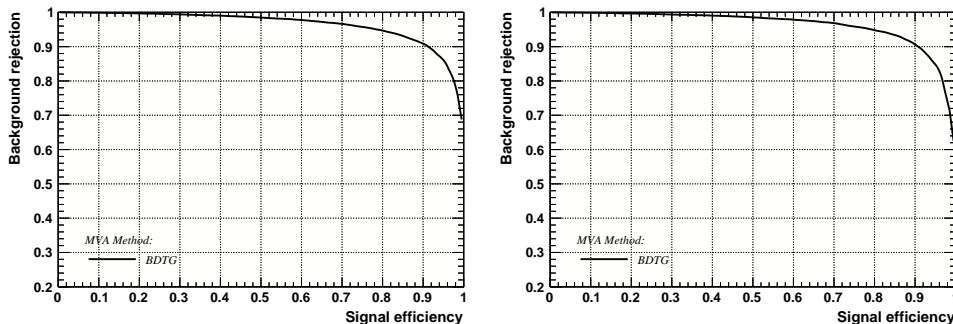


Figure B.13: Signal efficiency versus background rejection for the BDT trained on the even (left) and odd (right) sample for category [Run-II,L0-TIS].

¹¹²⁹ D Detailed mass fits

¹¹³⁰ In this section, all fits to the mass distribution of $B_s^0 \rightarrow D_s\pi\pi\pi$ and $B_s^0 \rightarrow D_sK\pi\pi$
¹¹³¹ candidates are shown. The fits are performed simultaneously in run period (Run-I, Run-
¹¹³² II), D_s final state ($D_s \rightarrow KK\pi$ non-resonant, $D_s \rightarrow \phi\pi$, $D_s \rightarrow K^*K$, or $D_s \rightarrow \pi\pi\pi$) and
¹¹³³ L0 trigger category.

Table C.1: Signal and background yields for the $B_s \rightarrow D_s\pi\pi\pi$ sample split by data-taking period.

Component	Yield for Run I
$B_s \rightarrow D_s\pi\pi\pi$	21443 ± 122
$B^0 \rightarrow D_s\pi\pi\pi$	358 ± 53
Partially reconstructed bkg.	8657 ± 104
Combinatorial bkg.	9492 ± 120
Component	Yield for Run II
$B_s \rightarrow D_s\pi\pi\pi$	82711 ± 257
$B^0 \rightarrow D_s\pi\pi\pi$	1359 ± 1326
Partially reconstructed bkg.	34471 ± 937
Combinatorial bkg.	31574 ± 680

Table C.2: Signal and background yields for the $B_s \rightarrow D_sK\pi\pi$ sample split by data-taking period.

Component	Yield for Run I
$B_s \rightarrow D_sK\pi\pi$	1018 ± 56
$B^0 \rightarrow D_sK\pi\pi$	846 ± 43
Partially reconstructed bkg.	232 ± 137
Misidentified bkg.	426 ± 0
Combinatorial bkg.	2520 ± 324
Component	Yield for Run II
$B_s \rightarrow D_sK\pi\pi$	4153 ± 76
$B^0 \rightarrow D_sK\pi\pi$	3264 ± 86
Partially reconstructed bkg.	1592 ± 312
Misidentified bkg.	760 ± 0
Combinatorial bkg.	6653 ± 186

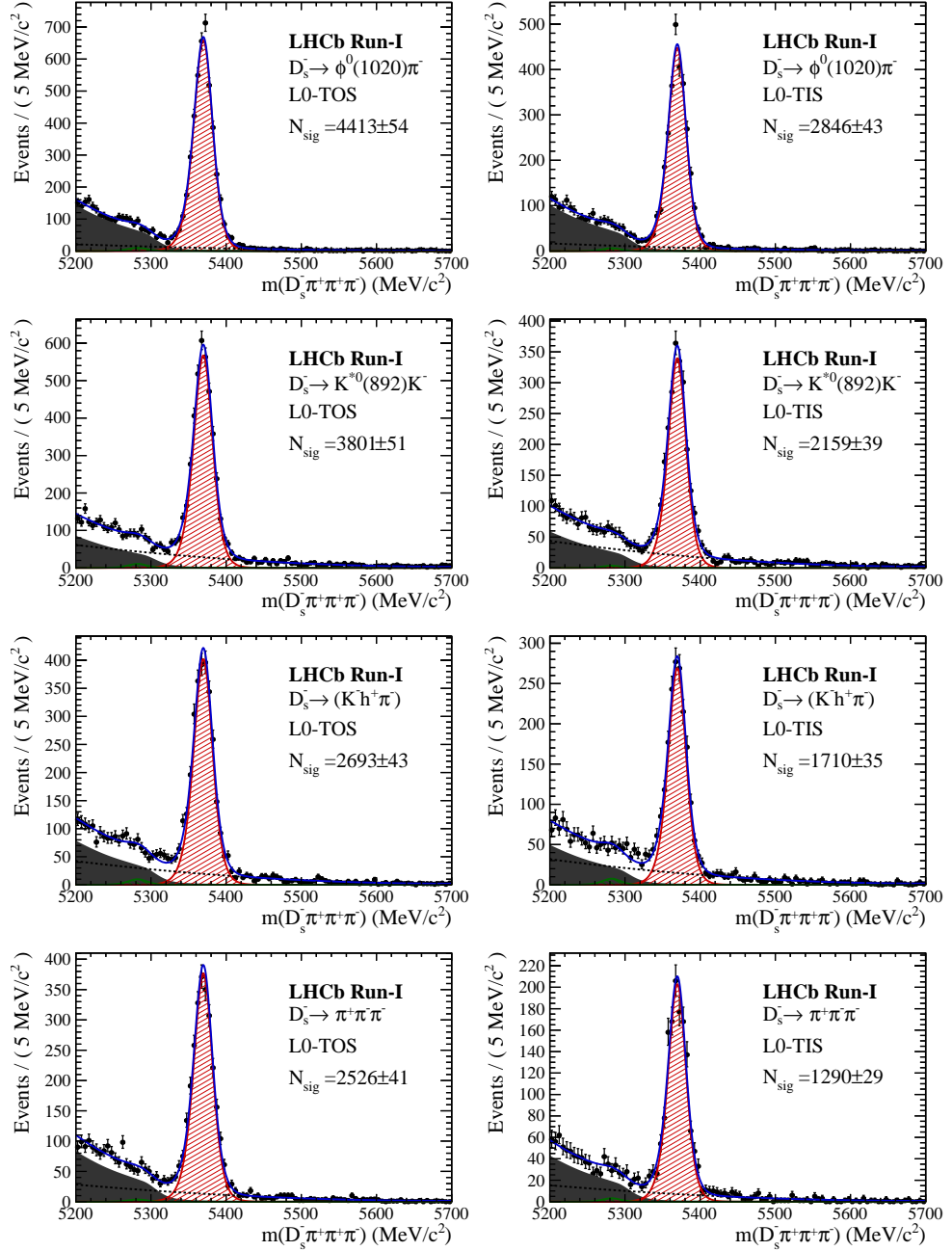


Figure C.1: Invariant mass distributions of $B_s^0 \rightarrow D_s \pi\pi\pi$ candidates for Run-I data.

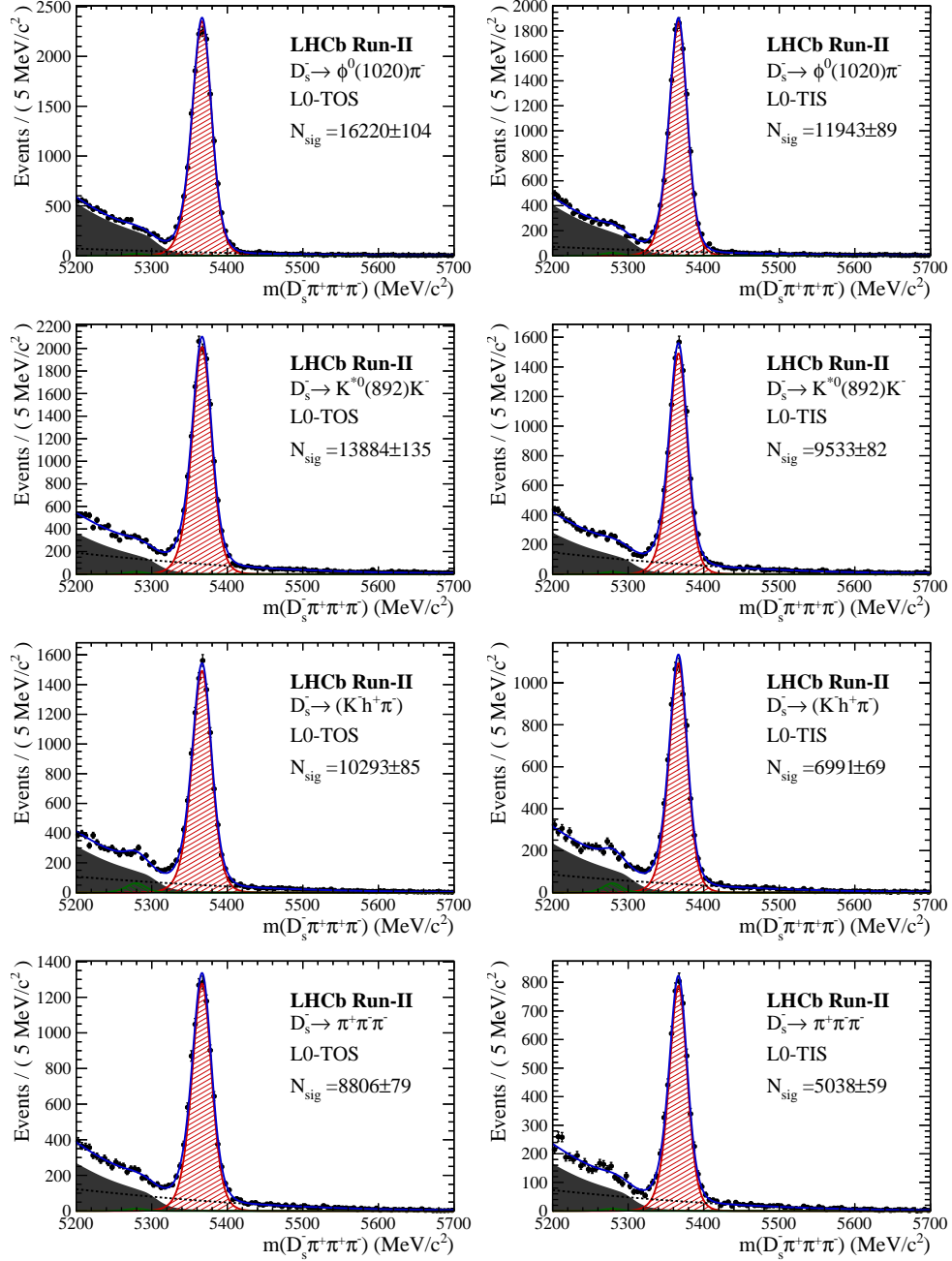


Figure C.2: Invariant mass distributions of $B_s^0 \rightarrow D_s \pi^+ \pi^- \pi^+ \pi^-$ candidates for Run-II data.

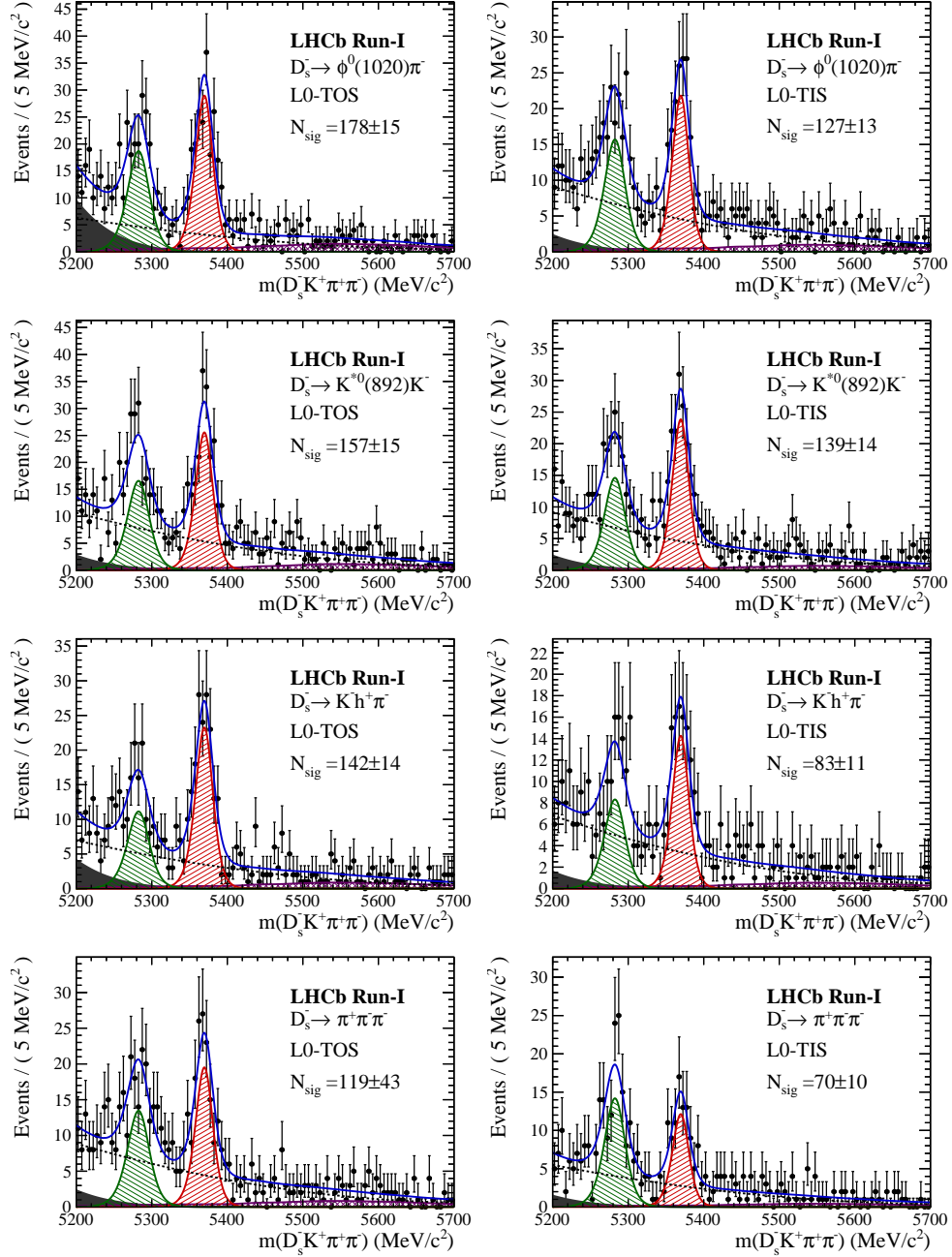


Figure C.3: Invariant mass distributions of $B_s^0 \rightarrow D_s K \pi\pi$ candidates for Run-I data.

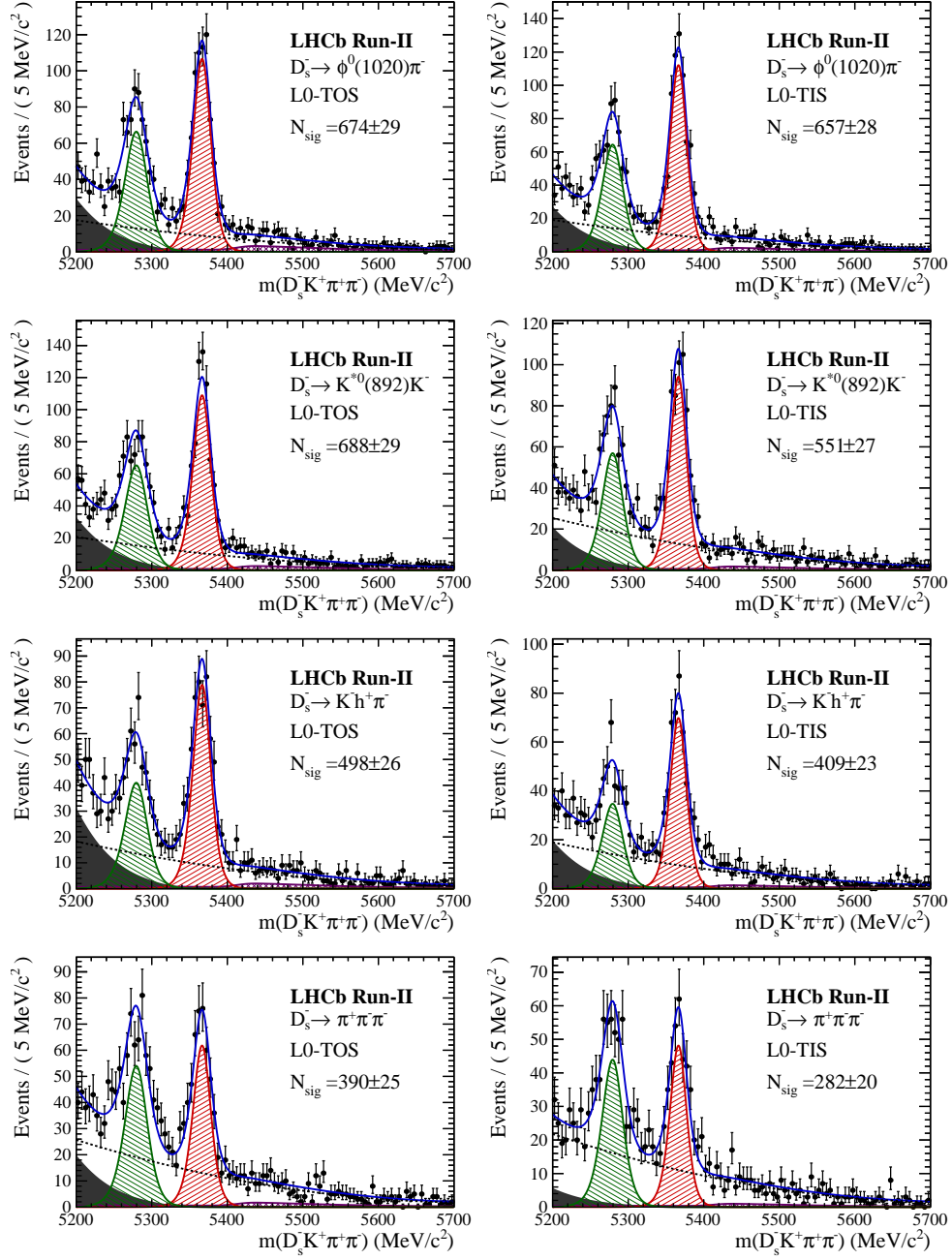


Figure C.4: Invariant mass distributions of $B_s^0 \rightarrow D_s K \pi \pi$ candidates for Run-II data.

1134 E Decay-time Resolution fits

1135 This section contains all fits to the distributions of the decay time difference Δt between
 1136 the true and the reconstructed decay time of the truth-matched B_s^0 candidates on MC.
 1137 The fits are performed in bins of the decay time error σ_t , where an adaptive binning
 1138 scheme is used to ensure that approximately the same number of events are found in each
 1139 bin.

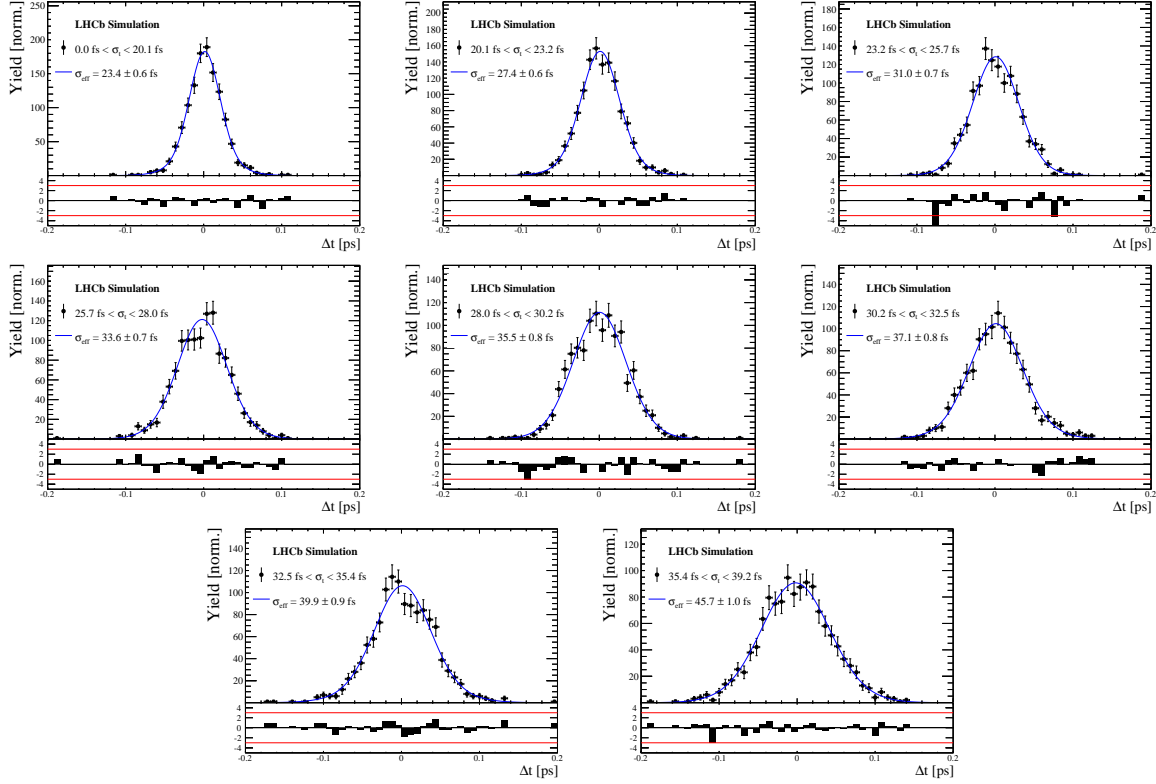


Figure D.1: Difference of the true and measured decay time of $B_s^0 \rightarrow D_s K\pi\pi$ MC candidates in bins of the per-event decay time error estimate..

Table D.1: Measured time resolution for $B_s \rightarrow D_s K\pi\pi$ MC in bins of the per-event decay time error estimate.

σ_t Bin [fs]	σ_1 [fs]	σ_2 [fs]	f_1	D	σ_{eff} [fs]
0.0 - 20.1	19 ± 0.675	33.8 ± 1.77	0.75 ± 0	0.917 ± 0.00406	23.4 ± 0.599
20.1 - 23.2	23.4 ± 0.86	37.4 ± 1.95	0.75 ± 0	0.888 ± 0.00477	27.4 ± 0.621
23.2 - 25.7	28.1 ± 1.02	38.7 ± 2.32	0.75 ± 0	0.86 ± 0.00563	31 ± 0.671
25.7 - 28.0	30.1 ± 1.12	43.2 ± 2.56	0.75 ± 0	0.837 ± 0.00651	33.6 ± 0.734
28.0 - 30.2	32.4 ± 1.12	44.2 ± 2.59	0.75 ± 0	0.819 ± 0.00694	35.5 ± 0.756
30.2 - 32.5	32.6 ± 1.38	49.2 ± 3.04	0.75 ± 0	0.805 ± 0.00792	37.1 ± 0.841
32.5 - 35.4	34.4 ± 1.19	54.7 ± 2.85	0.75 ± 0	0.778 ± 0.0086	39.9 ± 0.879
35.4 - 39.2	41.9 ± 1.8	56.9 ± 4.18	0.75 ± 0	0.719 ± 0.00997	45.7 ± 0.962
39.2 - 44.7	42.2 ± 1.56	68.1 ± 4.01	0.75 ± 0	0.687 ± 0.0114	48.8 ± 1.08
44.7 - 120.0	55.5 ± 2.59	83 ± 14.7	0.75 ± 0	0.546 ± 0.0521	62 ± 4.89

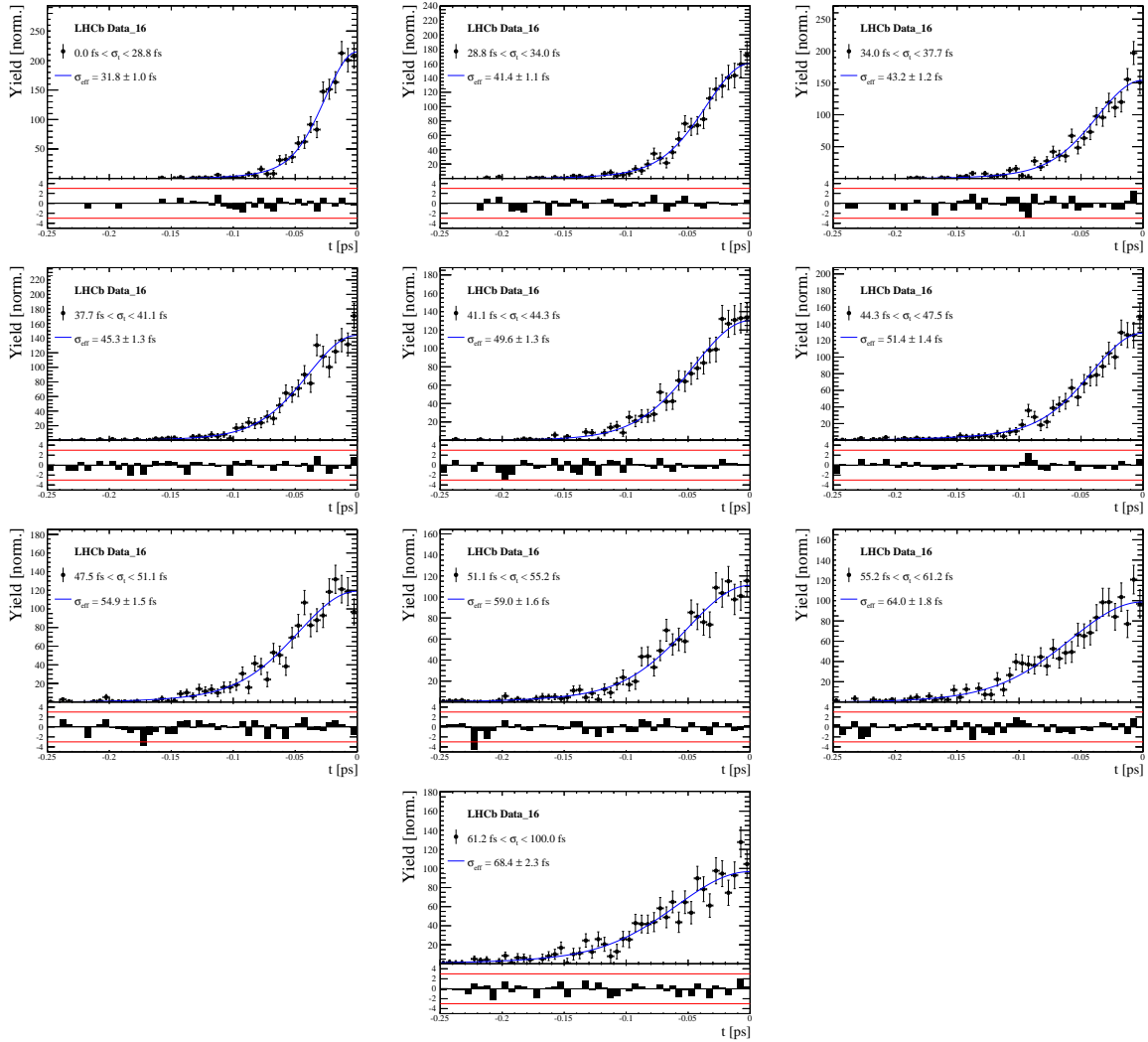


Figure D.2: Decay-time distribution for fake B_s candidates from promptly produced D_s candidates, combined with random prompt $K\pi\pi$ bachelor tracks, for bins in the per-event decay time error estimate. Data taken in 2016.

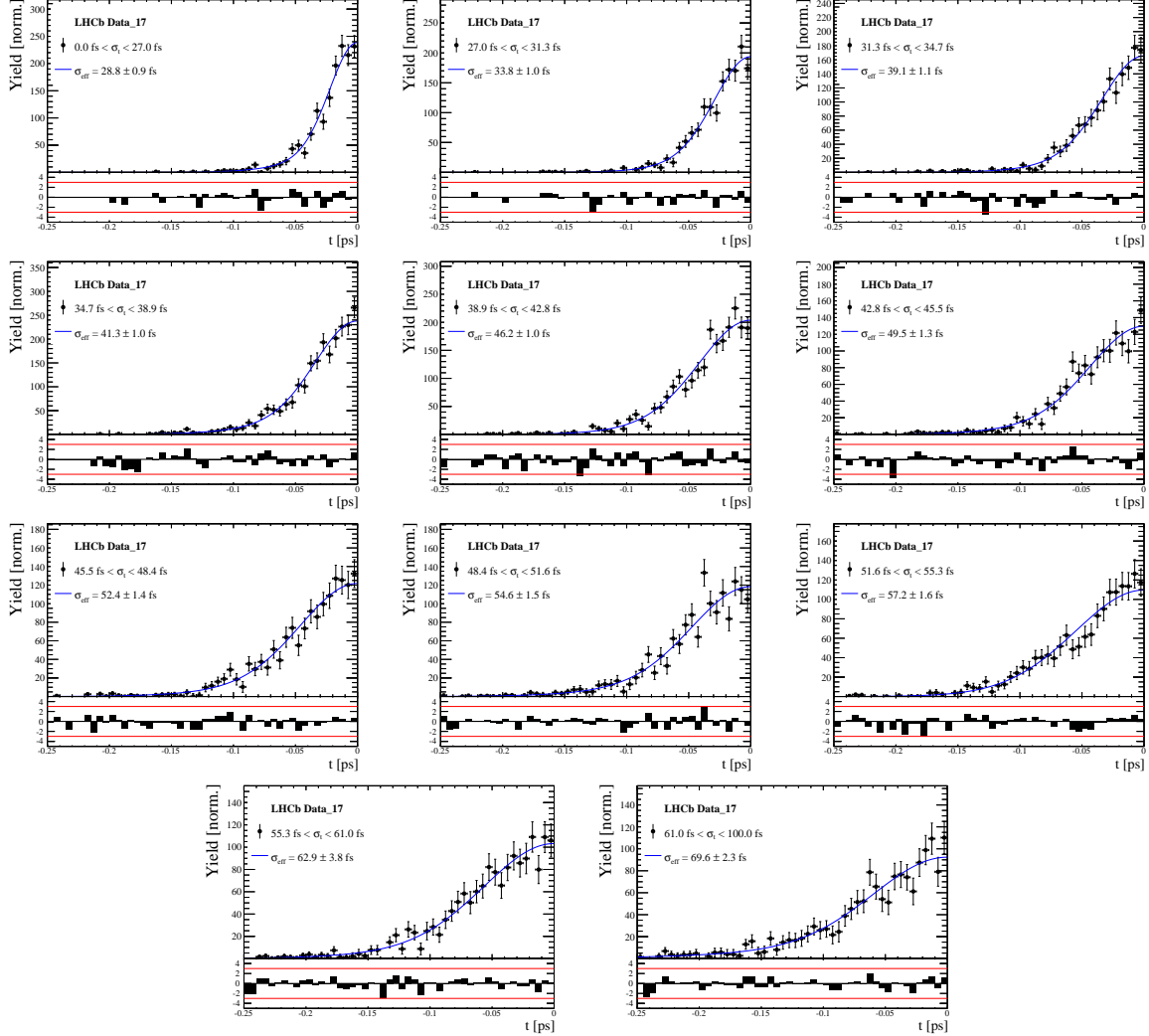


Figure D.3: Decay-time distribution for fake B_s candidates from promptly produced D_s candidates, combined with random prompt $K\pi\pi$ bachelor tracks, for bins in the per-event decay time error estimate. Data taken in 2017.

Table D.2: Measured time resolution for prompt- D_s data in bins of the per-event decay time error estimate. Data taken in 2016.

σ_t Bin [fs]	σ_1 [fs]	σ_2 [fs]	f_1	D	σ_{eff} [fs]
0.0 - 28.8	25.3 ± 1.05	47.8 ± 2.82	0.75 ± 0	0.853 ± 0.00827	31.8 ± 0.967
28.8 - 34.0	34.4 ± 1.38	60.4 ± 3.66	0.75 ± 0	0.763 ± 0.0114	41.4 ± 1.14
34.0 - 37.7	35.9 ± 1.7	63.1 ± 4.05	0.75 ± 0	0.745 ± 0.0122	43.2 ± 1.2
37.7 - 41.1	38.3 ± 1.63	65.3 ± 4.28	0.75 ± 0	0.723 ± 0.013	45.3 ± 1.26
41.1 - 44.3	43.6 ± 2.04	67.2 ± 4.78	0.75 ± 0	0.679 ± 0.0137	49.6 ± 1.3
44.3 - 47.5	40.4 ± 1.64	85.4 ± 5.28	0.75 ± 0	0.659 ± 0.0151	51.4 ± 1.41
47.5 - 51.1	46.1 ± 2.02	82.5 ± 5.61	0.75 ± 0	0.622 ± 0.0161	54.9 ± 1.5
51.1 - 55.2	49.2 ± 2.1	92.3 ± 6.57	0.75 ± 0	0.577 ± 0.0174	59 ± 1.62
55.2 - 61.2	56.6 ± 2.53	88.8 ± 7.84	0.75 ± 0	0.525 ± 0.0192	64 ± 1.82
61.2 - 100.0	57.6 ± 3.09	112 ± 14.5	0.75 ± 0	0.478 ± 0.0232	68.4 ± 2.25

Table D.3: Measured time resolution for prompt- D_s data in bins of the per-event decay time error estimate. Data taken in 2017.

σ_t Bin [fs]	σ_1 [fs]	σ_2 [fs]	f_1	D	σ_{eff} [fs]
0.0 - 27.0	22.1 ± 0.942	44.7 ± 2.65	0.75 ± 0	0.877 ± 0.00729	28.8 ± 0.914
27.0 - 31.3	28.3 ± 1.12	48.2 ± 2.98	0.75 ± 0	0.835 ± 0.00854	33.8 ± 0.959
31.3 - 34.7	32.8 ± 1.29	55.8 ± 3.39	0.75 ± 0	0.786 ± 0.0105	39.1 ± 1.08
34.7 - 38.9	33.4 ± 1.2	62.5 ± 3.04	0.75 ± 0	0.764 ± 0.00951	41.3 ± 0.956
38.9 - 42.8	40.3 ± 1.39	63 ± 3.58	0.75 ± 0	0.715 ± 0.0104	46.2 ± 1
42.8 - 45.5	42.2 ± 1.63	70.7 ± 4.35	0.75 ± 0	0.68 ± 0.0138	49.5 ± 1.3
45.5 - 48.4	44.7 ± 1.85	75.7 ± 4.91	0.75 ± 0	0.649 ± 0.0152	52.4 ± 1.42
48.4 - 51.6	46.3 ± 2.05	80.3 ± 5.66	0.75 ± 0	0.626 ± 0.0161	54.6 ± 1.5
51.6 - 55.3	53.2 ± 1.2	69.1 ± 3.03	0.75 ± 0	0.597 ± 0.0167	57.2 ± 1.55
55.3 - 61.0	54.8 ± 2.29	90.9 ± 12.2	0.75 ± 0	0.535 ± 0.0406	62.9 ± 3.82
61.0 - 100.0	58.4 ± 3.18	118 ± 15.6	0.75 ± 0	0.466 ± 0.0233	69.6 ± 2.28

1140 F Comparison of time-acceptance in subsamples

1141 Figure E.1 shows the spline coefficients obtained by fitting the decay-time distribution of
 1142 $B_s^0 \rightarrow D_s\pi\pi\pi$ data candidates in different subsamples. Sufficient agreement is observed
 1143 within a given data-taking period, while the acceptance shapes for Run-I and Run-II
 1144 data differ significantly. The fitted splines for the different D_s final states are in a good
 1145 agreement. The largest deviations are observed between the different L0 categories.

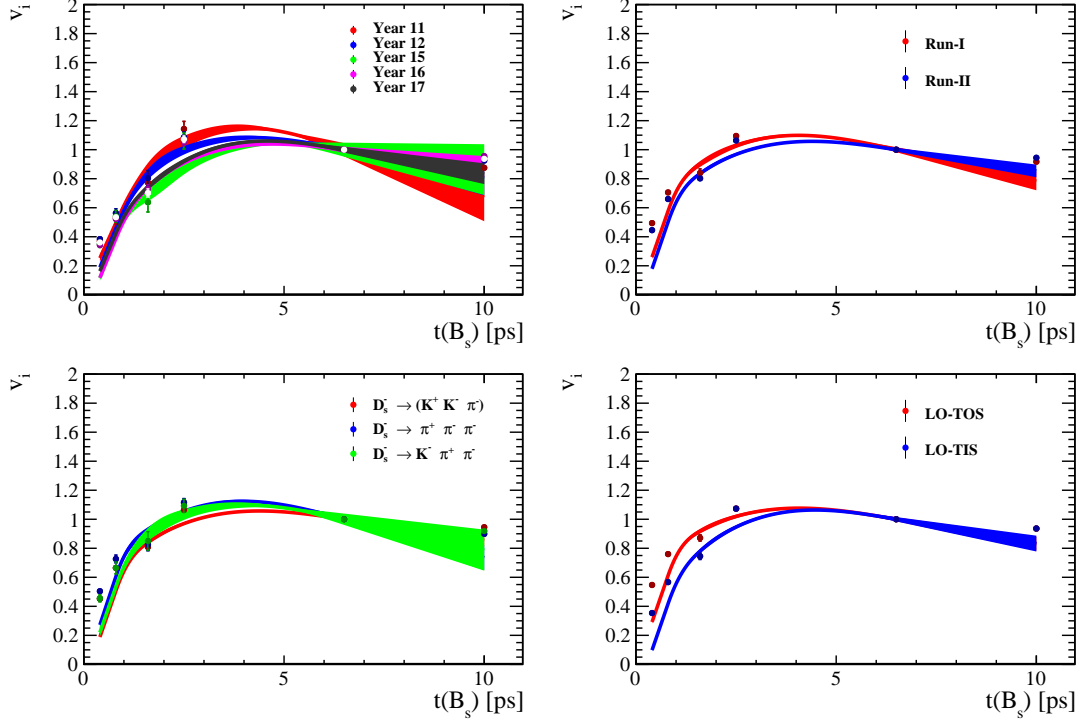


Figure E.1: Comparison of the spline coefficients (point with error bars) obtained from time-dependent fits to the $B_s^0 \rightarrow D_s\pi\pi\pi$ decay-time for different subsamples: (top-left) different years of data-taking; (top-right) different data-taking periods; (bottom-left) different D_s final states; (bottom-right) different trigger categories. The interpolated splines are overlaid.

1146 G Comparison of phase-space acceptance in subsamples

1148 Figures F.1, F.2 and F.3 compare the phase space-acceptance projections obtained from
 1149 $B_s \rightarrow D_s K\pi\pi$ MC in different subsamples. Sufficient agreement is observed between
 1150 different data-taking periods and D_s final states. The largest deviations are observed
 1151 between the different L0 categories.

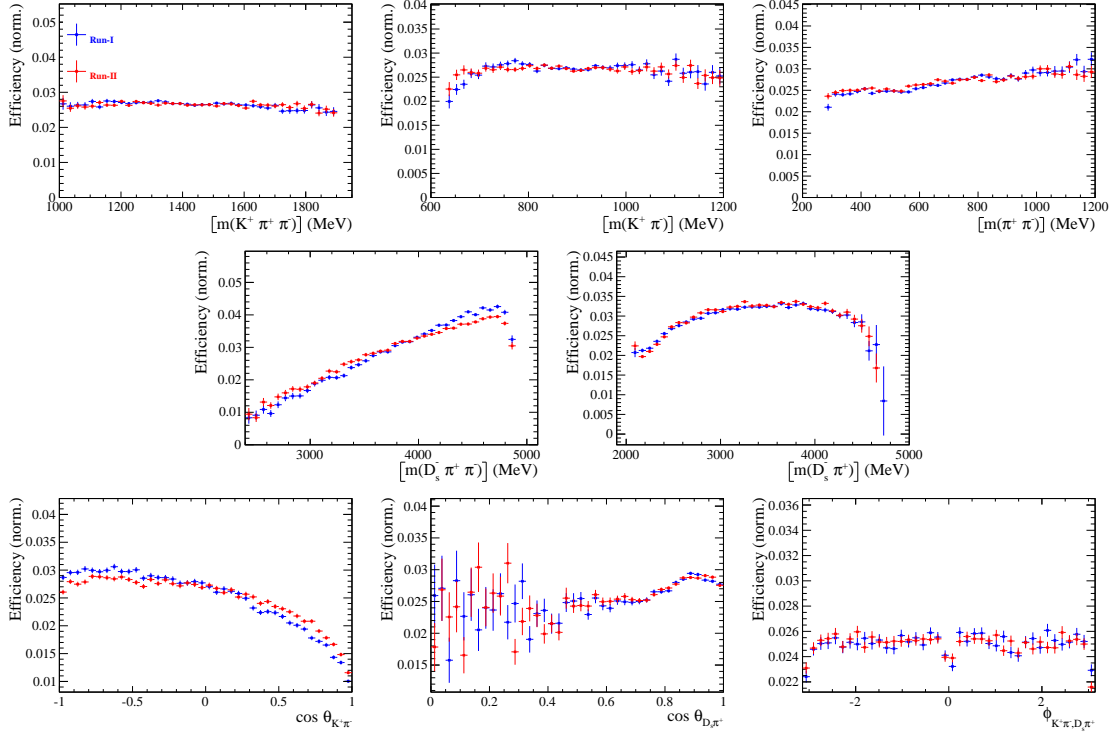


Figure F.1: Comparison of the phase space acceptance for different data-taking periods. A χ^2 -test between the samples yields $\chi^2/\nu = 1.10$ (with $\nu = 533$) using an adaptive 5D binning.

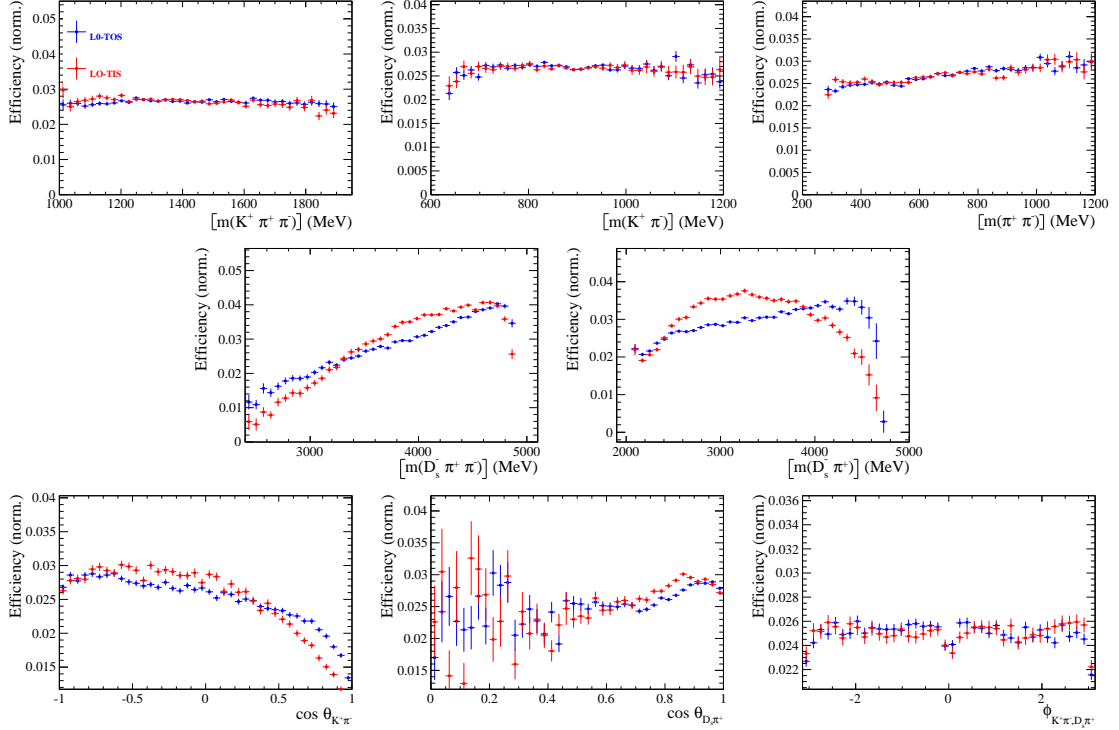


Figure F.2: Comparison of the phase space acceptance for different trigger categories. A χ^2 -test between the samples yields $\chi^2/\nu = 1.62$ (with $\nu = 1211$) using an adaptive 5D binning.

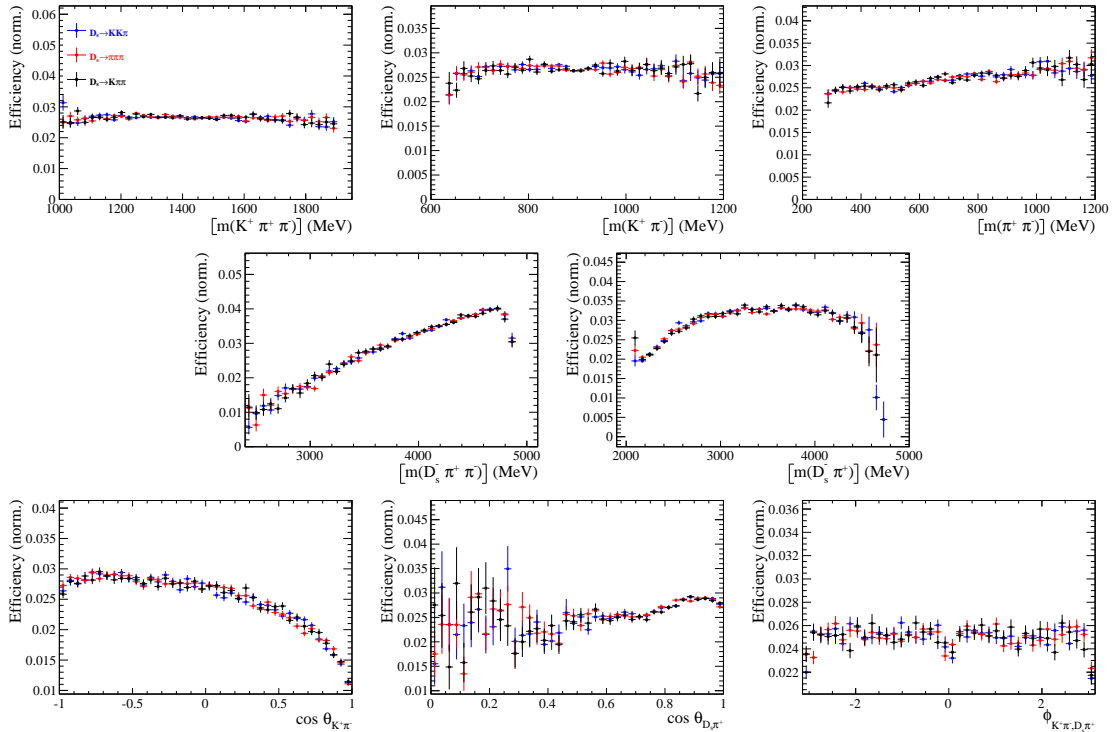


Figure F.3: Comparison of the phase space acceptance for different D_s final states. A χ^2 -test using an adaptive 5D binning between the $D_s \rightarrow KK\pi$ and $D_s \rightarrow K\pi\pi$ samples yields $\chi^2/\nu = 1.01$ (with $\nu = 728$), $\chi^2/\nu = 0.96$ (with $\nu = 988$) between $D_s \rightarrow KK\pi$ and $D_s \rightarrow \pi\pi\pi$ and $\chi^2/\nu = 1.00$ (with $\nu = 728$) between $D_s \rightarrow \pi\pi\pi$ and $D_s \rightarrow K\pi\pi$.

₁₁₅₂ **H OS tagger calibration parameters**

tagger	$\langle \eta \rangle$	$p_0 - \langle \eta \rangle$	p_1	$\rho(p_0, p_1)$
OS μ	0.30	0.010 ± 0.023	1.02 ± 0.26	0.03
OS e	0.29	0.042 ± 0.036	1.87 ± 0.59	0.08
OS K	0.42	0.020 ± 0.010	1.22 ± 0.15	0.03
OS Vtx charge	0.38	-0.011 ± 0.015	1.05 ± 0.23	-0.01

Table G.1: Calibration parameters of the OS taggers for Run-I.

tagger	$\langle \eta \rangle$	$p_0 - \langle \eta \rangle$	p_1	$\rho(p_0, p_1)$
OS μ	0.33	-0.001 ± 0.014	1.24 ± 0.21	0.06
OS e	0.36	0.014 ± 0.020	1.16 ± 0.27	0.06
OS K	0.40	-0.011 ± 0.010	1.51 ± 0.21	0.03
OS Vtx charge	0.39	-0.011 ± 0.010	1.25 ± 0.15	0.03
OS charm	0.36	-0.030 ± 0.019	0.96 ± 0.37	0.04

Table G.2: Calibration parameters of the OS taggers for Run-II.

₁₁₅₃ **I Spin Amplitudes**

₁₁₅₄ The spin factors used for $B \rightarrow P_1 P_2 P_3 P_4$ decays are given in Table H.1.

Table H.1: Spin factors for all topologies considered in this analysis. In the decay chains, S , P , V , A , T and PT stand for scalar, pseudoscalar, vector, axial vector, tensor and pseudotensor, respectively. If no angular momentum is specified, the lowest angular momentum state compatible with angular momentum conservation and, where appropriate, parity conservation, is used.

Number	Decay chain	Spin amplitude
1	$B \rightarrow (P P_1)$, $P \rightarrow (S P_2)$, $S \rightarrow (P_3 P_4)$	1
2	$B \rightarrow (P P_1)$, $P \rightarrow (V P_2)$, $V \rightarrow (P_3 P_4)$	$L_{(1)\alpha}(P) L_{(1)}^\alpha(V)$
3	$B \rightarrow (A P_1)$, $A \rightarrow (V P_2)$, $V \rightarrow (P_3 P_4)$	$L_{(1)\alpha}(B) P_{(1)}^{\alpha\beta}(A) L_{(1)\beta}(V)$
4	$B \rightarrow (A P_1)$, $A[D] \rightarrow (P_2 V)$, $V \rightarrow (P_3 P_4)$	$L_{(1)\alpha}(B) L_{(2)}^{\alpha\beta}(A) L_{(1)\beta}(V)$
5	$B \rightarrow (A P_1)$, $A \rightarrow (S P_2)$, $S \rightarrow (P_3 P_4)$	$L_{(1)\alpha}(B) L_{(1)}^\alpha(A)$
6	$B \rightarrow (A P_1)$, $A \rightarrow (T P_2)$, $T \rightarrow (P_3 P_4)$	$L_{(1)\alpha}(B) L_{(1)\beta}(A) L_{(2)}^{\alpha\beta}(T)$
7	$B \rightarrow (V_1 P_1)$, $V_1 \rightarrow (V_2 P_2)$, $V_2 \rightarrow (P_3 P_4)$	$L_{(1)\mu}(B) P_{(1)}^{\mu\alpha}(V_1) \epsilon_{\alpha\beta\gamma\delta} L_{(1)}^\beta(V_1) p_{V_1}^\gamma L_{(1)}^\delta(V_2)$
8	$B \rightarrow (PT P_1)$, $PT \rightarrow (V P_2)$, $V \rightarrow (P_3 P_4)$	$L_{(2)\alpha\beta}(B) P_{(2)}^{\alpha\beta\gamma\delta}(PT) L_{(1)\gamma}(PT) L_{(1)\delta}(V)$
9	$B \rightarrow (PT P_1)$, $PT \rightarrow (S P_2)$, $S \rightarrow (P_3 P_4)$	$L_{(2)\alpha\beta}(B) L_{(2)}(PT)^{\alpha\beta}$
10	$B \rightarrow (PT P_1)$, $PT \rightarrow (T P_2)$, $T \rightarrow (P_3 P_4)$	$L_{(2)\alpha\beta}(B) P_{(2)}^{\alpha\beta\gamma\delta}(PT) L_{(2)\gamma\delta}(T)$
11	$B \rightarrow (T P_1)$, $T \rightarrow (V P_2)$, $V \rightarrow (P_3 P_4)$	$L_{(2)\mu\nu}(B) P_{(2)}^{\mu\nu\rho\alpha}(T) \epsilon_{\alpha\beta\gamma\delta} L_{(2)\rho}^\beta(T) p_T^\gamma P_{(1)}^{\delta\sigma}(T) L_{(1)\sigma}(V)$
12	$B \rightarrow (T_1 P_1)$, $T_1 \rightarrow (T_2 P_2)$, $T_2 \rightarrow (P_3 P_4)$	$L_{(2)\mu\nu}(B) P_{(2)}^{\mu\nu\rho\alpha}(T_1) \epsilon_{\alpha\beta\gamma\delta} L_{(1)}^\beta(T_1) p_{T_1}^\gamma L_{(2)\rho}^\delta(T_2)$
13	$B \rightarrow (S_1 S_2)$, $S_1 \rightarrow (P_1 P_2)$, $S_2 \rightarrow (P_3 P_4)$	1
14	$B \rightarrow (V S)$, $V \rightarrow (P_1 P_2)$, $S \rightarrow (P_3 P_4)$	$L_{(1)\alpha}(B) L_{(1)}^\alpha(V)$
15	$B \rightarrow (V_1 V_2)$, $V_1 \rightarrow (P_1 P_2)$, $V_2 \rightarrow (P_3 P_4)$	$L_{(1)\alpha}(V_1) L_{(1)}^\alpha(V_2)$
16	$B[P] \rightarrow (V_1 V_2)$, $V_1 \rightarrow (P_1 P_2)$, $V_2 \rightarrow (P_3 P_4)$	$\epsilon_{\alpha\beta\gamma\delta} L_{(1)}^\alpha(B) L_{(1)}^\beta(V_1) L_{(1)}^\gamma(V_2) p_B^\delta$
17	$B[D] \rightarrow (V_1 V_2)$, $V_1 \rightarrow (P_1 P_2)$, $V_2 \rightarrow (P_3 P_4)$	$L_{(2)\alpha\beta}(B) L_{(1)}^\alpha(V_1) L_{(1)}^\beta(V_2)$
18	$B \rightarrow (T S)$, $T \rightarrow (P_1 P_2)$, $S \rightarrow (P_3 P_4)$	$L_{(2)\alpha\beta}(B) L_{(2)}^{\alpha\beta}(T)$
19	$B \rightarrow (V T)$, $T \rightarrow (P_1 P_2)$, $V \rightarrow (P_3 P_4)$	$L_{(1)\alpha}(B) L_{(2)}^{\alpha\beta}(T) L_{(1)\beta}(V)$
20	$B[D] \rightarrow (TV)$, $T \rightarrow (P_1 P_2)$, $V \rightarrow (P_3 P_4)$	$\epsilon_{\alpha\beta\delta\gamma} L_2^{\alpha\mu}(B) L_{2\mu}^\beta L_{(1)}^\gamma(V) p_B^\delta$
21	$B \rightarrow (T_1 T_2)$, $T_1 \rightarrow (P_1 P_2)$, $T_2 \rightarrow (P_3 P_4)$	$L_{(2)\alpha\beta}(T_1) L_{(2)}^{\alpha\beta}(T_2)$
22	$B[P] \rightarrow (T_1 T_2)$, $T_1 \rightarrow (P_1 P_2)$, $T_2 \rightarrow (P_3 P_4)$	$\epsilon_{\alpha\beta\gamma\delta} L_{(1)}^\alpha(B) L_{(2)}^{\beta\mu}(T_1) L_{(2)\mu}^\gamma(T_2) p_B^\delta$
23	$B[D] \rightarrow (T_1 T_2)$, $T_1 \rightarrow (P_1 P_2)$, $T_2 \rightarrow (P_3 P_4)$	$L_{(2)\alpha\beta}(B) L_{(2)}^{\alpha\gamma}(T_1) L_{(2)\gamma}^\beta(T_2)$

1155 J Considered Decay Chains

1156 The various decay channels considered in the model building are listed in Table I.1.

Table I.1: Decays considered in the LASSO model building.

Decay channel
$B_s \rightarrow D_s^- [K_1(1270)^+ [S, D] \rightarrow \pi^+ K^*(892)^0]$
$B_s \rightarrow D_s^- [K_1(1270)^+ \rightarrow \pi^+ K^*(1430)^0]$
$B_s \rightarrow D_s^- [K_1(1270)^+ [S, D] \rightarrow K^+ \rho(770)^0]$
$B_s \rightarrow D_s^- [K_1(1270)^+ [S, D] \rightarrow K^+ \omega(782)]$
$B_s \rightarrow D_s^- [K_1(1400)^+ [S, D] \rightarrow \pi^+ K^*(892)^0]$
$B_s \rightarrow D_s^- [K_1(1400)^+ [S, D] \rightarrow K^+ \rho(770)^0]$
$B_s \rightarrow D_s^- [K(1460)^+ \rightarrow \pi^+ \kappa]$
$B_s \rightarrow D_s^- [K(1460)^+ \rightarrow K^+ \sigma]$
$B_s \rightarrow D_s^- [K(1460)^+ \rightarrow \pi^+ K^*(892)^0]$
$B_s \rightarrow D_s^- [K(1460)^+ \rightarrow K^+ \rho(770)^0]$
$B_s \rightarrow D_s^- [K^*(1410)^+ \rightarrow \pi^+ K^*(892)^0]$
$B_s \rightarrow D_s^- [K^*(1410)^+ \rightarrow K^+ \rho(770)^0]$
$B_s \rightarrow D_s^- [K_2^*(1430)^+ \rightarrow \pi^+ K^*(892)^0]$
$B_s \rightarrow D_s^- [K_2^*(1430)^+ \rightarrow K^+ \rho(770)^0]$
$B_s \rightarrow D_s^- [K^*(1680)^+ \rightarrow \pi^+ K^*(892)^0]$
$B_s \rightarrow D_s^- [K^*(1680)^+ \rightarrow K^+ \rho(770)^0]$
$B_s \rightarrow D_s^- [K_2(1770)^+ \rightarrow \pi^+ K^*(892)^0]$
$B_s \rightarrow D_s^- [K_2(1770)^+ \rightarrow K^+ \rho(770)^0]$
$B_s \rightarrow \sigma^0 (D_s^- K^+)_S$
$B_s [S, P, D] \rightarrow \sigma^0 (D_s^- K^+)_V$
$B_s \rightarrow \rho(770)^0 (D_s^- K^+)_S$
$B_s [S, P, D] \rightarrow \rho(770)^0 (D_s^- K^+)_V$
$B_s \rightarrow K^*(892)^0 (D_s^- \pi^+)_S$
$B_s [S, P, D] \rightarrow K^*(892)^0 (D_s^- \pi^+)_V$
$B_s \rightarrow (D_s^- K^+)_S (\pi^+ \pi^-)_S$

1157 **K Additional information for the time-dependent
1158 amplitude fit**

1159 Table I.1 summarizes the fixed parameters for the resonances included in the baseline
1160 model. The parameters of the resonances $K_1^+(1400)$ and $K^{*+}(1410)$ are determined in
1161 the fit and their PDG values are only shown for comparison. Interference fractions are
1162 listed in Tables I.2 and I.3.

1163 Figure F.1 shows the distribution of likelihood values for 150 time-dependent amplitude
1164 fits with randomized starting parameters. The majority of the fits (76%) converge to the
1165 global minimum. Two well isolated local minima are detected at $\Delta(2NLL) = 13$ (3.3σ)
1166 and $\Delta(2NLL) = 23$ (4.8σ) to which 5% and 11% of the fits converge, respectively. The
1167 fits at $\Delta(2NLL) = 11$, $\Delta(2NLL) = 18$ and $\Delta(2NLL) = 33$ did not converge properly
1168 to one of the nearby local minima. The remaining fits (5%) have $\Delta(2NLL) > 500$ and
1169 are not shown. This procedure has been repeatedly performed during the development of
1170 the analysis, for both LASSO stages and the final fit, to ensure we operate at the global
1171 minimum.

Table I.1: Parameters of the resonances chosen at the model selection stage.

Resonance	m [MeV]	Γ [MeV]	Source
$\rho(770)$	775.26 ± 0.25	149.1 ± 0.8	[15]
$K^{*0}(892)$	895.55 ± 0.20	47.3 ± 0.5	[15]
$K_1^+(1270)$	1289.81 ± 1.75	116.11 ± 3.4	[23]
$K^+(1460)$	1482.4 ± 15.64	335.6 ± 10.64	[23]
$K_1^+(1400)$	1403 ± 7	174 ± 13	[15]
$K^{*+}(1410)$	1421 ± 9	236 ± 18	[15]
$K^{0*}(1430)$	1425 ± 50	270 ± 80	[15]

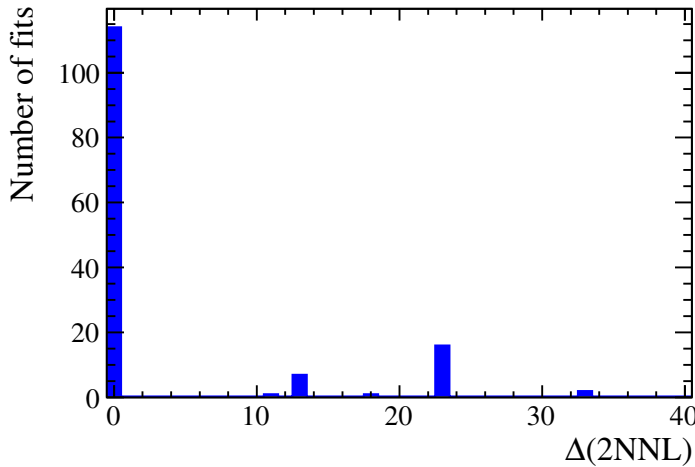


Figure F.1: Likelihood differences with respect to the smallest value obtained from 150 fits with randomized starting parameters.

Table I.2: Interference fractions of the amplitudes contributing to $b \rightarrow c$ decays.

Decay Channel i	Decay Channel j	$I_{ij}[\%]$
$B_s \rightarrow D_s (K_1(1400) \rightarrow K^*(892) \pi)$	$B_s \rightarrow (D_s \pi)_P K^*(892)$	-10.1 ± 4.2
$B_s \rightarrow D_s (K_1(1270) \rightarrow K^*(892) \pi)$	$B_s \rightarrow D_s (K_1(1400) \rightarrow K^*(892) \pi)$	8.8 ± 4.1
$B_s \rightarrow D_s (K_1(1270) \rightarrow K^*(892) \pi)$	$B_s \rightarrow (D_s \pi)_P K^*(892)$	-5.6 ± 1.3
$B_s \rightarrow D_s (K_1(1400) \rightarrow K^*(892) \pi)$	$B_s \rightarrow D_s (K_1(1270) \rightarrow K \rho(770))$	5.3 ± 0.5
$B_s \rightarrow D_s (K^*(1410) \rightarrow K^*(892) \pi)$	$B_s \rightarrow D_s (K^*(1410) \rightarrow K \rho(770))$	5.1 ± 0.3
$B_s \rightarrow D_s (K_1(1270) \rightarrow K_0^*(1430) \pi)$	$B_s \rightarrow D_s (K_1(1270) \rightarrow K \rho(770))$	-2.3 ± 0.8
$B_s \rightarrow (D_s \pi)_P K^*(892)$	$B_s \rightarrow D_s (K_1(1270) \rightarrow K \rho(770))$	0.5 ± 0.2
$B_s \rightarrow D_s (K_1(1270) \rightarrow K^*(892) \pi)$	$B_s \rightarrow D_s (K_1(1270) \rightarrow K \rho(770))$	-0.2 ± 0.4
$B_s \rightarrow D_s (K_1(1400) \rightarrow K^*(892) \pi)$	$B_s \rightarrow D_s (K_1(1270) \rightarrow K_0^*(1430) \pi)$	-0.1 ± 0.0
$B_s \rightarrow (D_s \pi)_P K^*(892)$	$B_s \rightarrow D_s (K_1(1270) \rightarrow K_0^*(1430) \pi)$	0.0 ± 0.0
$B_s \rightarrow D_s (K_1(1400) \rightarrow K^*(892) \pi)$	$B_s \rightarrow D_s (K^*(1410) \rightarrow K \rho(770))$	-0.0 ± 0.0
$B_s \rightarrow D_s (K_1(1400) \rightarrow K^*(892) \pi)$	$B_s \rightarrow D_s (K^*(1410) \rightarrow K^*(892) \pi)$	-0.0 ± 0.0
$B_s \rightarrow D_s (K^*(1410) \rightarrow K^*(892) \pi)$	$B_s \rightarrow D_s (K_1(1270) \rightarrow K \rho(770))$	0.0 ± 0.0
$B_s \rightarrow D_s (K^*(1410) \rightarrow K^*(892) \pi)$	$B_s \rightarrow D_s (K_1(1270) \rightarrow K_0^*(1430) \pi)$	-0.0 ± 0.0
$B_s \rightarrow D_s (K^*(1410) \rightarrow K \rho(770))$	$B_s \rightarrow D_s (K_1(1270) \rightarrow K \rho(770))$	-0.0 ± 0.0
$B_s \rightarrow D_s (K_1(1270) \rightarrow K^*(892) \pi)$	$B_s \rightarrow D_s (K_1(1270) \rightarrow K_0^*(1430) \pi)$	-0.0 ± 0.0
$B_s \rightarrow D_s (K^*(1410) \rightarrow K^*(892) \pi)$	$B_s \rightarrow (D_s \pi)_P K^*(892)$	-0.0 ± 0.0
$B_s \rightarrow (D_s \pi)_P K^*(892)$	$B_s \rightarrow D_s (K^*(1410) \rightarrow K \rho(770))$	0.0 ± 0.0
$B_s \rightarrow D_s (K^*(1410) \rightarrow K \rho(770))$	$B_s \rightarrow D_s (K_1(1270) \rightarrow K_0^*(1430) \pi)$	-0.0 ± 0.0
$B_s \rightarrow D_s (K_1(1270) \rightarrow K^*(892) \pi)$	$B_s \rightarrow D_s (K^*(1410) \rightarrow K^*(892) \pi)$	-0.0 ± 0.0
$B_s \rightarrow D_s (K_1(1270) \rightarrow K^*(892) \pi)$	$B_s \rightarrow D_s (K^*(1410) \rightarrow K \rho(770))$	0.0 ± 0.0

Table I.3: Interference fractions of the amplitudes contributing to $b \rightarrow u$ decays.

Decay Channel i	Decay Channel j	$I_{ij}[\%]$
$B_s \rightarrow D_s (K_1(1270) \rightarrow K^*(892) \pi)$	$B_s \rightarrow (D_s \pi)_P K^*(892)$	-20.7 ± 4.9
$B_s \rightarrow D_s (K_1(1270) \rightarrow K^*(892) \pi)$	$B_s \rightarrow D_s (K_1(1400) \rightarrow K^*(892) \pi)$	-20.0 ± 8.7
$B_s \rightarrow D_s (K_1(1400) \rightarrow K^*(892) \pi)$	$B_s \rightarrow (D_s \pi)_P K^*(892)$	18.9 ± 9.7
$B_s \rightarrow D_s (K(1460) \rightarrow K^*(892) \pi)$	$B_s \rightarrow (D_s \pi)_P K^*(892)$	-8.4 ± 1.2
$B_s \rightarrow (D_s K)_P \rho(770)$	$B_s \rightarrow D_s (K_1(1270) \rightarrow K_0^*(1430) \pi)$	-6.3 ± 1.2
$B_s \rightarrow D_s (K_1(1270) \rightarrow K_0^*(1430) \pi)$	$B_s \rightarrow D_s (K_1(1270) \rightarrow K \rho(770))$	-5.5 ± 1.7
$B_s \rightarrow (D_s \pi)_P K^*(892)$	$B_s \rightarrow (D_s K)_P \rho(770)$	3.1 ± 0.6
$B_s \rightarrow D_s (K_1(1400) \rightarrow K^*(892) \pi)$	$B_s \rightarrow (D_s K)_P \rho(770)$	2.0 ± 0.6
$B_s \rightarrow D_s (K_1(1400) \rightarrow K^*(892) \pi)$	$B_s \rightarrow D_s (K_1(1270) \rightarrow K \rho(770))$	2.0 ± 1.3
$B_s \rightarrow (D_s \pi)_P K^*(892)$	$B_s \rightarrow D_s (K_1(1270) \rightarrow K \rho(770))$	1.7 ± 0.8
$B_s \rightarrow D_s (K(1460) \rightarrow K^*(892) \pi)$	$B_s \rightarrow (D_s K)_P \rho(770)$	-1.5 ± 0.3
$B_s \rightarrow D_s (K_1(1270) \rightarrow K^*(892) \pi)$	$B_s \rightarrow (D_s K)_P \rho(770)$	-1.3 ± 0.4
$B_s \rightarrow D_s (K_1(1270) \rightarrow K^*(892) \pi)$	$B_s \rightarrow D_s (K_1(1270) \rightarrow K \rho(770))$	-0.6 ± 1.0
$B_s \rightarrow (D_s \pi)_P K^*(892)$	$B_s \rightarrow D_s (K_1(1270) \rightarrow K_0^*(1430) \pi)$	0.1 ± 0.0
$B_s \rightarrow (D_s K)_P \rho(770)$	$B_s \rightarrow D_s (K_1(1270) \rightarrow K \rho(770))$	-0.1 ± 2.9
$B_s \rightarrow D_s (K(1460) \rightarrow K^*(892) \pi)$	$B_s \rightarrow D_s (K_1(1270) \rightarrow K \rho(770))$	0.1 ± 0.0
$B_s \rightarrow D_s (K_1(1270) \rightarrow K^*(892) \pi)$	$B_s \rightarrow D_s (K(1460) \rightarrow K^*(892) \pi)$	0.0 ± 0.0
$B_s \rightarrow D_s (K_1(1400) \rightarrow K^*(892) \pi)$	$B_s \rightarrow D_s (K(1460) \rightarrow K^*(892) \pi)$	-0.0 ± 0.0
$B_s \rightarrow D_s (K_1(1270) \rightarrow K^*(892) \pi)$	$B_s \rightarrow D_s (K_1(1270) \rightarrow K_0^*(1430) \pi)$	-0.0 ± 0.0
$B_s \rightarrow D_s (K_1(1400) \rightarrow K^*(892) \pi)$	$B_s \rightarrow D_s (K_1(1270) \rightarrow K_0^*(1430) \pi)$	0.0 ± 0.0
$B_s \rightarrow D_s (K(1460) \rightarrow K^*(892) \pi)$	$B_s \rightarrow D_s (K_1(1270) \rightarrow K_0^*(1430) \pi)$	0.0 ± 0.0

L Data-simulation comparisson

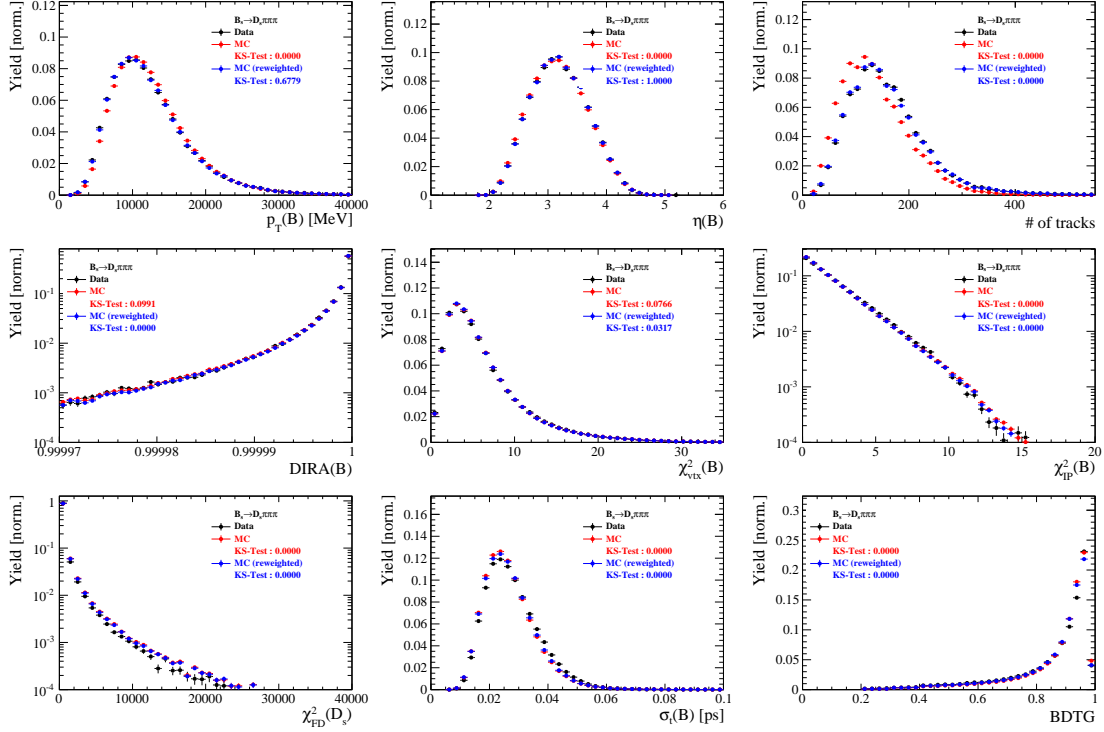


Figure J.1: Comparison between data and MC of selected variables for $B_s \rightarrow D_s \pi\pi$ decays.

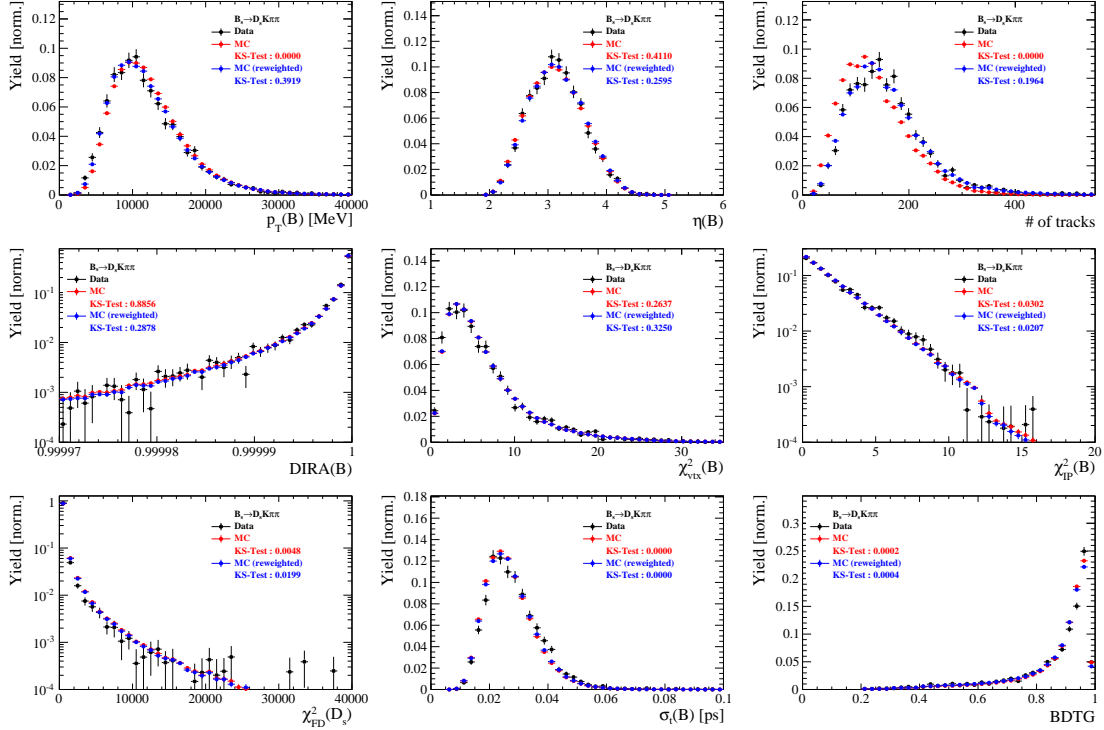


Figure J.2: Comparison between data and MC of selected variables for $B_s \rightarrow D_s K\pi\pi$ decays.

1173 M Data distributions

1174 Comparison of signal and calibration channels

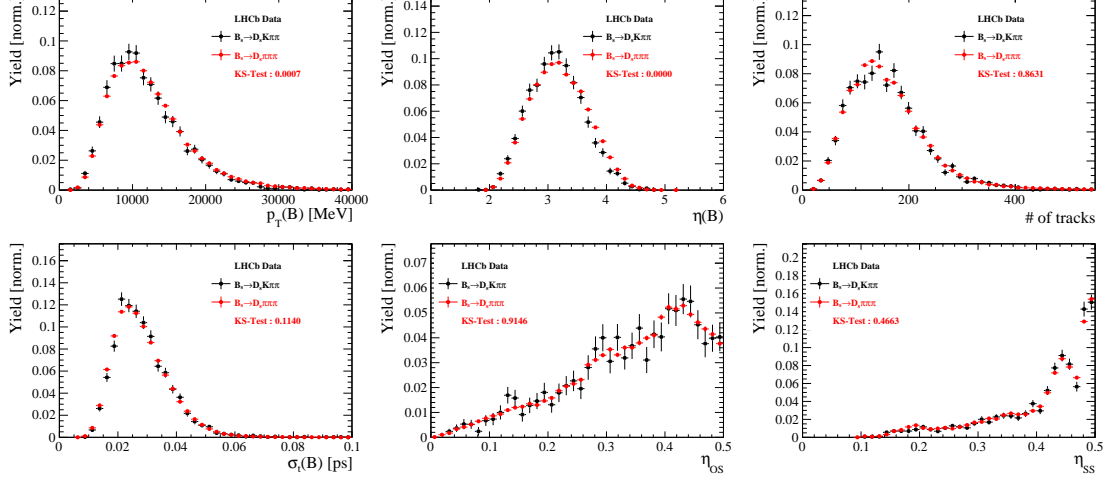


Figure K.1: Comparison between $B_s \rightarrow D_s K\pi\pi$ and $B_s \rightarrow D_s \pi\pi\pi$ decays for selected variables.

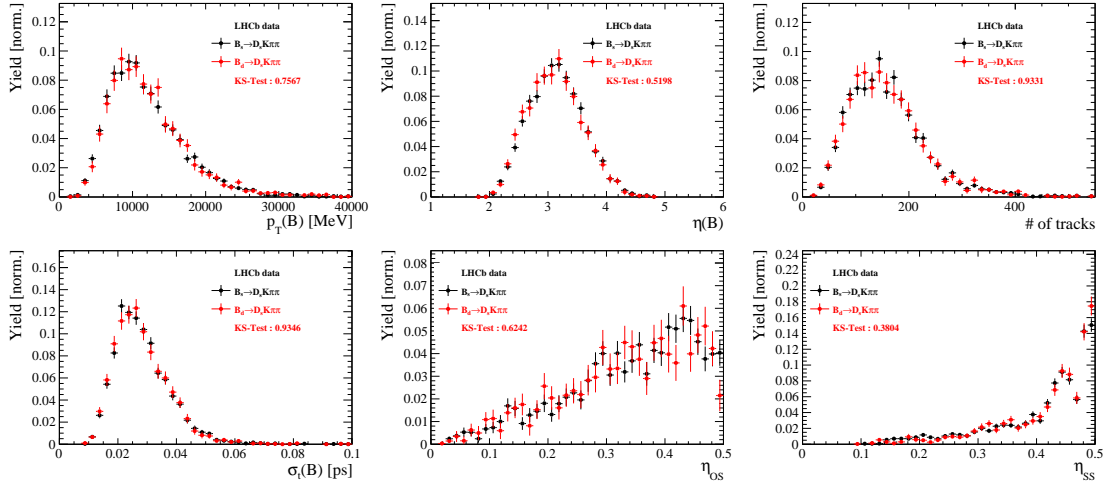


Figure K.2: Comparison between $B_s \rightarrow D_s K\pi\pi$ and $B_d \rightarrow D_s K\pi\pi$ decays for selected variables.

1175 Comparison of data taken in 2016 and 2017

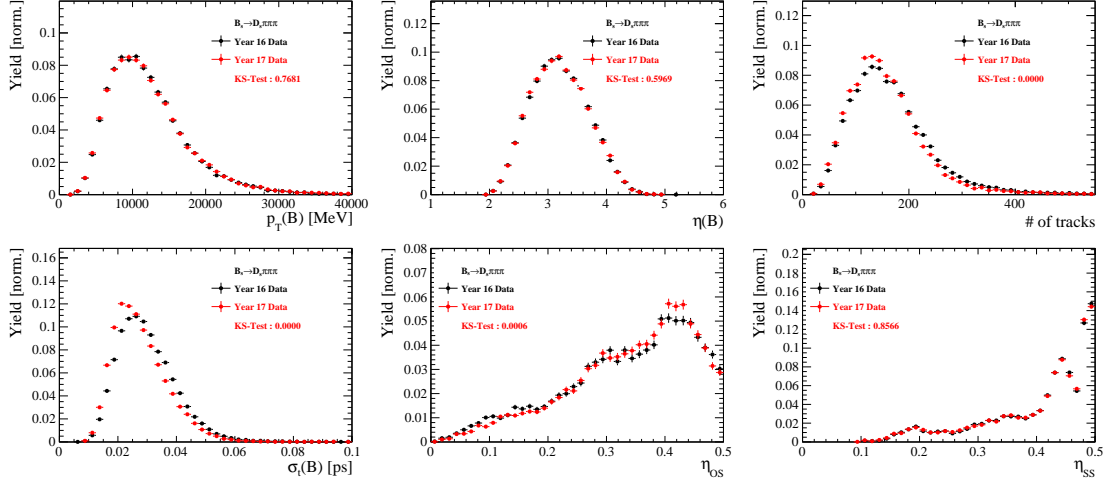


Figure K.3: Comparison of selected variables for $B_s \rightarrow D_s \pi\pi\pi$ data taken in 2016 and 2017.

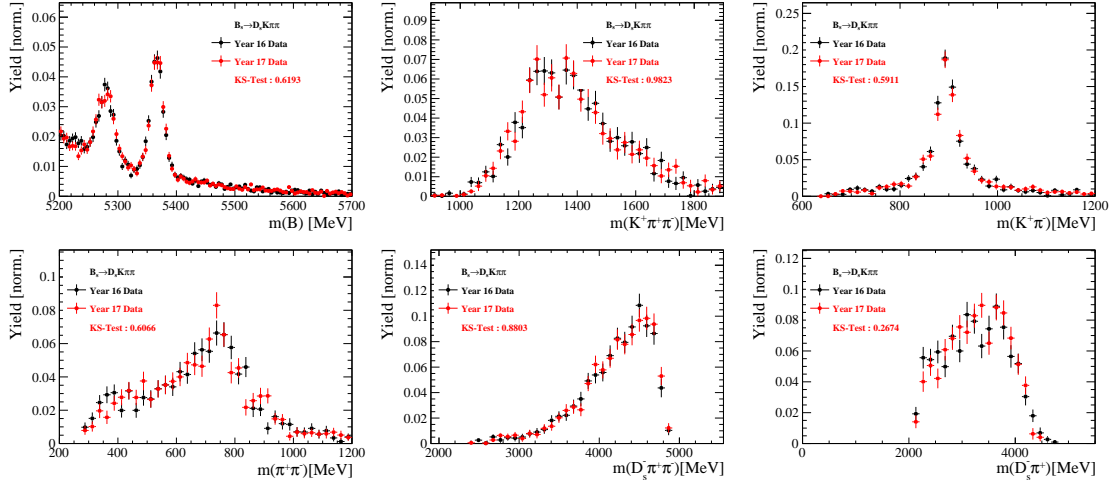


Figure K.4: Comparison of selected variables for $B_s \rightarrow D_s K\pi\pi$ data taken in 2016 and 2017.

Comparison of Run-I and Run-II data

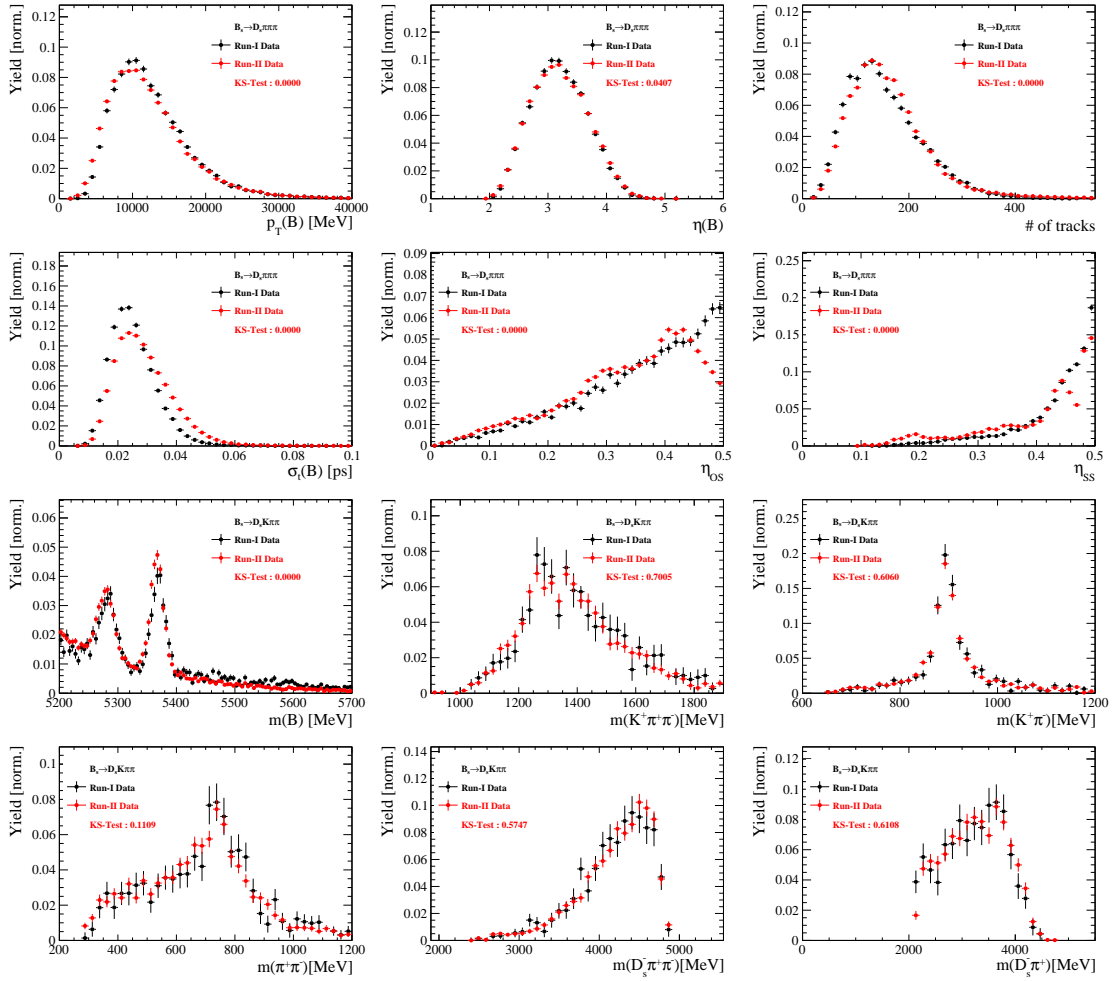


Figure K.5: Comparison of selected variables for Run-I and Run-II data.

1177 Comparison of D_s final states

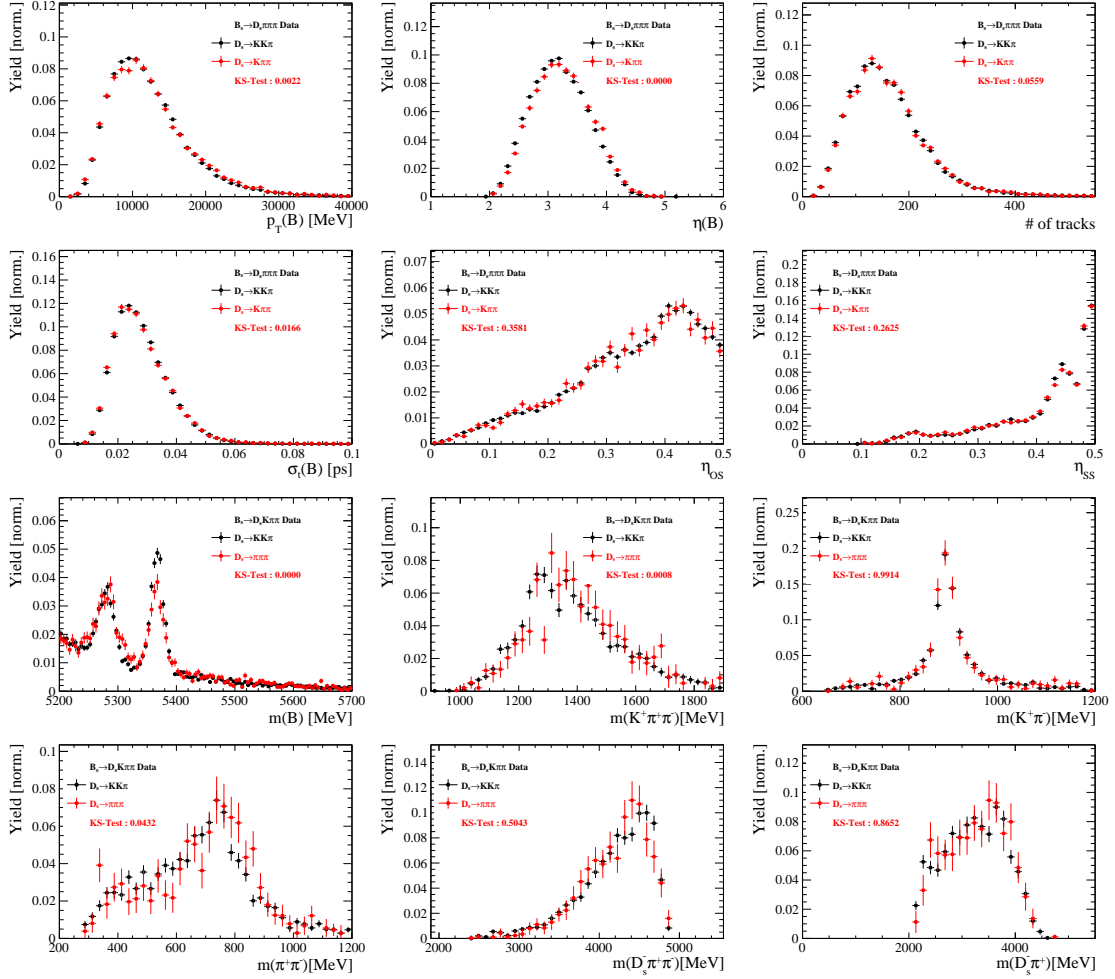


Figure K.6: Comparison of selected variables for different D_s final states.

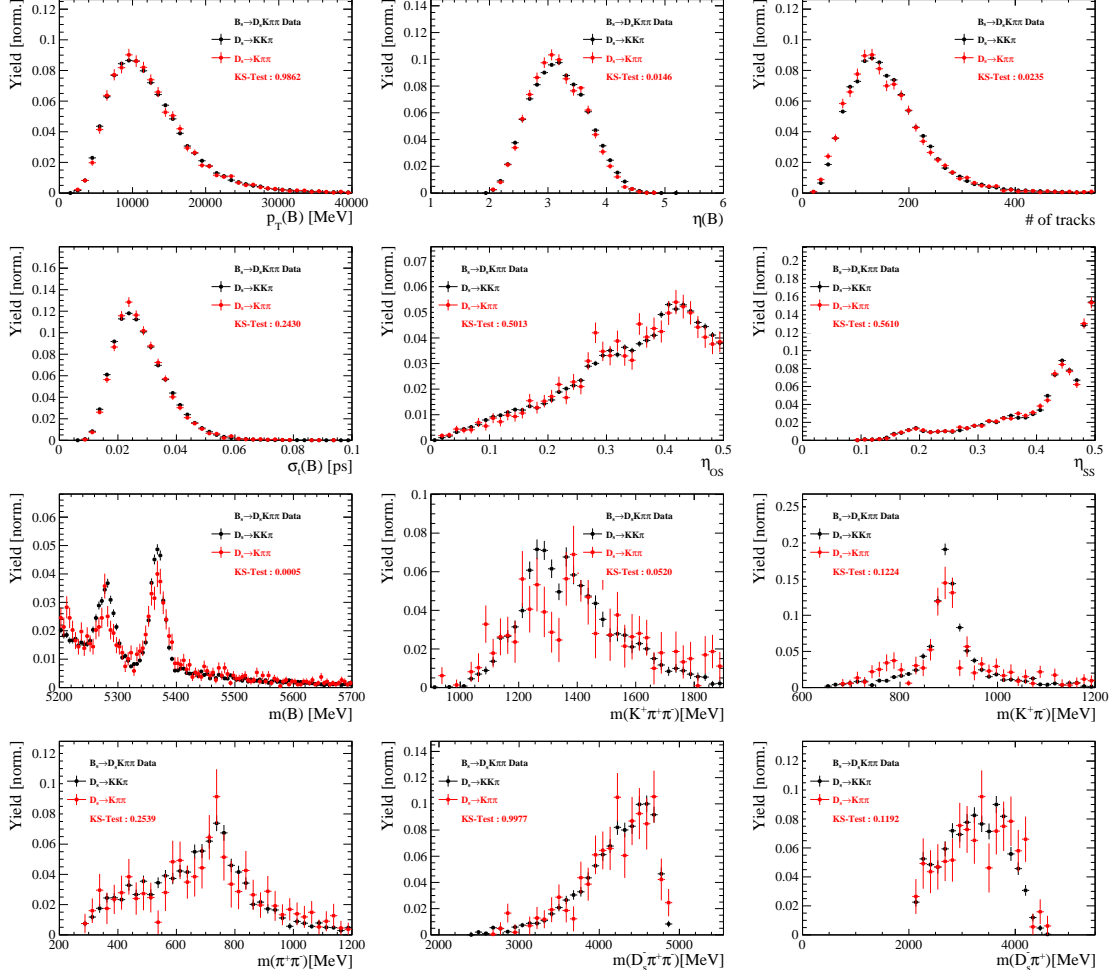


Figure K.7: Comparison of selected variables for different D_s final states.

1178 Comparison of trigger categories

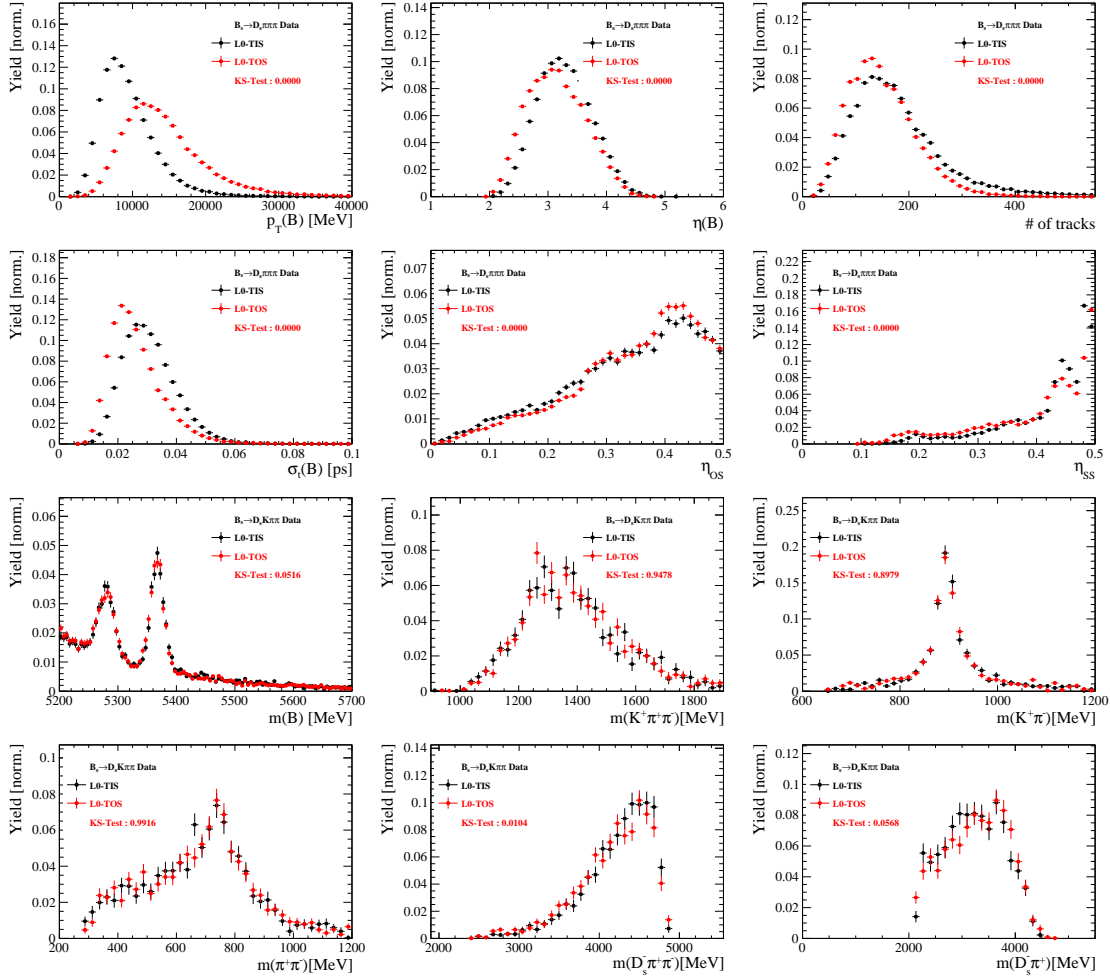


Figure K.8: Comparison of selected variables for different trigger categories.

1179 **References**

- 1180 [1] S. Blusk, *First observations and measurements of the branching fractions for the*
1181 *decays $\bar{B}_s^0 \rightarrow D_s^+ K^- \pi^+ \pi^-$ and $\bar{B}^0 \rightarrow D_s^+ K^- \pi^+ \pi^-$* , LHCb-ANA-2012-076.
- 1182 [2] LHCb, S. Blusk, *Measurement of the CP observables in $\bar{B}_s^0 \rightarrow D_s^+ K^-$ and first obser-*
1183 *vation of $\bar{B}_{(s)}^0 \rightarrow D_s^+ K^- \pi^+ \pi^-$ and $\bar{B}_s^0 \rightarrow D_{s1}(2536)^+ \pi^-$* , 2012. [arXiv:1212.4180](#).
- 1184 [3] LHCb collaboration, R. Aaij *et al.*, *First observation of the decays $\bar{B}_{(s)}^0 \rightarrow D_s^+ K^- \pi^+ \pi^-$*
1185 *and $\bar{B}_s^0 \rightarrow D_{s1}(2536)^+ \pi^-$* , Phys. Rev. **D86** (2012) 112005, [arXiv:1211.1541](#).
- 1186 [4] R. Fleischer, *New strategies to obtain insights into CP violation through $B_s \rightarrow$*
1187 *$D_s^\pm K^\mp, D_s^{*\pm} K^\mp, \dots$ and $B_d \rightarrow D^\pm \pi^\mp, D^{*\pm} \pi^\mp, \dots$ decays*, Nucl. Phys. **B671** (2003) 459,
1188 [arXiv:hep-ph/0304027](#).
- 1189 [5] K. De Bruyn *et al.*, *Exploring $B_s \rightarrow D_s^{(*)\pm} K^\mp$ Decays in the Presence of a Sizable*
1190 *Width Difference $\Delta\Gamma_s$* , Nucl. Phys. **B868** (2013) 351, [arXiv:1208.6463](#).
- 1191 [6] L. collaboration, *Measurement of time-dependent CP-violation observables in $B_s^0 \rightarrow$*
1192 *$D_s^\mp K^\pm$* , LHCb-ANA-2016-052.
- 1193 [7] LHCb, R. Aaij *et al.*, *Measurement of CP asymmetry in $B_s^0 \rightarrow D_s^\mp K^\pm$ decays*, JHEP
1194 **03** (2018) 059, [arXiv:1712.07428](#).
- 1195 [8] E. Byckling and K. Kajantie, *Particle Kinematics*, John Wiley & Sons, 1973.
- 1196 [9] S. Mandelstam, J. E. Paton, R. F. Peierls, and A. Q. Sarker, *Isobar approximation*
1197 *of production processes*, Annals of Physics **18** (1962), no. 2 198 .
- 1198 [10] D. J. Herndon, P. Söding, and R. J. Cashmore, *Generalized isobar model formalism*,
1199 Phys. Rev. D **11** (1975) 3165.
- 1200 [11] J. J. Brehm, *Unitarity and the isobar model: Two-body discontinuities*, Annals of
1201 Physics **108** (1977), no. 2 454 .
- 1202 [12] P. d'Argent *et al.*, *Amplitude Analyses of $D^0 \rightarrow \pi^+ \pi^- \pi^+ \pi^-$ and $D^0 \rightarrow K^+ K^- \pi^+ \pi^-$*
1203 *Decays*, JHEP **05** (2017) 143, [arXiv:1703.08505](#).
- 1204 [13] F. von Hippel and C. Quigg, *Centrifugal-barrier effects in resonance partial decay*
1205 *widths, shapes, and production amplitudes*, Phys. Rev. D **5** (1972) 624.
- 1206 [14] J. D. Jackson, *Remarks on the phenomenological analysis of resonances*, Il Nuovo
1207 Cimento Series 10 **34** (1964), no. 6 1644.
- 1208 [15] Particle Data Group, C. Patrignani *et al.*, *Review of Particle Physics*, Chin. Phys.
1209 **C40** (2016), no. 10 100001.
- 1210 [16] C. Zemach, *Use of angular momentum tensors*, Phys. Rev. **140** (1965) B97.
- 1211 [17] W. Rarita and J. Schwinger, *On a theory of particles with half integral spin*, Phys.
1212 Rev. **60** (1941) 61.

- [18] S. U. Chung, *General formulation of covariant helicity-coupling amplitudes*, Phys. Rev. D **57** (1998) 431.
- [19] B. S. Zou and D. V. Bugg, *Covariant tensor formalism for partial wave analyses of ψ decay to mesons*, Eur. Phys. J. **A16** (2003) 537, [arXiv:hep-ph/0211457](https://arxiv.org/abs/hep-ph/0211457).
- [20] V. Filippini, A. Fontana, and A. Rotondi, *Covariant spin tensors in meson spectroscopy*, Phys. Rev. **D51** (1995) 2247.
- [21] J.-J. Zhu, *Explicit expressions of spin wave functions*, [arXiv:hep-ph/9906250](https://arxiv.org/abs/hep-ph/9906250).
- [22] M. Williams, *Numerical Object Oriented Quantum Field Theory Calculations*, Comput. Phys. Commun. **180** (2009) 1847, [arXiv:0805.2956](https://arxiv.org/abs/0805.2956).
- [23] LHCb, R. Aaij *et al.*, *Studies of the resonance structure in $D^0 \rightarrow K^\mp\pi^\pm\pi^\pm\pi^\mp$ decays*, Eur. Phys. J. **C78** (2018), no. 6 443, [arXiv:1712.08609](https://arxiv.org/abs/1712.08609).
- [24] D. J. Lange, *The EvtGen particle decay simulation package*, Nucl. Instrum. Meth. **A462** (2001) 152.
- [25] M. Karbach and M. Kenzie, *Gammacombo package*, <http://gammacombo.hepforge.org/web/HTML/index.html>, 2014.
- [26] A. Hoecker *et al.*, *TMVA: Toolkit for Multivariate Data Analysis*, PoS **ACAT** (2007) 040, [arXiv:physics/0703039](https://arxiv.org/abs/physics/0703039).
- [27] N. L. Johnson, *Systems of frequency curves generated by methods of translation*, Biometrika **36** (1949), no. 1/2 149.
- [28] Particle Data Group, K. A. Olive *et al.*, *Review of Particle Physics*, Chin. Phys. **C38** (2014) 090001.
- [29] LHCb collaboration, R. Aaij *et al.*, *LHCb detector performance*, Int. J. Mod. Phys. **A30** (2015) 1530022, [arXiv:1412.6352](https://arxiv.org/abs/1412.6352).
- [30] M. Schiller, *Proper time resolution studies in $B_s \rightarrow D_s\pi$* , Tech. Rep. LHCb-INT-2011-005. CERN-LHCb-INT-2011-005, CERN, Geneva, Feb, 2011.
- [31] LHCb collaboration, L. Zhang, *Measurements of CP violation in $B_s^0 \rightarrow J/\psi K^+K^-$ decays in the low K^+K^- mass range with 13 TeV data*, LHCb-ANA-2017-028.
- [32] A. Poluektov, *Correction of simulated particle identification response in LHCb using kernel density estimation*, LHCb-INT-2017-007.
- [33] Heavy Flavor Averaging Group, Y. Amhis *et al.*, *Averages of b-hadron, c-hadron, and τ -lepton properties as of summer 2014*, [arXiv:1412.7515](https://arxiv.org/abs/1412.7515), updated results and plots available at <http://www.slac.stanford.edu/xorg/hfag/>.
- [34] T. M. Karbach, G. Raven, and M. Schiller, *Decay time integrals in neutral meson mixing and their efficient evaluation*, [arXiv:1407.0748](https://arxiv.org/abs/1407.0748).
- [35] LHCb collaboration, R. Aaij *et al.*, *Opposite-side flavour tagging of B mesons at the LHCb experiment*, Eur. Phys. J. **C72** (2012) 2022, [arXiv:1202.4979](https://arxiv.org/abs/1202.4979).

- [36] LHCb, R. Aaij *et al.*, *A new algorithm for identifying the flavour of B_s^0 mesons at LHCb*, JINST **11** (2016), no. 05 P05010, [arXiv:1602.07252](#).
- [37] LHCb, R. Aaij *et al.*, *Measurement of B^0 , B_s^0 , B^+ and Λ_b^0 production asymmetries in 7 and 8 TeV proton-proton collisions*, Phys. Lett. **B774** (2017) 139, [arXiv:1703.08464](#).
- [38] H. Gordon, R. W. Lambert, J. van Tilburg, and M. Vesterinen, *A Measurement of the $K\pi$ Detection Asymmetry*, Tech. Rep. LHCb-INT-2012-027. CERN-LHCb-INT-2012-027, CERN, Geneva, Feb, 2013.
- [39] A. Davis *et al.*, *Measurement of the instrumental asymmetry for $K^-\pi^+$ -pairs at LHCb in Run 2*, Tech. Rep. LHCb-PUB-2018-004. CERN-LHCb-PUB-2018-004, CERN, Geneva, Mar, 2018.
- [40] I. I. Y. Bigi and H. Yamamoto, *Interference between Cabibbo allowed and doubly forbidden transitions in $D \rightarrow K(S)$, $K(L) + \pi$'s decays*, Phys. Lett. **B349** (1995) 363, [arXiv:hep-ph/9502238](#).
- [41] M. Pivk and F. R. Le Diberder, *sPlot: A statistical tool to unfold data distributions*, Nucl. Instrum. Meth. **A555** (2005) 356, [arXiv:physics/0402083](#).
- [42] R. Tibshirani, *Regression shrinkage and selection via the Lasso*, Journal of the Royal Statistical Society, Series B **58** (1994) 267.
- [43] B. Guegan, J. Hardin, J. Stevens, and M. Williams, *Model selection for amplitude analysis*, JINST **10** (2015), no. 09 P09002, [arXiv:1505.05133](#).
- [44] G. Schwarz, *Estimating the dimension of a model*, Ann. Statist. **6** (1978) 461.
- [45] CLEO Collaboration, M. Artuso *et al.*, *Amplitude analysis of $D^0 \rightarrow K^+K^-\pi^+\pi^-$* , Phys. Rev. **D85** (2012) 122002, [arXiv:1201.5716](#).
- [46] T. Skwarnicki, *A study of the radiative cascade transitions between the Upsilon-prime and Upsilon resonances*, PhD thesis, Institute of Nuclear Physics, Krakow, 1986, DESY-F31-86-02.
- [47] D. Hill, M. John, and P. Gandini, *A study of partially reconstructed $B^\pm \rightarrow D^{*0}h^\pm$ decays using the $D^0 \rightarrow K\pi$, KK , $\pi\pi$ final states*, LHCb-ANA-2017-018.
- [48] G. H. Golub and C. F. Van Loan, *Matrix Computations (3rd Ed.)*, Johns Hopkins University Press, Baltimore, MD, USA, 1996.
- [49] L. collaboration, *Precision measurement of the B_s oscillation frequency with the decay $B_s \rightarrow D_s\pi$* , LHCb-ANA-2012-053.
- [50] LHCb collaboration, R. Aaij *et al.*, *Precision measurement of the $B_s^0 - \bar{B}_s^0$ oscillation frequency in the decay $B_s^0 \rightarrow D_s^-\pi^+$* , New J. Phys. **15** (2013) 053021, [arXiv:1304.4741](#).
- [51] BaBar, P. del Amo Sanchez *et al.*, *Measurement of $D0$ -anti $D0$ mixing parameters using $D0 \rightarrow K(S)0$ pi+ pi- and $D0 \rightarrow K(S)0$ K+ K- decays*, Phys. Rev. Lett. **105** (2010) 081803, [arXiv:1004.5053](#).

- 1286 [52] LHCb, R. Aaij *et al.*, *Studies of the resonance structure in $D^0 \rightarrow K_S^0 K^\pm \pi^\mp$ decays*,
 1287 Phys. Rev. **D93** (2016), no. 5 052018, arXiv:1509.06628.
- 1288 [53] D. V. Bugg, *The mass of the σ pole*, Journal of Physics G Nuclear Physics **34** (2007)
 1289 151, arXiv:hep-ph/0608081.
- 1290 [54] W. Dunwoodie. Fits to $K\pi$ $I = \frac{1}{2}$ S -wave amplitude and phase data.
- 1291 [55] D. Aston *et al.*, *A Study of $K^-\pi^+$ Scattering in the Reaction $K^-p \rightarrow K^-\pi^+n$ at*
 1292 $11\text{GeV}/c$, Nucl. Phys. **B296** (1988) 493.
- 1293 [56] BaBar, B. Aubert *et al.*, *Dalitz-plot analysis of the decays $B^\pm \rightarrow K^\pm \pi^\mp \pi^\pm$* ,
 1294 Phys. Rev. **D72** (2005) 072003, arXiv:hep-ex/0507004, [Erratum: Phys.
 1295 Rev.D74,099903(2006)].
- 1296 [57] G. J. Gounaris and J. J. Sakurai, *Finite-width corrections to the vector-meson-*
 1297 *dominance prediction for $\rho \rightarrow e^+e^-$* , Phys. Rev. Lett. **21** (1968) 244.
- 1298 [58] CMD-2, R. R. Akhmetshin *et al.*, *Measurement of $e^+e^- \rightarrow \pi^+\pi^-$ cross-section with*
 1299 *CMD-2 around rho meson*, Phys. Lett. **B527** (2002) 161, arXiv:hep-ex/0112031.
- 1300 [59] M. S. et al. *Search for CP violation in the $D^0 \rightarrow KK\pi\pi$ decay through a full*
 1301 *amplitude analysis*, LHCb-ANA-2017-064.
- 1302 [60] LHCb Collaboration, R. Aaij, *Search for CP violation through an amplitude analysis*
 1303 *of $D^0 \rightarrow K^+K^-\pi^+\pi^-$ decays*, Tech. Rep. arXiv:1811.08304. LHCb-PAPER-2018-041,
 1304 CERN, Geneva, Nov, 2018. * Temporary entry *.
- 1305 [61] S. M. Flatté, *Coupled-channel analysis of the $\pi\eta$ and KK systems near KK threshold*,
 1306 Physics Letters B **63** (1976), no. 2 224 .
- 1307 [62] BES Collaboration, M. Ablikim *et al.*, *Resonances in $J/\psi \rightarrow \phi\pi^+\pi^-$ and ϕK^+K^-* ,
 1308 Phys. Lett. **B607** (2005) 243, arXiv:hep-ex/0411001.